

University of Bath



PHD

Novel fibres for endoscopy

Wood, Harry

Award date:
2019

Awarding institution:
University of Bath

[Link to publication](#)

General rights

Copyright and moral rights for the publications made accessible in the public portal are retained by the authors and/or other copyright owners and it is a condition of accessing publications that users recognise and abide by the legal requirements associated with these rights.

- Users may download and print one copy of any publication from the public portal for the purpose of private study or research.
- You may not further distribute the material or use it for any profit-making activity or commercial gain
- You may freely distribute the URL identifying the publication in the public portal ?

Take down policy

If you believe that this document breaches copyright please contact us providing details, and we will remove access to the work immediately and investigate your claim.

Download date: 23. May. 2019



Citation for published version:

Wood, H 2018, 'Novel fibres for endoscopy', Ph.D., University of Bath.

Publication date:

2018

[Link to publication](#)

University of Bath

General rights

Copyright and moral rights for the publications made accessible in the public portal are retained by the authors and/or other copyright owners and it is a condition of accessing publications that users recognise and abide by the legal requirements associated with these rights.

Take down policy

If you believe that this document breaches copyright please contact us providing details, and we will remove access to the work immediately and investigate your claim.

NOVEL FIBRES FOR ENDOSCOPY

Harry Alexander Charles Wood

A thesis submitted for the degree of Doctor of Philosophy

University of Bath

Department of Physics

May 2018

COPYRIGHT

Attention is drawn to the fact that copyright of this thesis rests with its author. This copy of the thesis has been supplied on condition that anyone who consults it is understood to recognise that its copyright rests with its author and no information derived from it may be published without the prior written consent of the author.

This thesis may be made available for consultation within the University library and may be photocopied or lent to other libraries for the purposes of consultation

*for Mum, Dad,
Grace, & Tom*

Contents

Contents	3
Acknowledgements	7
Abstract.....	8
Overview	9
Introduction.....	10
1.1 Optics and medicine.....	10
1.2 Proteus.....	13
1.2.1 Goals	13
1.2.2 Collaboration Structure	15
1.2.3 My role.....	16
The basics.....	17
2.1 Theory of optical fibres.....	17
2.1.1 Core concepts.....	17
2.1.2 Guided modes	18
2.1.3 Silica glass	22
2.2 Photonic crystal fibre	22
2.2.1 Hollow core fibres.....	23
2.2 Techniques	25
2.2.1 Fibre fabrication.....	25
2.2.1.1 Doped preform manufacture	25
2.2.1.2 Drawing down.....	26
2.2.1.3 Stacking.....	28
2.2.2 Post processing.....	30
2.2.2.1 Cleaving	30
2.2.2.2 Polishing.....	31
2.2.2.3 Tapering	31
2.2.3 Characterisation	32
2.2.3.1 Numerical aperture.....	32
2.2.3.2 USAF resolution test targets	32
2.2.3.3 Dispersion	34

Sensing.....	36
3.1 Introduction	36
3.2 Fluorescence spectroscopy	36
3.2.1 Work from Proteus	37
3.2.2 Optical fibres from Bath	37
3.3 Raman spectroscopy	40
3.3.1 SERS in Proteus.....	41
3.3.2 Raman background problem.....	42
3.3.3 Photonic lanterns	43
3.3.4 Little & large core fibre	44
3.3.5 Hollow core fibre.....	45
3.4 Conclusion	49
Chapter 4.....	50
Imaging fibres	50
4.1 Inter-core coupling	50
4.1.1 The resolution/wavelength limit	50
4.1.2 Non-identical core pairs.....	52
4.1.3 Anderson localisation	53
4.2 Prior work.....	53
4.2.1 Fujikura.....	53
4.2.3 Leached fibre bundles.....	55
4.2.4 Phased array imaging.....	56
4.2.5 Multi-stacking techniques.....	57
4.3 Panoptes imaging fibres.....	60
4.3.1 50,000-core fibre	61
4.3.1.1 Fabrication	61
4.3.1.2 Imaging characterisation.....	64
4.3.1.3 Coupling characterisation	65
4.3.2 The step index Panoptes imaging fibre – PSII	67
4.3.2.1 Fabrication	68
4.3.2.2 Characterisation	68
4.3.3 Panoptes graded-index imaging fibre – PGI1	69
4.3.3.1 Fabrication	69
4.3.3.2 Characterisation	70
4.3.4 Panoptes graded-index 9.....	71
4.3.4.1 Fabrication	72
4.3.4.1 Characterisation	73

4.3.5 Square array imaging fibre.....	74
4.3.5.1 Fabrication	74
4.3.5.2 Characterisation	80
4.4 Conclusion	82
Imaging fibre characterisation	83
5.1 Established methods.....	83
5.1.1 Test target imaging.....	83
5.1.2 Coupled power characterisation.....	84
5.1.3 Modulation transfer function	84
5.2 Quantitative interferometric characterisation.....	84
5.2.1 Theory and preliminary work	85
5.2.2 Fringe visibility analysis	86
5.2.3 Final experiment design	88
5.2.4 Data.....	90
5.2.5 Further development	93
Air-clad imaging fibres.....	94
6.1 Introduction.....	94
6.2 Prior work	95
6.2.1 Hollow core imaging fibres.....	95
6.2.2 Chalcogenide glass fibre bundles.....	96
6.2.3 Multi-core photonic crystal fibres.....	97
6.2.4 Disordered fibres.....	98
6.2.5 Air-polymer microstructured fibre.....	100
6.2.6 Superlattice microstructured optical fibre.....	101
6.3 PCF imaging	102
6.4 Air clad imaging - ACI1	105
6.4.1 Fabrication	105
6.4.2 Characterisation	108
6.5 ACI2.....	109
6.5.1 Fabrication	109
6.7 ACI4.....	111
6.7.1 Fabrication	111
6.7.2 Characterisation	114
6.7.2.1 USAF test target imaging.....	115
6.7.2.2 Quantitative characterisation.....	117
6.7.2.3 Numerical aperture.....	118

6.7.2.4	Dispersion.....	118
6.7.2.5	Coupled family imaging	121
6.8	Medical significance.....	121
6.9	Post-processing.....	122
6.9.1	Necessity.....	122
6.9.2	Tapering.....	122
6.9.3	Adhesives and wax	123
6.10	Conclusion.....	124
Conclusion		125
List of acronyms.....		127
Publications		129
B.1	Journal publications	129
B.2	Conference presentations	129
References		131

Acknowledgements

Many helped me settle into the PhD role, but I want to give special thanks to Hasti, Rose, Clarissa, Jamie, Rowan, Adrian, and Stephanos, for going out of their way to look after me, and the other fledgling students. I can't imagine the amount of time and effort your advice, mentoring, tips, and tricks have saved me.

I am grateful for my glamorous team of proof-readers; Charlotte, Joel, and Carlo, I'm a waffler, so I know it can't have been easy! Many thanks also to Olly, Tom, and Dave for your continuing help getting the words from the tip of my tongue onto paper.

To my supervisors, Tim and Jonathan; I've been both privileged, and honoured to have studied with you. Thanks for giving me the opportunities, freedom, encouragement, and guidance that I needed more than I knew.

William and Pete, you both always treat all the group's students as your own. Time and again you've gone beyond what is required to ensure we are all growing happily within the physics community.

Jon and Sean, you've been my Merry and Pippin. I've relied on your help and companionship, from second breakfast, to the fields of Pelennor - thanks for all the fun.

Thanks for putting up with me Rebecca, and for doing your best to keep we boys out of trouble!

Kerri, for years now we have worked side by side in the office, lab, and tower - painting lines and clinking glass. Even our most stressful times you still greet me with all the warmth of a cup of coffee, and an even darker sense of humour.

Jim, I honestly couldn't ask for a better mentor. Thanks for everything.

Finally, to all the members of the Department of Physics, both past and present:

You have made this place a home to me.

Thank you.

Abstract

The research I present in this thesis is a collection of recent developments of endoscopic optical fibre technology, focussing primarily on my contributions to the field of bronchoscopy.

The bulk of my PhD has been spent advancing the coherent fibre bundle technology that is used prolifically for endoscopic imaging. This was achieved by controlling the core-to-core crosstalk that is the primary mechanism of image quality degradation. In this thesis I report novel methods of fabricating several lower cost but high performance imaging fibres that use regular lattices of different sized cores to suppress coupling. Ultimately, I detail my methods of fabricating a new class of imaging fibre that uses an air-filled cladding to better confine the light to its cores. I go on to show that this type of fibre offers 3.2 μm resolution, competitive with leading commercial alternatives, but functions up to wavelengths in excess of 1500 nm. These fibres can also be drawn thinner or post-processed to provide resolutions down to 2.2 μm , superior to any silica based imaging fibres currently on the market.

In addition to using a selection of established techniques to measure and compare the performance of my imaging fibres, I also use a technique of my own design that uses an interference pattern of filtered supercontinuum light as the standard image. This allows the fibre's performance to be quantified across a wide spectrum of optical and spatial frequencies.

The prospect of including a fibre designed for sensing the chemical environment (such as pH and oxygen saturation) of the distal end of the endoscope is currently a subject of great interest to the optical fibre field. The associated challenges and some potential solutions that have been developed by my group are also discussed in this thesis.

Overview

Within this thesis several advances to the optical technology used for medical endoscopy are presented. Chapters 1 and 2 provide the historical and scientific context for the results detailed in chapters 3, 4, 5, and 6.

I outline a brief historical summary of the optics used for endoscopy in Chapter 1 before discussing the structure and goals of the Proteus project, and the role I have played as part of it.

In chapter 2 I equip the reader with the basic scientific knowledge and technical jargon necessary to fully understand the results presented to them in later chapters.

Chapter 3 begins by outlining two optical methods of detecting physiological characteristics that can be used to diagnose disease. I discuss the challenges of integrating these techniques into an optical fibre probe, before presenting novel designs for fibre devices to conquer these challenges, and the results obtained through their use.

In chapter 4 I provide a deeper understanding of the optical processes relevant to the design of imaging fibres for endoscopy. I describe a few of the most popular imaging fibre solutions in industry, and discuss their respective advantages and limitations before detailing the Proteus project's, and my own contributions to the development of this technology.

I describe a novel quantitative imaging fibre characterisation technique that I developed and published during this PhD in chapter 5.

What will likely be the highest impact achievement of my PhD is detailed in chapter 6. I provide a full description of the novel techniques that I have developed for the fabrication of imaging fibres comprised of silica cores within an air-filled cladding. I go on to show that these air-clad imaging fibres have double the operational wavelength range when compared with state of the art commercial equivalents, with equal resolution.

Chapter 7 concludes this thesis by discussing the significance of the results presented in previous chapters and their place in the wider research field.

Chapter 1

Introduction

1.1 Optics and medicine

The story of optical fibres is a young one, with almost all of its development taking place over the course of the extraordinarily rapid telecoms boom. It is easy to believe that the technology is rooted in the field of telecommunications, but in fact we find its origins in a far earlier form of optical technology; medical endoscopes.

The critical obstacle to early endoscopy lay in illuminating the investigated body cavity. In 1804 Philipp Bozzini published the designs of his “Lichtleiter”, which literally translates to “Light Conductor”, as the first endoscopic device to effectively address the illumination problem [1,2]. This was well before the conception of electric light, so his invention, figure 1.1, used a candle as the light source.



Figure 1.1: Bozzini’s lichtleiter, and its various attachments and specula. Image obtained from the European Museum of Urology [3].

The candle was set within the metal box and the light guided by a set of mirrors into a metal tube which carried it into the body. Different tubes could be attached to suit the orifice being investigated, and an eyepiece on the opposite side of the box allowed the inside of the body cavity to be observed. As often happens, this advancement received a very mixed response, but later it would come to be recognised as the earliest effective form of endoscopy. This type of technology would soon be improved by higher performance lighting, such as Sir Humphry Davy's arc lamp, and deepening knowledge of lenses would allow longer and thinner endoscopes to be made. 30 years after the birth of the Lichleiter, Daniel Collodon and Jacques Babinet would guide light using jets of water for the very different application of fountain displays, and shortly afterwards John Tyndall showed experimentally that light was being guided by the higher refractive index of water compared to the surrounding air [4]. This principle was first put to medical use in 1888 when Dr. Roth and Prof. Reuss pioneered the first dental and medical illuminators that were composed of little more than glass rods that had been bent to guide light around corners and into body cavities. It would soon be realised that such optics could be used to guide light and even images from around bends; a key ability that rigid endoscopes lacked.

The RCA Rocky Point Laboratory on Long Island filed a patent in 1927 on Clarence Hansell's idea to use a bundle of optical fibres, all in the same arrangement at both ends, to transmit grainy but coherent images made up of the spots of light transmitted by each individual fibre. The British inventor John Logie baird used and patented a similar idea for his early attempts at inventing the television. It is this principle that most modern coherent fibre bundle endoscopes are based upon, but unfortunately little was done to capitalise on the concept at the time. It wasn't until 1930 that Heinrich Lamm came to a similar epiphany and proceeded to fabricate a rudimentary coherent fibre bundle and demonstrate its imaging properties using a lightbulb filament as the object [4]. Of course, when attempting to patent his invention he found Hansell's institution already held it. 20 years later Holger Moller Hansen and Abraham Van Heel would begin researching the topic at the Technical University of Delft, and with the help of the University of Rochester's Brian O'Brien realise that the application of a low refractive index cladding material would dramatically improve the fibre's transmission quality [4]. They published their research on imaging fibre bundles in Nature simultaneously with Harold H. Hopkins and Narinder Kapany of Imperial College London [4,5].

With the advantages of flexible endoscopes clear, one might think that rigid ones have no place in modern medicine. In fact, they still see use today because they are not limited by the number of imaging elements, but instead the resolution of their lens systems. The last fundamental improvement to their design would come in the 1960s when Harold Hopkins replaced the lenses, which required the support of obstructive rings, with rod-like lenses that were self-supporting and filled the full diameter of the scope [6,7].

At this point, incremental design changes produced flexible imaging fibres that functioned well enough to enable some minimally invasive medical procedures, but attenuation was still too

high to allow adaptation of the technology for telecoms. This changed in 1970 when researchers at Corning showed that they had fabricated single mode optical fibres based on research done by Dr. Charles Kao of the University of New South that had attenuation below 20 dB/km [8,9]. The fibres were made of pure silica, deposited from the vapour phase, with a doped core. This is what forms individual imaging elements in the optical fibres used for bronchoscopy to this day.

With modern phone cameras that offer multi-megapixel resolution in a package no more than a few millimetres across, one might wonder why imaging fibres have not been replaced by cameras on wires? They would have higher resolution, and the wire could be made thinner and more flexible than an imaging fibre. The answer lies in recent advances in microscopy such as confocal fluorescence microscopy which uses the energy transitions of organic molecules such as elastin or collagen [10] to produce images with far more definition. Simple colour images of flesh can be difficult to diagnose, but with fluorescence microscopy images such as the one in figure 1.2 are possible. In this case two stains have been added to give dead cells all the visibility of a red phosphorous flare amongst the forest of green stained living cells.

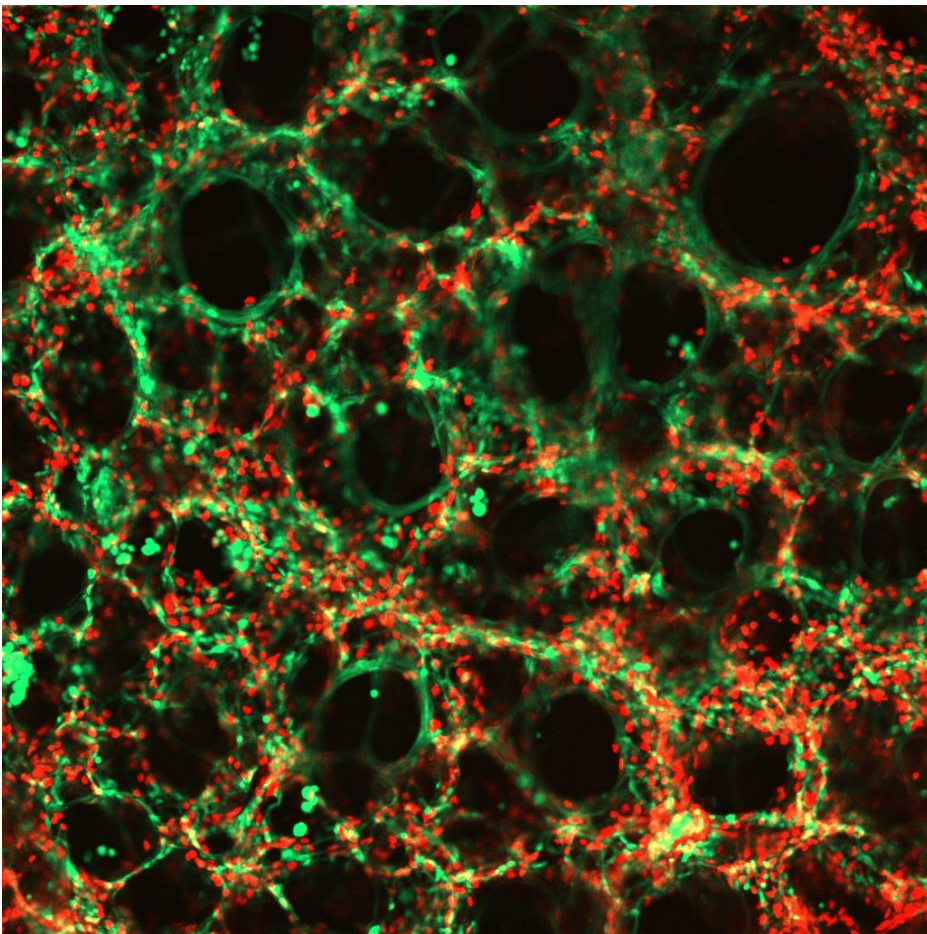


Figure 1.2: A fluorescence microscope image of the alveolar region of a sheep lung, courtesy of Proteus PhD student Philip Emmanuel. Living cells are stained in green, dead cells in red, and the green autofluorescence of the elastin is also visible.

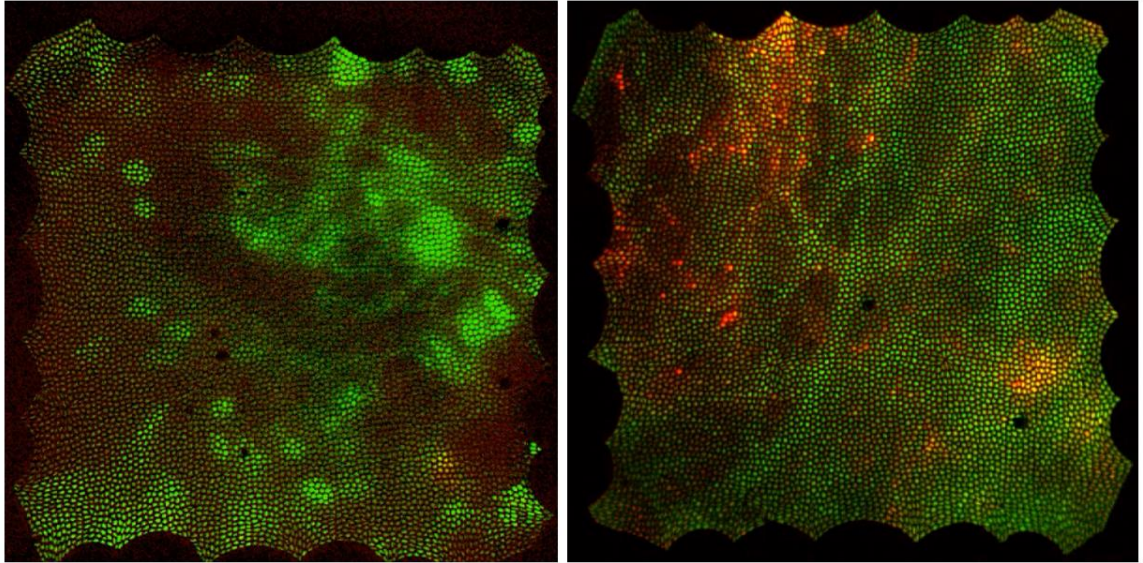


Figure 1.3: Fluorescence images of ex-vivo human lung tissue in a well plate using one of our square array imaging fibres, discussed in chapter 4. In the left image the neutrophils (a type of immune cell) have been stained with a green fluorescent compound. In the right image bacteria have been stained with a red fluorophore. The green background fluorescence of the fibrous lung tissues pervades both images.

Fluorescence microscopy can be done with relative ease through an imaging fibre to produce images as in figure 1.3, but a camera endoscope is limited to imaging reflected light. This also enables the use of marker compounds that only fluoresce when bound to specific pathogens, making their identification easy. Most bacteria are under $2\ \mu\text{m}$ in length – roughly the same size or smaller than the cores of an imaging fibre. This means that, when searching for ones marked by fluorophores, they manifest as “twinkling” lights as they move past the cores, either due to the operators manipulations or the natural movements of the living body.

1.2 Proteus

Proteus [11] is one of three collaborative interdisciplinary research projects co-funded by the UK government’s engineering and physical sciences research council (EPSRC) (Proteus’ grant code is EP/K03197X/1) from Q3 2014 to Q3 2018. The mandate of these projects was to improve the outcomes of patients in the national health care system. To this end, Proteus has brought together a multidisciplinary team from the Universities of Bath, Edinburgh and Heriot Watt, to improve the technology used to diagnose pulmonary disease in patients in intensive care.

1.2.1 Goals

The efforts of Proteus are targeted at the challenges of lung disease diagnosis which leads to more than 100,000 deaths annually in the UK alone. When a patient is admitted into intensive care with acute respiratory distress syndrome (ARDS) they are usually put on a ventilator to maintain their blood oxygen levels. Although this temporarily preserves their lives, it also makes diagnosis and treatment of the illness more difficult as they are usually unconscious, so only limited patient history is available, their airways are more difficult to access and inspect, and mucus moves up and out far more slowly. Although the ventilator tube is sterilised before being inserted, the fact it brings fresh air directly to the bottom of the trachea means it bypasses many of our usual defences (such as mucus in the nose and throat) and can lead to further infection.

Diagnosis of lung disease usually begins with bronchoscopy, where a flexible endoscope is inserted into the ventilator tube and guided into the bronchus and bronchi of the lungs using a small camera at the tip. When the passages are too small for the main endoscope body (roughly 5 mm) an unguided imaging fibre is inserted via the endoscope's working channel, and gently pushed to the deepest reaches of the lungs; the alveoli. Such inspections rarely reveal more than inflammation, infection, and foreign matter. The potential causes are many, and the multitude of possible treatments are also ailing for the patient. Moreover, it has been shown that a clinician's view through these instruments is so poor it could be considered legally blind [12]. To gain further information a biopsy must be obtained. This is often done during bronchoscopy using a lavage – saline solution is pumped into the lungs and then sucked out, including a sample of the pathogens present. The introduction of foreign material to the lungs, even sterile saline solution, risks further decreasing the efficiency of the gas exchanging membranes of the alveolar spaces in the lungs [13]. Lavage samples must then be cultured and the polymerase chain reaction (PCR) used to identify the pathogens present. This takes time that the patient may not have, and even then, often only identifies bacteria that naturally present in healthy lungs as lavage is not specific to the infected part of the lungs, but entire branches. Of course, specific biopsies can be taken by invasive, transthoracic (through the chest wall) surgery, but this carries its own risks, such as further infection or even pulmonary haemorrhaging. All of this usually leads the clinicians to administer a broad-spectrum treatment that itself exerts a huge toll on the patient's body.

Since the development of commercial optical fibre fluorescence imaging endoscope systems, such as Mauna Kea's Cellvizio [14, 15], lung disease diagnosis accuracy has improved slightly. This system costs over a hundred thousand pounds and functions with a selection of different endoscopic probes for different purposes. These probes are easily connected and disconnected from the main unit, cost a few thousand pounds each, and can be used and re-sterilised up to 20 times before being discarded.

Proteus' goal is to improve patient outcomes by advancing endoscopic technology that has hardly changed in 20 years. This is being done in three main ways, each with subsidiary objectives:

- Improvement of imaging fibre technology
 - Increased resolution
 - Fluorescent probes for bacteria identification
 - Broad spectrum functionality for probes of disparate fluorescence wavelengths
- Addition of sensing fibres to guide light for spectroscopy from;
 - pH sensitive fluorescent compounds
 - Surface enhanced Raman spectroscopy (SERS) probes
- Incorporation of capillaries that reach the same alveoli as the imaging probe
 - For drug and/or probe delivery
 - For lavage and sample collection from specific lung locations

The device's design was additionally constrained by having a maximum outer diameter of 1.4 mm to remain compatible with other endoscope and ventilator technologies, and to prevent damage to the bronchioles when it is pushed to the alveoli. Flexibility was also a key consideration, as a minimum bend radius of 5 cm was required to access the upper lobes of the lung. The ultimate goal was to produce a functional commercial product that satisfied all of these criteria. However, this also needed to be balanced against the final cost of the device to the clinic. If this could be made sufficiently low to allow disposal after a single use, clinical workflow would also be improved by avoiding additional sterilisation procedures.

Work began with preliminary research into the plethora of technologies that could fill these roles. Focus later shifted to assembling the most effective solutions into the multiplexed "touch-and-tell" probe that we have named Panoptes. The design has since been finalised and our prototypes are currently going through biocompatibility testing before the clinical trials later this year.

1.2.2 Collaboration Structure

To build an effective probe with all of the components discussed in the section above, Proteus has brought together skilled researchers from three academic institutions as shown in figure 1.4. In the University of Edinburgh and the Queen's medical research institution (QMRI) clinicians who actively treat patients with ARDS help test prototypes produced by the project on analogues such as sheep lungs or human lung tissue well plates, and advise on further development. The chemists and biologists there work in tandem researching novel compounds for fluorescence or SERS sensing. Machine learning and image processing experts in Edinburgh write the code necessary to produce useful images and data from the raw information received from the endoscope. Physicists at Heriot Watt University engineer the optics for the distal and proximal fibre ends, as well as the sensors that

interpret the optical signals and the programs for processing them. Physicists of the University of Bath's Centre for Photonics and Photonic Materials (CPPM) use our knowledge of waveguides and fibre fabrication facilities to produce the novel optical fibres to bridge the gap between the distal lung and the sensors.

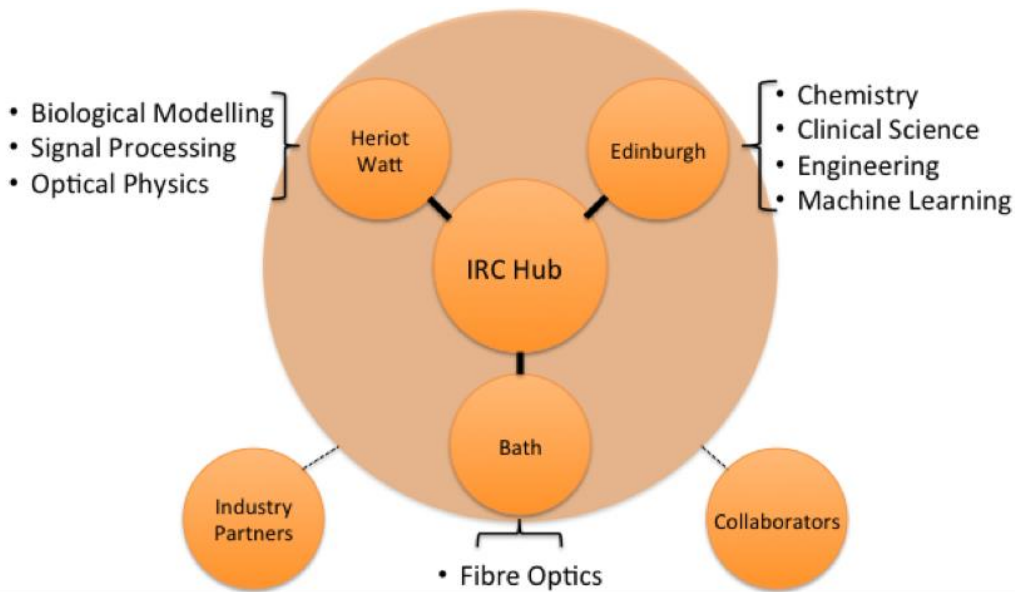


Figure 1.4: A diagram of the organisational structure of the Proteus project.

1.2.3 My role

I joined the Proteus project in late 2014, around 6 months before the Panoptes work package began. Since then I have worked as a postgraduate researcher in Bath's CPPM, learning and refining the design and fabrication techniques for imaging and sensing fibres. The multidisciplinary nature of the project has also allowed me to extend the foundation of my knowledge to include aspects of human physiology, chemistry, engineering, and biology.

This thesis contains a summary of the knowledge and expertise I have accumulated over the past 4 years, and the academic outputs and papers I have produced.

Chapter 2

The basic theory and practice

This chapter aims to equip the reader with basic theory and terminology to ease their journey through the rest of the thesis. It is not intended as a complete guide to optical fibre technology.

2.1 Theory of optical fibres

2.1.1 Core concepts

Most optical fibres used in modern telecommunications systems consist of strands of silica (SiO_2) glass a tenth of a millimetre in diameter, with a pure cladding and a core region which is doped with germanium to give a higher refractive index, as shown in figure 2.1.

The refractive index contrast between core and cladding produces a boundary that refracts incident light. When light in the higher index core interacts with the boundary at a sufficiently shallow angle the refracted ray travels along the index boundary, as established by Snell's law of refraction. At even shallower angles the refracted light would still be inside the core glass, so it instead undergoes total internal reflection (TIR) back into the core material. It follows that light propagating in the core of the fibre with an appropriately small angle relative to the fibre's axis will be confined by TIR at the boundaries and guided along the fibre's length [16,17,18]. With the guidance mechanism established, we now consider the conditions for light entering the end face of the fibre such that it will be guided – a process called coupling in. Based on the critical angle for TIR and refraction on entering the structure, the maximum allowed incident angle, θ in figure 2.1, can be found. It follows that the light emitted from the other fibre end forms a cone of similar angle.

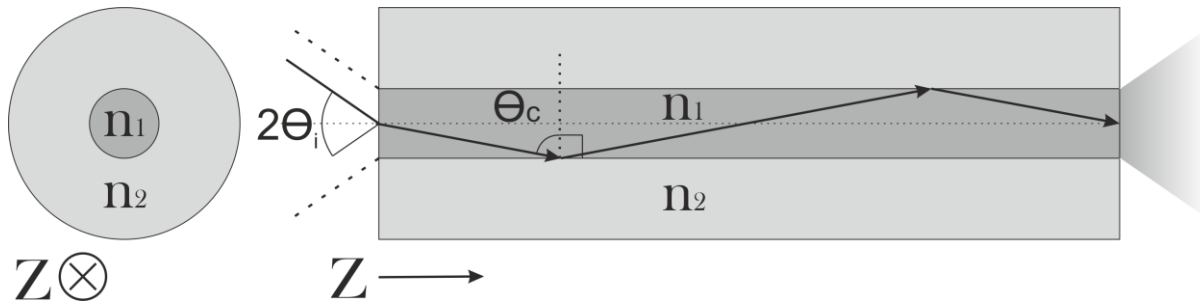


Figure 2.1: Left is an end-on diagram of a step index optical fibre, where n_1 , the core, is a higher index material than n_2 , the cladding. Right is side-on cross section of the same fibre, with a ray guidance diagram. The ray is incident on the left end face with a maximum angle θ , is guided by total internal reflection, then is emitted from the right end with the same maximum angle.

Snell's law can again be used to derive equation 1 for calculating the maximum angle of the incident and emitted light cones, θ ;

$$\sin \theta_i = \sqrt{n_1^2 - n_2^2} = NA . \quad (1)$$

The numerical aperture (NA) is a useful parameter in several equations describing the characteristics of optical fibres, and has become the industry's standard measure of the index contrast between core and cladding.

2.1.2 Guided modes

As the waveguide's core size approaches that of the wavelength of the light being guided it becomes difficult to fully describe the light's properties using the ray TIR guidance model. This is both because of the influence of diffraction, as well as the complexity of summing over all the interfering waves [16,17]. An alternative method of exploring this guidance regime is through the use of Maxwell's equations. As glass is not magnetic and has no free charges, these can be simplified to

$$\nabla \times \mathbf{E} = -\frac{\partial \mathbf{B}}{\partial t} , \quad (2)$$

$$\nabla \times \mathbf{H} = \frac{\partial \mathbf{D}}{\partial t} , \quad (3)$$

$$\nabla \cdot \mathbf{D} = 0 , \quad (4)$$

and

$$\nabla \cdot \mathbf{B} = 0 , \quad (5)$$

where t is time, \mathbf{E} and \mathbf{H} are the electric and magnetic field vectors respectively, and \mathbf{D} and \mathbf{B} are likewise the displacement current and magnetic flux densities. Using substitution and vector identities gives the vector wave equation

$$\nabla^2 \mathbf{E} - \frac{1}{c^2} \frac{\partial^2 \mathbf{E}}{\partial t^2} = \mu_0 \frac{\partial^2 \mathbf{P}}{\partial t^2}, \quad (6)$$

where \mathbf{P} is the material's polarisation, described by

$$\mathbf{P} = \chi \epsilon_0 \mathbf{E}, \quad (7)$$

using the electric constant ϵ_0 and the medium's electric susceptibility χ , which is a scalar in this case as we assume the waveguide consists of a homogeneous, linear, and isotropic material.

In an ideal waveguide the transverse (x, y plane) field distribution does not vary except for phase as it propagates, so we seek a solution to equation 6 of the form

$$\mathbf{E}(x, y, z, t) = \mathbf{E}(x, y) e^{i(\beta z - \omega t)}. \quad (8)$$

This fundamentally defines an optical mode, where x, y , and z are the Cartesian coordinates, ω is the angular frequency of the light's phase, and β is its constant of propagation in space, given by

$$\beta = nk \sin \theta = n_{\text{eff}} k. \quad (9)$$

In this way θ can be thought of as the angle of propagation of the phase front, or wave vector, relative to the fibre's axis, the magnitude of which is given by k , the wavenumber. This means that β functions as the projection of k along the waveguide's axis, scaled by the refractive index of the material. n_{eff} is the effective index that retards the light's propagation along the waveguide, given by the ratio of the velocity of light in free space to its phase velocity in the waveguide. Because β governs how the phase of the light changes as it propagates along the fibre's axis, it is critically important to the inter-core coupling calculations that will be discussed in chapter 4.

When substituting the mode solution 8 back into equation 6 we obtain

$$\nabla_{\mathbf{t}}^2 \mathbf{E} + (k^2 n^2 - \beta^2) \mathbf{E} = -(\nabla_{\mathbf{t}} + i\beta z)(\mathbf{E} \cdot \nabla_{\mathbf{t}}(\ln(n^2))), \quad (10)$$

where $\nabla_{\mathbf{t}}$ is the gradient operator in the x, y plane. By assuming that the transverse refractive index differences are small by comparison to the average index of the glass (ie. $\Delta n \ll n$, often referred to as the "weak guidance" approximation) then the entire right-hand side can be neglected to give

$$\nabla_{\mathbf{t}}^2 \varphi + (k^2 n^2 - \beta^2) \varphi = 0. \quad (11)$$

Assuming the fibre is weakly guiding also means that the vector field \mathbf{E} must be near parallel at all points across the mode, allowing us to replace it with the scalar electric field φ .

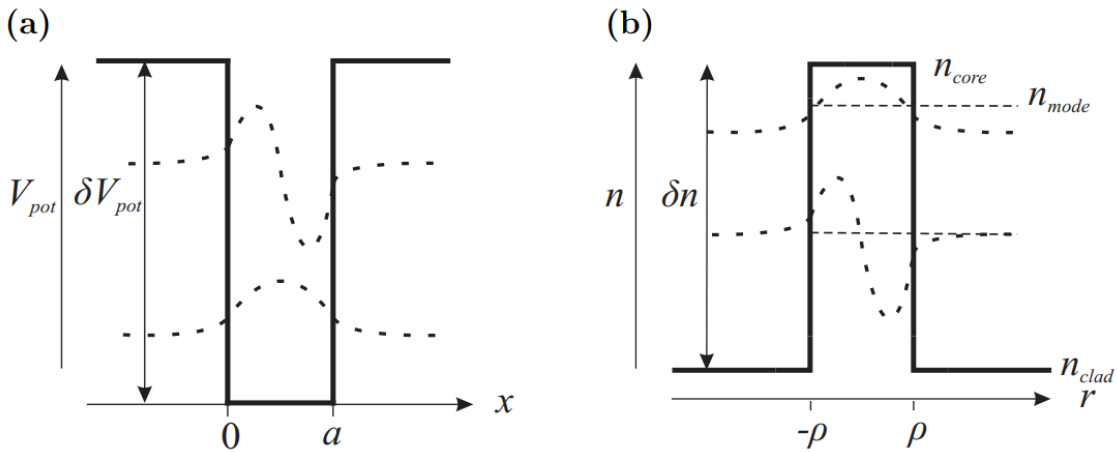


Figure 2.2: A comparison between a) the vibrational modes of an electron in a 1-dimensional finite potential well and b) light in a step index fibre [19].

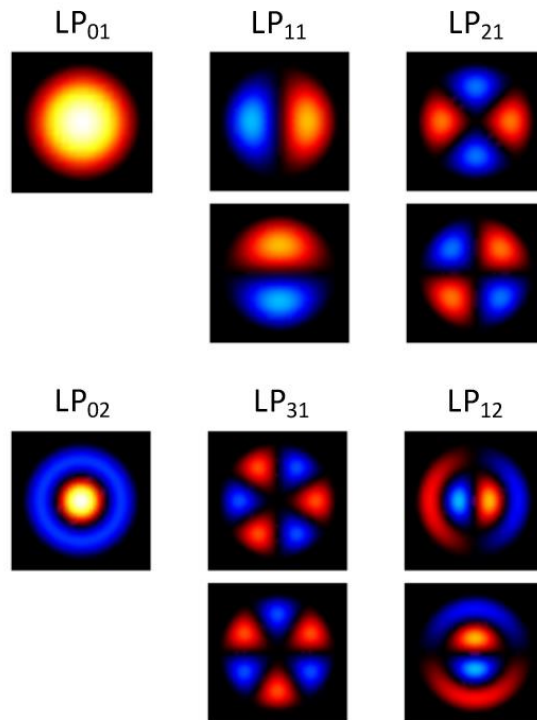


Figure 2.3: Diagrams of the 9 lowest order transverse field distributions of light guided in a step index fibre (reproduced from T. A. Birks' Presentation on Modes) [20].

By noticing the similarity between this equation and the Schrödinger wave equation, oscillatory solutions can be found analogously as shown in figure 2.2. This is achieved by imposing the boundary conditions of the waveguide's refractive index profile in the same way those of a finite potential well would constrain an electron's wave to a specific set of odd and even solutions. In this case we form an eigenvalue equation from the scalar wave equation 11 by ensuring that the fields

drop to zero sufficiently quickly at large distances from the core, and that there are no discontinuities at the core boundaries (or anywhere else). In this way the different propagation constants (β_i) for each bound mode become our eigenvalues. Because the refractive index of an optical fibre varies in 2 dimensions, finding solutions to the eigenvalue equations is not trivial. The 10 lowest order odd and even transverse mode distributions calculated for a simple step index fibre are shown in figure 2.3.

These are described mathematically by a Bessel function of the first kind for the core region, and a modified Bessel function of the second kind for the cladding [21, 22]. This implies an evanescent field extending beyond the core boundary which would classically be forbidden, deepening the analogy with the quantum well.

Although the mode field solutions are best left to graphical or computational methods, the number of guided modes can be found by calculating the core's normalised frequency, or V-value [16, 23], defined as

$$V = \frac{2\pi}{\lambda} \cdot \rho \cdot NA, \quad (12)$$

where ρ is the core radius. It has been shown that a core with a V-value below 2.405 will be single-moded. Values smaller than 2 indicate that the fundamental mode is becoming less well localised to the core, increasing loss. For large values of V, a good approximation of how many spatial modes are guided is

$$M \approx \frac{V^2}{4}, \quad (13)$$

or double this if considering differently polarised modes separately [24].

2.1.3 Silica glass

Glasses are defined by their solid, non-crystalline and amorphous structure at room temperature. In the case of silica, this takes the form of silicon atoms bonded tetrahedrally to 4 neighbouring oxygen atoms, as in figure 2.4. As all the electrons are trapped in covalent bonds, the structure is a dielectric. Because of this, and the fact it has no energy transitions that can be stimulated by visible photons, it is transparent to these wavelengths. When heated above the softening temperature (roughly 1670 °C for fused silica) the glass behaves similarly to a supercooled liquid – it will be soft enough to work with, albeit very slowly, and can deform over its own weight, given enough time. Past the working temperature, 2354 °C, silica's viscosity dips below 10^3 Pa s and so it becomes too fluid to maintain its shape while handling. This broad, nearly 700 °C range in which silica can be worked mechanically is another key reason for its prolific use in the optical fibre industry, and puts it squarely within the long glasses subcategory that are defined by this temperature range. Many short glasses

by comparison will have a working temperature range that spans 200 °C or less [25, 26]. This has meant that it is often preferable to find complex solutions (for example hollow core fibre, discussed later in this chapter) to problems such as silica's absorption in the mid infra-red instead of using soft glasses that are transparent in this range.

Much of the fibre fabrication work described in this thesis was carried out at temperatures ranging from 1900 to 2050 °C, where silica can be stretched, but its viscosity is sufficiently high to prevent deformation of internal gas filled holes and microstructures due to surface tension.

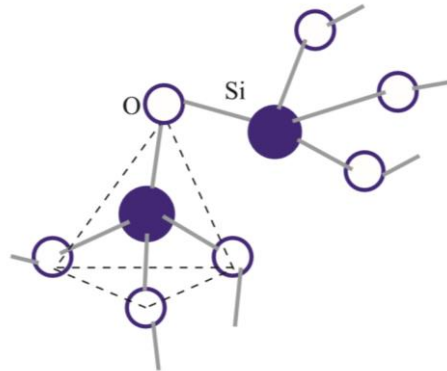


Figure 2.4: A representation of the 3D structure of SiO₂ silica glass. White circles represent oxygen, blue circles silicon [27].

2.2 Photonic crystal fibre

Photonic crystal fibres (PCFs) are defined by a periodic lattice of air holes (or sometimes doped regions) that can be used to form a band gap in the possible values of β , preventing certain wavelengths of light propagating transversely through them [28]. This principle is based on the same physics as describes the band gaps of electron energy levels in a periodic 3D lattice. By omitting a hole from the lattice, a waveguide core is formed as the bandgap effects of the cladding lattice prevent light escaping into it. Figure 2.5 shows the structure of a photonic crystal fibre designed for single mode performance across all wavelengths as the transverse wavevector of higher order modes are permitted within the cladding bandgap, allowing them to escape.

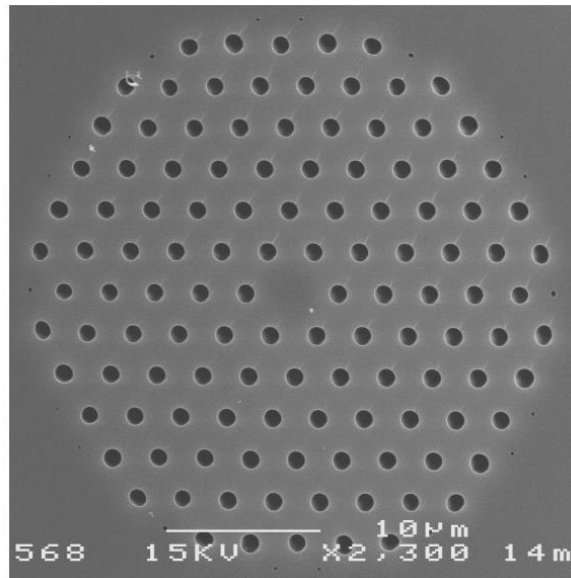


Figure 2.5: A scanning electron microscope (SEM) image of an endlessly single mode PCF [29].

Dispersion refers to the relationship between the speed of a wave in a medium and its frequency. This property is affected both by the refractive index of the material that the wave is propagating in, as well as the waveguide itself. One of the most interesting advantages of PCFs is the ability to engineer their dispersion simply by changing the ratio of the diameter of the holes to their separation [30].

2.2.1 Hollow core fibres

The name PCF has become heavily associated with all glass-air microstructured fibres, regardless of the presence of a bandgap or other lattice effects. One example of what is often referred to as a PCF despite the lack of any photonic crystal structure is the fibre shown in figure 2.6.

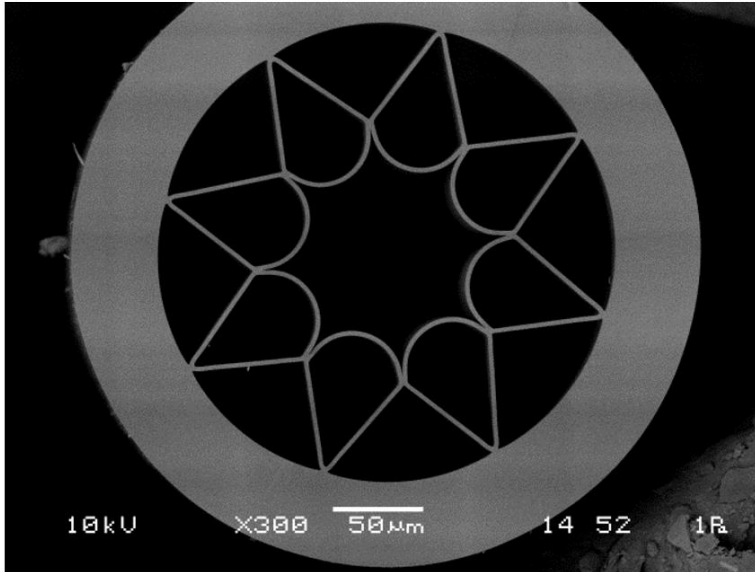


Figure 2.6: An SEM image of a typical negative curvature hollow core fibre [31]. The light regions are pure silica glass, the dark are air-filled spaces. When in use, light is guided in the central, air-filled region due to anti-resonance conditions in the surrounding thin silica webs. Negative curvature fibres derive their name from the inverted curvature of the core boundary.

This is an example of a hollow core fibre (HCF). These fibres guide light within a core filled with air, or sometimes other gasses or even vacuum. In this case, light is being guided in the inverse of the index step discussed in section 1.1. This can be achieved using band gap effects, but more often a phenomenon known as anti-resonance is employed. Theoretically described by the anti-resonant reflecting optical waveguide (ARROW) model [32], the thin glass capillaries that form the cladding act similarly to a Fabry-Perot resonator cavity [31]. If the light incident upon the capillaries is of a wavelength such that an integer number of oscillations can fit within the layer of glass, a cavity mode is formed. In this case the wave can propagate through the glass and be lost from the fibre. If instead the wavelength can only make half integer number of oscillations within the glass, no mode can be formed and so the surface reflects the light back into the core. The capillaries are of a precise thickness such that one of the reflected wavelength bands is at the wavelength intended for guidance. This principle is illustrated in figure 2.7.

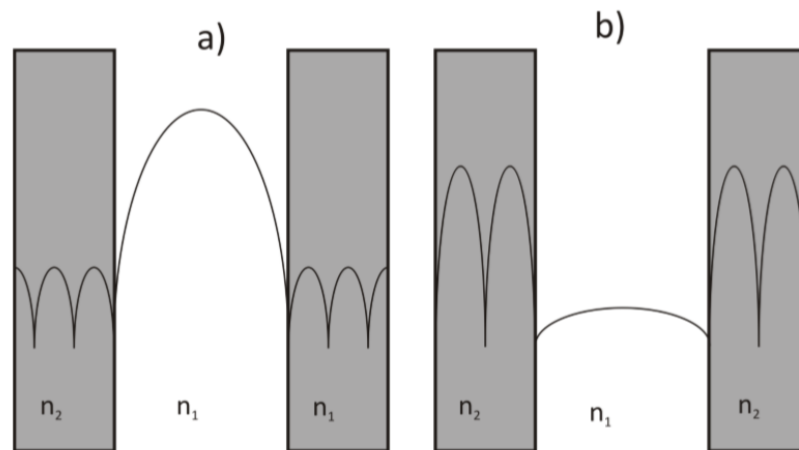


Figure 2.7: Schematic representations of the intensity profile in the core region and first high index regions in the one dimensional planar waveguide, a) is the anti-resonant case where light is confined in the core region by antiresonant reflections and b) is when the wavelength is close to a resonance of the high index regions corresponding to the peak transmission of the Fabry-Perot cavity [31].

The precision fabrication of glass fibres with air-silica microstructures has been refined since the invention of PCF in the mid 90's, and will be briefly described in the following section.

2.2 Techniques

In this section I outline a few of the techniques that underpin the fabrication of optical fibre devices as a whole. This will aid the reader's understanding of the novel science presented in later chapters.

2.2.1 Fibre fabrication

When heated past its softening temperature (roughly 1670 degrees) silica glass can be stretched. The glass is thinned, while preserving and scaling down any internal doping structure. This process, called drawing down, allows complex structures to be fabricated at a macro scale, then reduced to optically relevant sizes. A remarkably useful concept, this underpins much of fibre fabrication. This section describes how these types of technique are used fabricate most basic optical fibres from precursor chemical vapours.

2.2.1.1 Doped preform manufacture

The glass used to make optical fibres at the CPPM fabrication facility usually begins as a meter-long rod, less than 30 millimetres thick. Referred to as preforms, the desired doping profile is already fixed inside the glass during its manufacture. We buy our preforms from external companies such as Draka [33] (a subsidiary of the Prysmian group [34]) who fabricate them using a process called plasma chemical vapour deposition (PCVD). A schematic diagram of this process is in figure 2.8 [35].

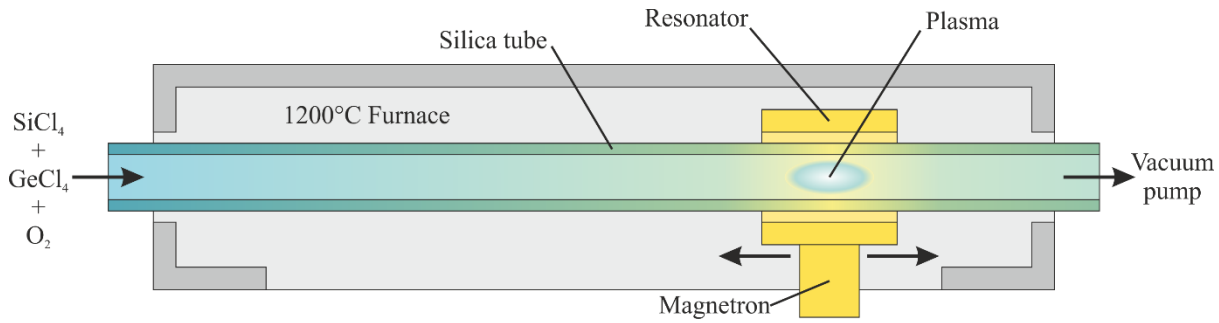


Figure 2.8: A diagram of the PCVD process. [36]

A tube of pure fused silica is placed in a lathe and surrounded by an oven to bring it to around 1175°C , making it ready to act as a substrate. A mixture of SiCl_4 and O_2 gas is pumped down the bore of the silica tube, and a microwave generator sweeps up and down it, irradiating the chemicals to turn them into a non-isothermal plasma. The precursor chemicals react to produce pure SiO_2 soot which fuses to the inside of the tube, and chlorine gas that is extracted. By introducing other chemicals into the gas mix the resulting glass is doped depending on the ratio of the mixtures. Most commonly GeCl_4 or C_2F_4 are used to dope the structure with germanium or fluorine, which raise or lower the refractive index respectively. When the desired doping profile has been built up the remaining hole is evacuated to collapse it, and the preform cooled and removed from the lathe. The PCVD process is capable of building very complex doping profiles, providing they are circularly symmetric. An example of what can be achieved is shown in figure 2.9, an airy pattern fluorine doping profile, used to better accommodate a mode pattern diffracted from the circular aperture of a telescope [37].

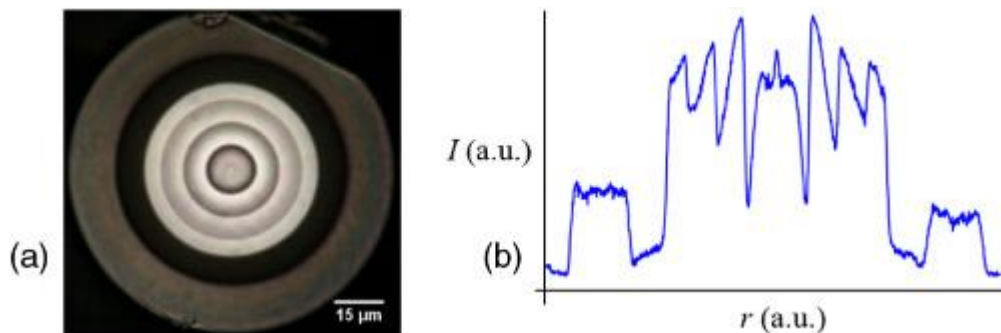


Figure 2.9: a) an optical fibre with an Airy pattern doping profile. b) the measured refractive index as a function of radius. [37]

Other dopants that are frequently incorporated to influence the optical and mechanical properties of the silica include: Fluorine, to decrease the index; erbium or ytterbium, to act as a gain medium; boron, to drastically lower the softening temperature and stress the cooled structure.

2.2.1.2 Drawing down

Drawing down refers to the process of heating and stretching a cane, preform or stack to reduce its diameter. For simplicity, here I will only discuss the techniques relevant to drawing down solid cylindrical preforms to fibre or canes.

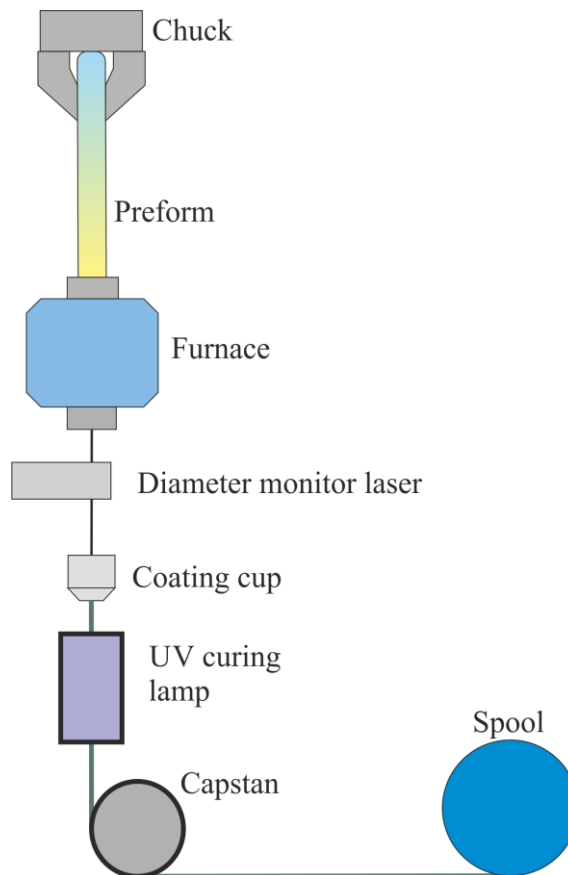


Figure 2.10: A simplified schematic drawing of the optical fibre drawing tower at the University of Bath. The chuck lowers the silica based preform into the preheated furnace, raising its temperature to roughly 2000 °C. A strand of silica is pulled from the bottom of the preform (in the furnace hot-zone). Its diameter is measured by a laser monitor, then it is coated in a thin layer of monomer, which is cured to a tough acrylate polymer by the UV lamp. The fibre is pulled at a steady rate by the capstan, and fed onto a spool.

The procedure, depicted in figure 2.10, begins by clamping the glass in the chuck at the top of the tower, and lowering it so that the tip reaches a couple of centimetres past the hot zone of the furnace. At between 2000 and 2100°C the drop-off process begins. At this temperature the glass is so soft that the small amount of weight below the furnace's hot zone will slowly drop out of the bottom of the furnace, still attached to the preform by a thinning thread of glass. With the drop-off outside, the hanging bulk is broken off. The thread, still attached to the preform neck down region, is used to begin the drawing process.

Sometimes it is desirable to avoid losing particularly precious glass in the drop off. For these times a technique we refer to as “fishing” can be used. This involves lowering the very tip of the preform to the precise centre of the furnace hot zone and inserting a thin silica cane from beneath the furnace to fuse to it. The cane is then used to gently pull a thread of glass from the preform and begin the process. Because material must be conserved, after a short period of stabilisation, the diameter of the fibre is a direct result of the diameter of the preform, the speed with which it is being lowered into the furnace, and that of the fibre being pulled out. The diameter of the glass is measured as it emerges from the bottom of the furnace using a non-contact laser based monitoring device.

Optical fibres are typically less than a millimetre in diameter, so any surface imperfections are significant in scale compared to the whole structure. Therefore, they can easily cause fractures that cleave through the whole fibre diameter if it is mechanically stressed. With a perfect surface, however, glass fibres are astonishingly strong as stress is evenly distributed across the whole covalently bonded structure. For this reason, it is necessary to protect the fibres with a polymer coating before they are allowed to contact anything solid or chemicals that could weaken them. This is done by passing the bare fibre through a coating die which applies the uncured liquid monomer, and then passing it through a high-power UV lamp to cure and polymerise it. After this the fibre is safely gripped and pulled by a capstan at the bottom of the tower and wound onto a large spool.

For the multi-stage fabrication processes that are discussed in subsequent sections it is often necessary to draw canes of uncoated glass, greater than a millimetre thick, as the intermediate stages. For this purpose, the fibre drawing facility in Bath also has a secondary tower to draw canes of glass that are too thick to be bent round a capstan. This cane tower system lacks not only the capstan, but also the coating cup and curing lamp. These are replaced with a pair of motorised belt rollers that clamp onto the cane below the furnace and pull it down vertically. The resulting canes are cut manually, usually to meter lengths, using an alumina cleaving tile.

2.2.1.3 Stacking

The distribution of dopants within a piece of silica is not affected by the drawing process in any way except scale, and the minor effects of diffusion. In addition, by maintaining a temperature lower than 2000°C during the draw, the viscosity of the glass is such that it will retain its shape, and those of any internal air pockets, against the forces of surface tension. This enables the fabrication of fibres with complex cross sections, such as those discussed in the earlier section on PCF, by using stack-and-draw techniques where the desired structure is built up at the millimetre scale using silica canes and capillaries, and then drawn down to optically relevant sizes.

Stacking is done by hand, so is practically limited to a few hundred canes, usually in close packed hexagonal arrangements. A typical example of the progression of stack-and-draw techniques used to prepare PCF is shown in figure 2.11.

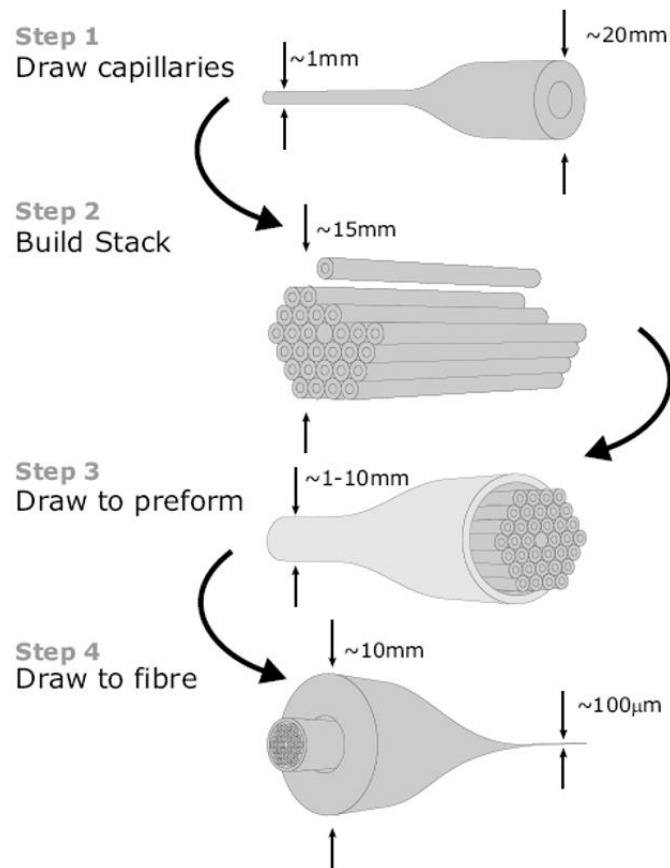


Figure 2.11: A schematic representation of the stack and draw method of PCF fabrication. First, capillaries are drawn from pure silica tubes (1) and are then stacked in a close packed array with the introduction of a defect region to form the core (2). These are drawn down to preforms (3) which are then jacketed in a silica tube and drawn to fibre (4) [38].

With solid fibres a vacuum is usually applied to the top of the preform in the step 4 of figure 2.11 to collapse the interstitial spaces and fuse the jacket tube around the internal structure, forming a solid cylinder of glass. In the case of PCFs this process is more nuanced as the capillaries would also collapse if the vacuum was drawn from the top. Instead, the top can be sealed before the draw, causing the passive pressure of the internal gasses to build up during the draw as the preform is heated, keeping the capillaries open. The interstitial spaces can still be collapsed during the draw by cutting a hole into the outside of the jacket tube and applying a vacuum. Sometimes it is necessary to inflate/deflate the capillaries during the draw through the use of active pressure control. This can be achieved by partially drawing down the top end while pulling a vacuum from the side to collapse the interstitial spaces without completely sealing the capillaries, as in Figure 2.12 (b). Active pressure can then be applied to them through the tapered top end through the use of a brass piece that forms a seal using an internal screw thread and PTFE tape, figure 2.12 (a).

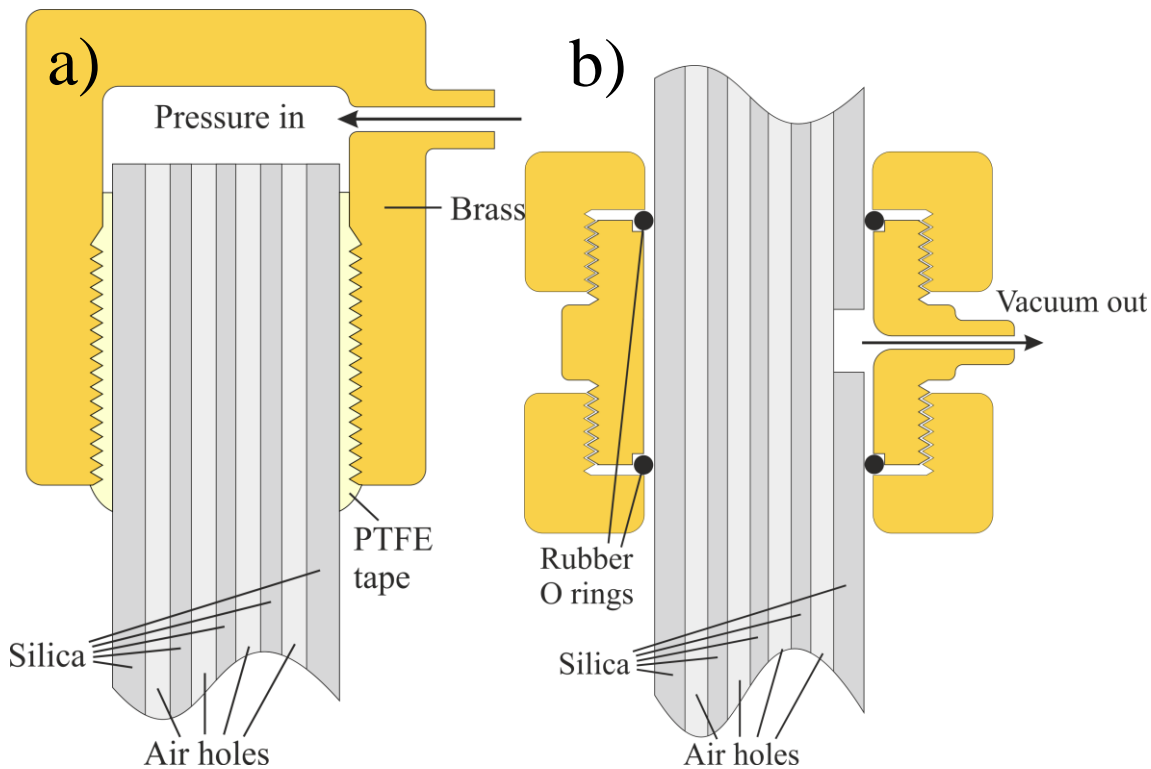


Figure 2.12: (a) A cut-through diagram of a PCF stack with a brass piece screwed on to the top of the jacket tube. Pressure is applied through the brass piece to inflate the air holes during the draw. (b) A similar diagram of a brass collar used to apply a vacuum to a slot cut in the jacket tube. This collapses the interstitial spaces within the contained stack during the draw.

2.2.2 Post processing

This section briefly covers a short list of techniques that are commonly used to terminate fibre ends, prepare them for use in experiments, or alter the waveguide's properties.

2.2.2.1 Cleaving

As mentioned in section 2.2.1.2, any imperfection on the surface of the glass focuses stress and can cause cracks to propagate through the structure. Cleaving is the act of purposefully scoring the surface using a blade of hardness greater than the glass (usually an alumina tile or ruby scribe), and stressing the glass such that the ensuing crack runs through the cross section to produce a flat end face. The energy required to form interfaces between glass and polar fluids is lower than for glass and air, so it can often help the cleave's propagation to introduce a drop of isopropyl alcohol (IPA) or water [39]. The cleaved end of an imaging fibre is shown in figure 2.13. Note the evidence of the original scratch on the bottom side, and the lip on the opposite - characteristic by-products of this technique.

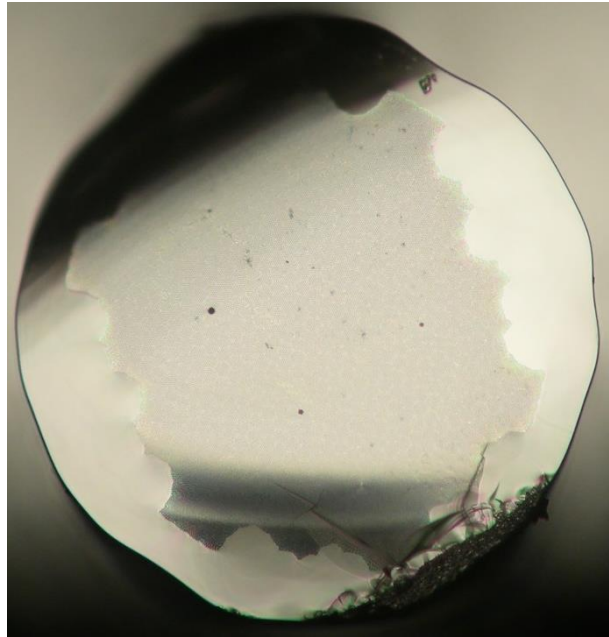


Figure 2.13: An example of a particularly poor cleave on one of my imaging fibres that will be discussed in chapter 4. Note that the crack from the initial score mark at the bottom, and the out of focus lip at the top both extend into the imaging region.

2.2.2.2 Polishing

Although the cores of most fibres are central in the cross section, in the instances where they are close to the fibre's edge (such as in imaging fibres) cleaving artefacts can render them useless. For this reason alone, it is often useful to polish fibre end faces perfectly flat; a laborious process described in detail in Thor Labs' guide [40]. A properly polished fibre will have a perfectly flat end face, and surface roughness only slightly worse than a cleaved fibre.

2.2.2.3 Tapering

Optical fibres can be post processed by tapering their outer diameter down using a rig such as the one in figure 2.14. The fibre is clamped between the two stages, and the flame moved up and down its length. The stages clamping the fibre are moved apart as it is heated, stretching it and decreasing its diameter similarly to the drawing tower. This is a very useful technique for locally changing the waveguide properties to make a plethora of useful photonic devices.

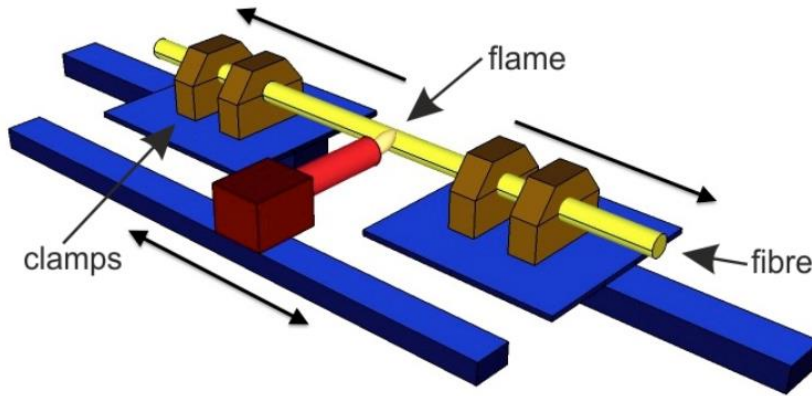


Figure 2.14: An isometric drawing of an optical fibre tapering rig [41].

2.2.3 Characterisation

Several well-established methods for accurately quantifying various parameters of an optical fibre are listed here.

2.2.3.1 Numerical aperture

The NA of a fibre can be found by the knife edge measurement: Two blades are placed on a translation stage to form a slit in front of the fibre end, with a large area detector behind them. By scanning them across the cone of emitted light an intensity profile can be built up. The edge of the beam is taken to be at some fraction of the maximum power (usually either $1/e^2$, $1/e$, or $1/10$ in industry standards), and by measuring this at different distances from the fibre end the angle of the cone, and therefore the fibre NA, can be calculated. This can also be done using just one blade by taking the derivative of the power with respect to the blade's position as it moves across the beam. In chapter 6, I use this method to characterise one of the cores of one of my novel imaging fibres with unknown NA.

2.2.3.2 USAF resolution test targets

Since the 1950s the United States Air Force (USAF) has produced several test targets designed to act as standard images for the characterisation of imaging devices. These are usually used to find the smallest resolvable feature of imaging fibres. In chapter 4, I present several imaging fibres that I fabricated for this project, most of which were characterised using the targets in figure 2.15 as we found them to be the most commonly used ones in literature.

Positive test targets consist of a glass microscope slide with successively smaller sets of perpendicular lines of chromium coating, etched from a whole layer using photolithography. Negative test charts are simply the inverse; the design is etched out of the chromium so that light can pass through the lines and numbers, but not through the blank regions of the target.

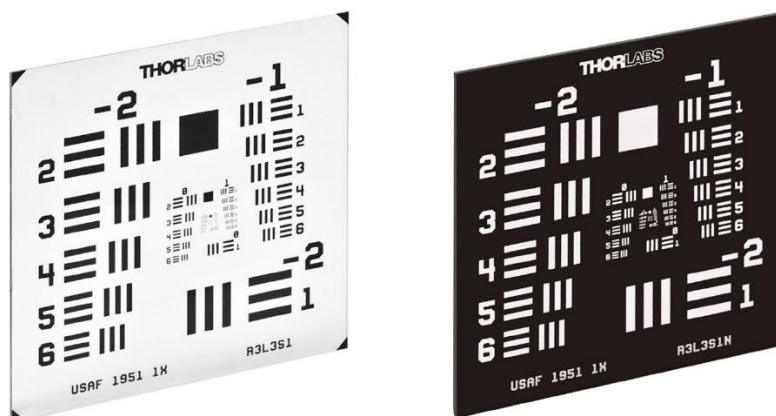


Figure 2.15: Positive (left) and negative (right) USAF test targets.

Test targets allow the maximum resolution of an imaging fibre to be investigated by butting the fibre up against the section of the target corresponding to the spatial resolution of interest and lighting it from behind, in our case, with a beam of supercontinuum light. The lines are arranged in pairs, three horizontal and three vertical lines of identical dimensions, with the gap between each line being the same as the line's thickness. The lines are five times longer than they are wide, meaning each triplet within each pair is square, allowing astigmatism of optics to be tested. These pairs of line triplets are called elements, and are arranged into groups of 6 elements (corresponding numbers are beside each element) with the group's number above it. For example, the bottom left set of lines in each image in figure 2.15 is element 6 of group -2. The resolution of an optical system is found by observing the smallest element in which the lines can be distinguished from each other, and finding its dimensions in a lookup table.

2.2.3.3 Dispersion

A fibre's group velocity dispersion (GVD) refers to the relationship between light's wavelength and the propagation speed of pulses of light. It is directly related to the propagation constant by

$$\text{GVD} = -\frac{2\pi c}{\lambda^2} \beta_2, \quad (14)$$

and so can be used to infer some of the coupling characteristics of neighbouring cores. To measure a fibre's GVD, we use an interferometer that is based on the Mach-Zender design [27]. The fibre is incorporated into one of the interferometer's beam arms and a delay line is used to match the optical delay of each arm, producing interference that is read out by a photoreceiver. In my case, I have modified the setup used by my group to include a flipper mirror and CCD camera, figure 2.16, to facilitate characterising multi-core fibres.

A visible supercontinuum is used as the light source so that wavelengths can be selected using a band pass filter before the collection fibre, and because of its short coherence length which means

that interference will only be observed when the optical delay of the two interferometer arms is matched precisely. By comparing the delay arm's position with and without the fibre in the setup, the fibre's contribution to the delay can be calculated. Using visible bandpass filters to measure this group delay at different wavelengths allows the GVD to be measured.

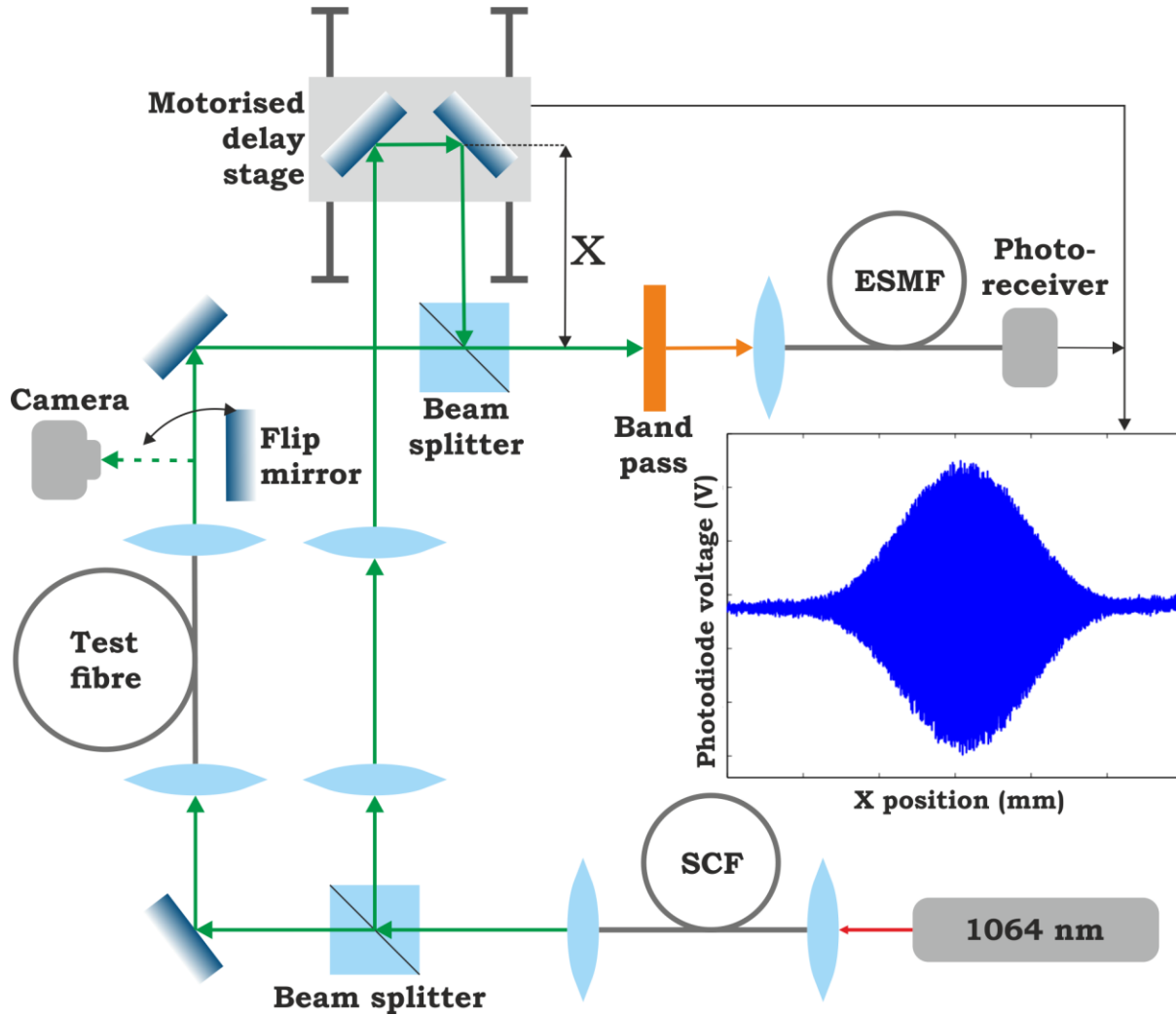


Figure 2.16: A schematic diagram of the optical setup I have used to characterise the dispersion of optical fibres. The 1064 nm pulsed microchip laser is used to pump the supercontinuum fibre (SCF), generating white light. The bottom beam splitter sends half the beam through the test fibre, and the other half through free space and a pair of lenses identical to those used to couple to the test fibre as a reference. A flip mirror and camera can be used to monitor the output of the test fibre. A delay stage is used to alter the reference arm path length, and the beams are recombined. Band pass filters are used to investigate changes at different wavelengths. By coupling the light into a length of endlessly single mode fibre (ESMF) before the photoreceiver, the beams are effectively recombined, irrespective of their original mode content. The delay arm position is swept, and interference fringes are observed from the photodiode when the optical delay in each arm is identical.

Chapter 3

Sensing

3.1 Introduction

As discussed in the previous chapter, optical fibres are key components in endoscopic systems for retrieving optical signals from otherwise inaccessible locations. Traditionally such signals are images, but there is increasing interest in endoscopic systems that incorporate spectroscopic mechanisms of in-vivo diagnosis, with all the bulky, but essential, instrumentation attached to the proximal end of the fibre [42]. The concept of using sensing fibres in conjunction with the more traditional imaging fibres was included in Proteus' main goals, potentially representing a major leap in endoscope technology.

This chapter explores the different methods used by the Proteus team to overcome the challenges associated with making a functional spectroscopic sensing channel in an endoscope; first in terms of previous work, then the work of the author, and finally what this aspect of the project has evolved into.

3.2 Fluorescence spectroscopy

Fluorescence is the process by which electrons in a compound absorb energy from incoming photons, increasing their energy level, and subsequently transitioning down and reemitting some of that energy as photons. An electron's descent through its energy levels is rarely a one-step process. Usually it involves several non-radiative steps, and so energy is lost to heat and acoustic bond vibrations. This means that the emitted photon usually has lower energy than the absorbed one did – an energy change that is specific to the fluorescent compound.

Chemicals can be designed to only fluoresce under certain circumstances, for example when bound to a specific protein, or cleaved by an enzyme. This has been used to produce markers that will only fluoresce in the presence of specific pathogenic antigens in a process known as immunofluorescence [43, 44]. Fluorophores have also been made that activate in the presence of chemicals indicative of the human disease response [45], or physiological characteristics such as pH or oxygen saturation [46]. This technology is often used in conjunction with imaging systems as in

figure 1.3 of chapter 1. In this case, the sensors are usually unable to detect subtle changes in the fluorescent spectra.

3.2.1 Work from Proteus

Proteus chemists have produced several different types of immunofluorescent compounds designed to mark different types of bacteria [47,48]. These have mainly been used with imaging fibres to help identify bacteria in the distal lung. They have also been investigating the use of several different fluorophores that react to changes in pH or oxygen saturation as, in the context of the distal lung, they can be strong indicators of disease and dysfunction [49].

Separating out the fluorescent contributions of the small volume of fluorophore from the background fluorescence of both the lung and the fibre itself is one of the main challenges of integrating this technology into endoscope systems. Proteus researchers at Heriot Watt university have been developing single photon avalanche detector (SPAD) arrays that have the temporal resolution necessary to solve this issue [50]. Our researchers in Edinburgh have also been working to solve this issue by increasing the signal from the sample. They achieve this by infusing porous polymer structures with the fluorophore, providing a far greater surface for the interaction to take place on [51].

3.2.2 Optical fibres from Bath

Several optical fibres have been fabricated in Bath to carry the excitation light to the fluorophores and return the signal light to the detectors, the first of which was fabricated by Dr. Fei Yu. Made using the standard hexagonal stack and draw technique outlined in chapter 2, it included 19 multi-mode cores with 15 μm diameter parabolic germanium doping profiles.

The end of the fibre was etched using hydrofluoric acid, producing pits at the cores as the doped glass etches faster. This allows spheres of fluorophore-infused polymer (usually TentaGel [52]), produced in Edinburgh, to be embedded securely in the fibre end, precisely in the path of the illumination. A scanning electron microscope (SEM) image of the end of Fei's fibre with TentaGel spheres in some of the etched core pits is shown in figure 3.1.

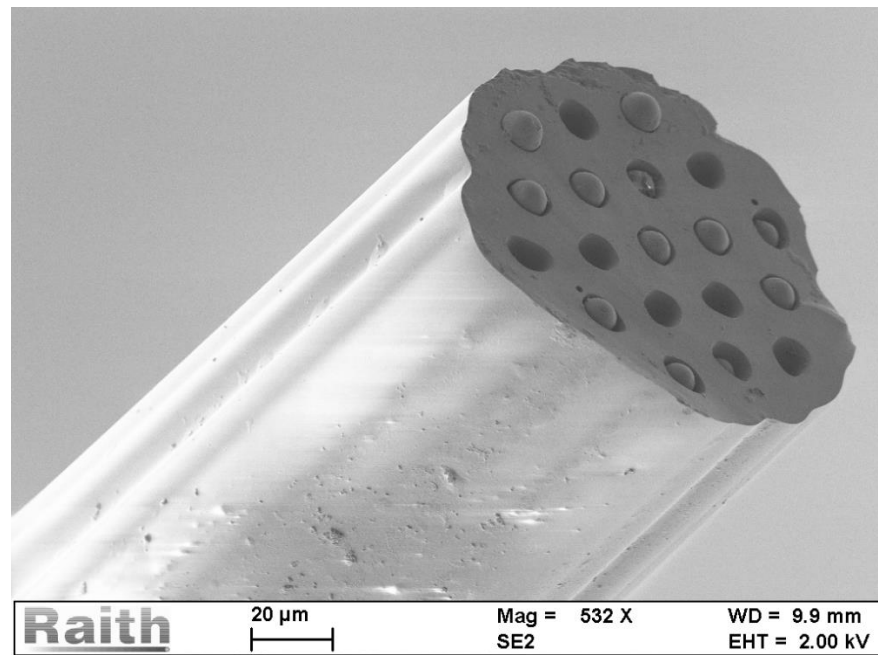


Figure 3.1: An SEM image of Fei's 19 core sensing fibre with TentaGel spheres embedded in the acid etched core pits.

The irregular outer boundary is due to the lack of packing glass to fill the spaces between the edge of the stack and the relatively thin jacket tube.

To familiarise ourselves with the cane and fibre drawing towers, Kerrienne Harrington and I fabricated a similar fibre for the project. It had 20 μm diameter cores, to complement the most recent batch of spheres produced in Edinburgh, and a more circular cross section for increased strength. An image of the end of one of these fibres is shown in figure 3.2 with higher order modes clearly visible. A cohort of Proteus chemists used this fibre to produce a publication titled Controlled core-to-core photo-polymerisation – fabrication of an optical fibre-based pH sensor [51]. In it they show that by photo-polymerising fluorescein O-methacrylate and PEG diacrylate onto the cores at the distal fibre end face it can act as a pH sensor, and demonstrate that it is capable of resolving changes in pH as small as 1. Figure 3.3 shows the fluorescence intensity data they obtained using the fibre probe in solutions of different pH.

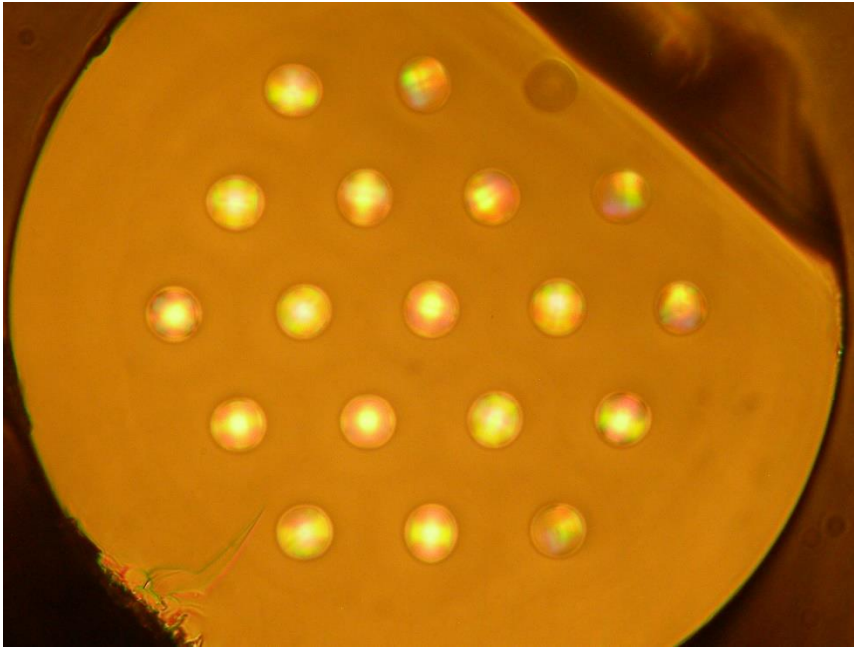


Figure 3.2: An optical microscope image of the cleaved end our sensing fibre. There are 19 cores of 20 µm diameter, with a parabolic doping profile.

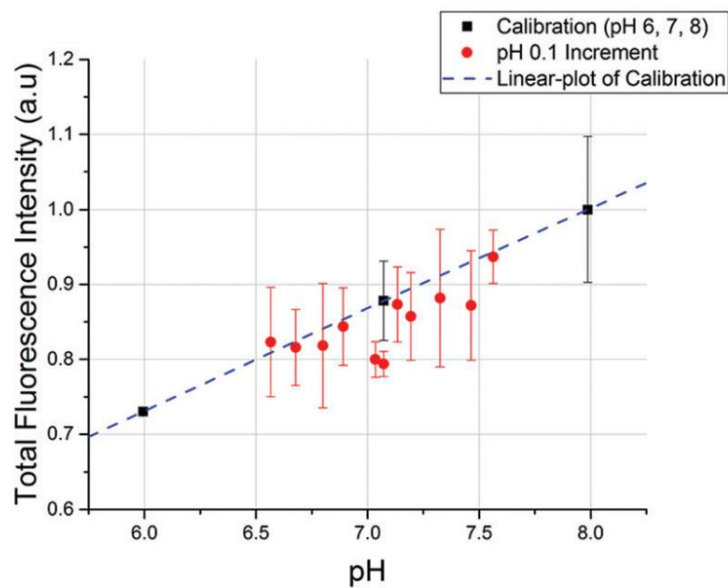


Figure 3.3: Fluorescence intensity data of photo-polymerised fluorescein O-methacrylate and PEG diacrylate on the distal end of the cores of the fibre in figure 3.2, exposed to different pH solutions. The black points are calibration data taken by increasing the pH from 6 to 8 in steps of 1, and the red points were obtained by randomly changing the pH from 6.6 to 7.6 in 0.1 increments [51].

3.3 Raman spectroscopy

In the previous section I discussed fluorescence spectroscopy – a method that uses electron energy transitions for analysis. In this one I will discuss another spectroscopic technique that instead explores a compound's vibrational energies.

Chemical bonds are flexible and have a number of degrees of freedom of movement (rotation, stretching, flexing etc.) based on their structure. The vibrations of these bonds are unique to their specific circumstances; for example, the vibrational modes of a carbon-carbon bond in ethane will be changed if one of the carbon atoms exchanges a hydrogen for a heavier iodine. Bonds can interact with light through Stokes and anti-Stokes scattering. These are inelastic processes where a photon either loses (Stokes) or gains (anti-Stokes) some energy to respectively absorb or create a vibration in the interacting bond. In lattices these vibrations can move through the structure as phonons. The amount of energy exchanged with the photon is specific to the vibrational modes of the bond, so the resulting spectrum will be distinct for any given set of bonds. This allows the compound to be identified to an extremely high degree of accuracy.

Because it is rare for a photon to encounter an actively vibrating bond it is more common for Stokes scattering to occur, although the number of excited bonds does depend on temperature. This has resulted in most Raman spectroscopy setups specifically investigating Stokes scattered light, usually using a long-pass filter to remove both anti-Stokes and Rayleigh scattered light. Raman scattering strength increases with the fourth power of the excitation frequency [53], so one might think that the shortest possible wavelength excitation source is desirable. In fact, the choice of excitation wavelength is also affected by other factors, for example; absorption in the sample's surface decreases the volume of it that can interact with the light, reducing the signal, and if the light can excite photoluminescent transitions in the sample (or potentially in the substrate or surrounding material) then the resulting emissions can overwhelm any Raman signal.

By comparison to fluorescence, the number of photons that undergo Raman scattering is vanishingly small. Rayleigh scattered excitation light is also a factor of 10^4 to 10^6 stronger than Raman scattering [54]. Therefore, to achieve an adequate signal to background ratio, it is necessary to filter out more than 10^5 of the Rayleigh scattered light. Usually a cooled detector and high efficiency gratings are also used when the signal is small.

The spectrum obtained from a Raman experiment is usually expressed in terms of intensity at a given Raman shift, or wavenumber, in cm^{-1} . This is calculated as

$$\Delta w = \left(\frac{1}{\lambda_0} - \frac{1}{\lambda_R} \right) \times 10^7 \quad (15)$$

where Δw is the shift in cm^{-1} , λ_0 is the excitation wavelength in nanometres, λ_R the Raman shifted wavelength in nanometres.

Several methods can be used to enhance the signal, the most common of which is Surface Enhanced Raman Spectroscopy (SERS). SERS takes advantage of the increase in local electromagnetic field strength that results from the surface plasmon effects of light interacting with materials that possess a large number of delocalised electrons for the light to couple to. In practice this usually means using transition metals, and particularly gold or silver nanoparticles [55, 56]. Increasing the field strength in this way increases the Raman scattering signal by up to 10^{10} [57] without risking thermal decomposition of the analyte, which would be the case if higher laser powers were used.

3.3.1 SERS in Proteus

Mercaptobenzoic acid (MBA) has a hydrogen ion that freely dissociates (deprotonates) as shown in the chemical diagram at the top of figure 3.4 – the acidic group COOH becomes COO⁻. This process works to establish an equilibrium with the hydrogen ions that are already in solution, so the extent to which the MBA dissociates depends on the pH of the solution it is in. The loss of the hydrogen from the acid group produces the changes in the peaks of its Raman spectrum seen at roughly 1700 and 1450 cm⁻¹ in figure 3.4. By comparing these peaks to the unchanged reference peak at 1600 cm⁻¹ the pH of the solution can be measured [58]. Proteus chemists in Edinburgh have functionalised gold nanospheres with MBA to produce a SERS probe with a Raman spectrum that depends on pH.

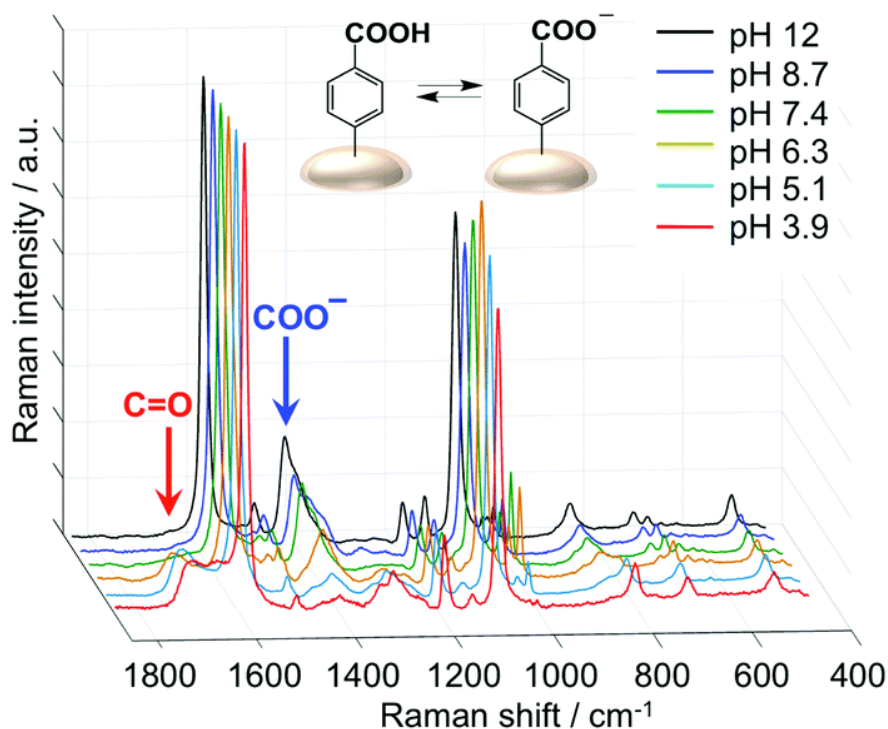


Figure 3.4: The SERS response of MBA functionalised nanoparticles in different pH solutions. Taken from [59].

Samples of these nanoparticles were provided to Bath along with instructions on how to bind them to silica glass. This allowed us to investigate various optical fibre devices as the potential channel of a bronchoscope's SERS probe. The following section discusses the main challenge associated with this prospect. The subsequent sections detail our approaches to solving it.

3.3.2 Raman background problem

Silica glass, and therefore optical fibres, also have an associated Raman response, shown in figure 3.5. It is an awkwardly broadband response that extends from 0 to 1750 cm^{-1} that results from a combination of the amorphous structure and its dangling bonds [60]. The length of fibre used in endoscopy means there is a far greater volume of silica for the light to interact with than whatever sample is at the distal end, leading to any signal within this spectral region being irretrievably overwhelmed.

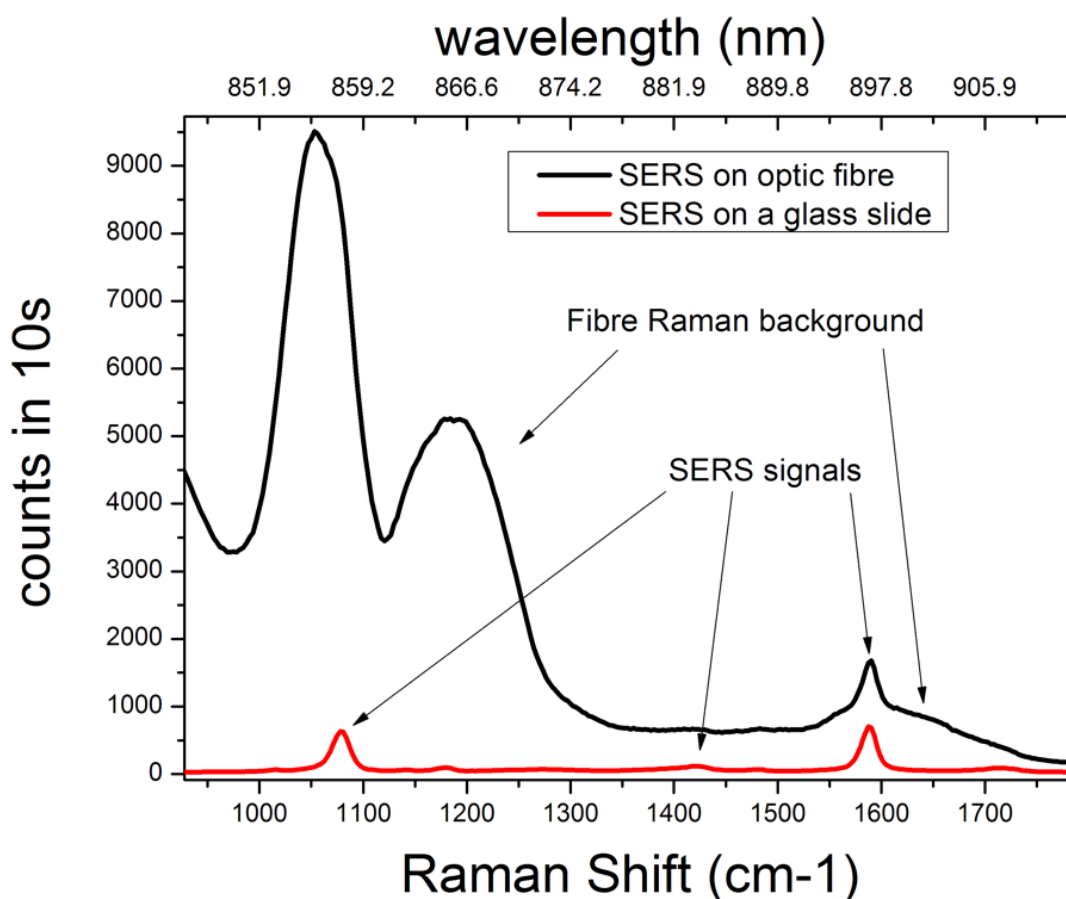


Figure 3.5: A comparison of the SERS response from MBA functionalised nanoparticles with and without an optical fibre for excitation and signal collection.

Solving this problem is a challenge that has been taken up by Proteus' optical fibre researchers in Bath, comprising a significant portion of the first year of my PhD. In the following sections,

several of the concepts for reducing the silica background and recovering an acceptable level of signal are discussed. The simplest aspect of our overall design philosophy was to reduce the amount of glass the pump light interacts with, minimising the amount of background generated in the first place. The signal collection efficiency was also maximised using large, multi-mode collection cores.

3.3.3 Photonic lanterns

Our first concept for a reduced background SERS fibre sensor was based on a photonic lantern, the design of which is shown in figure 3.6. Photonic lanterns are post processed fibre devices. The process of making one begins by taking a multi-core fibre in which each core supports a single mode, and jacketing it in a fluorine doped capillary using the tapering rig discussed in chapter 2. The rig is then used to collapse a region of the jacketed fibre to the point where the cores are too small to guide. This causes the light to couple into the modes of the multi-mode core formed by the index step between the fluorine doped silica and the pure or germanium doped silica of the fibre. Figure 3.6 shows an example of a photonic lantern, where (a) indicates the untapered multi-core fibre, (b) the fibre jacketed by a fluorine doped silica capillary (shown in grey), and (c) the multi-mode end.

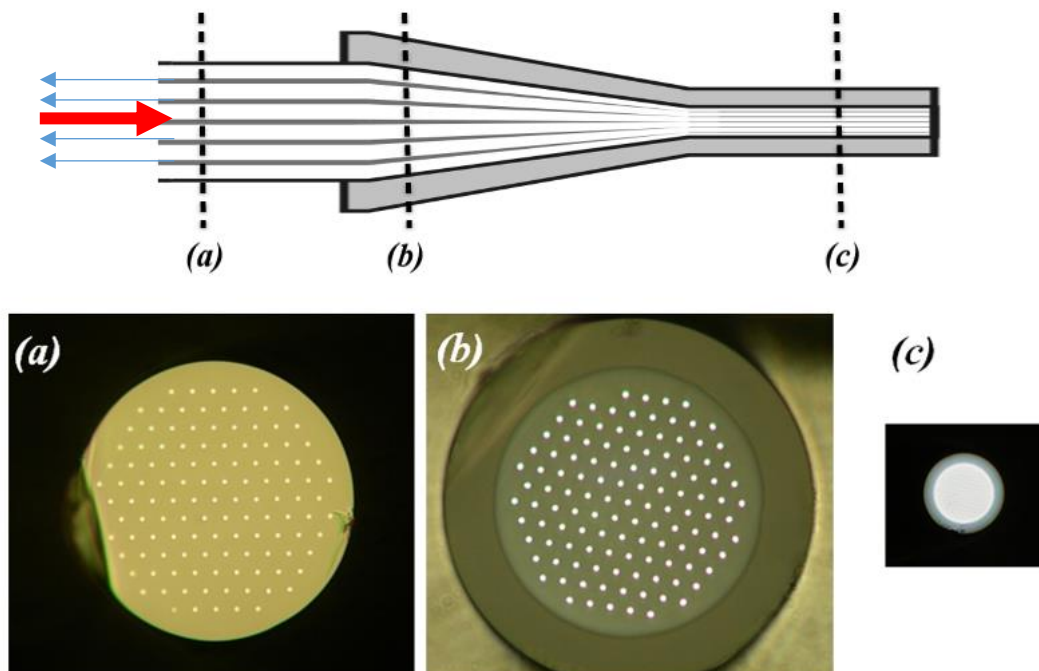


Figure 3.6: A diagram and cross sections of a typical fibre based photonic lantern; the unjacketed, multi-core, single-mode region of outer diameter $230\ \mu\text{m}$, labelled (a), the same fibre with a fluorine doped jacket (b), and the multi-mode region with a $50\ \mu\text{m}$ core (c). The red and blue arrows indicate the paths of the excitation and signal light, respectively, in our design for a background-suppressing SERS fibre lantern probe [61].

In the case of our SERS sensor, one single-mode core guides the excitation light to the multi-mode end face, where it spreads and excites a large quantity of SERS particles. The signal light is initially captured by the wide multi-mode core's end face, then, after the taper transition, guided back via all of the single-mode cores. The back-scattered light returning from the excitation core is removed by spatial filtering – sacrificing a single core's signal to remove the greatest source of back-scattered Raman and fluorescent background.

The SERS nanoparticle samples provided by Proteus' Edinburgh based chemists were supplied as a water-based colloid, so over time the particles settled to the bottom of their container. This necessitated a 5 minute stint in an ultra-sonic bath to break up any clumps of settled nanoparticles. After this the colloid was put in a centrifuge at 5000 rpm, for one minute at a time, until the bottom of the phial contained a loose slurry - ideal for high density coating of fibre ends. Attaching the nanoparticles to glass required the surface to be pre-treated with poly-l-lysine (PLL) and left to dry. The particles readily bound to the dried polypeptide. An example lantern end with good coverage of PLL and nanoparticles is shown in figure 3.7. This was achieved by placing 3-5 μl of the colloid slurry, fresh from the centrifuge, on a slide and pushing the fibre tip through it.

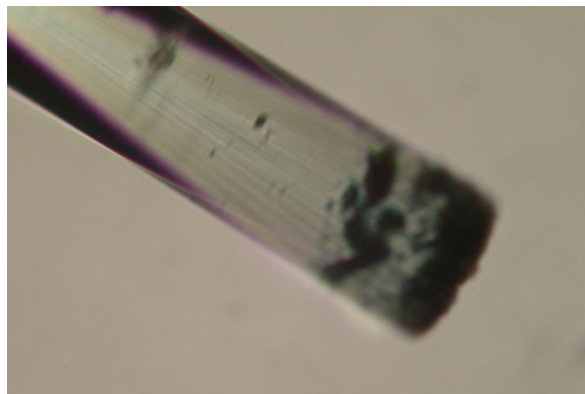


Figure 3.7: The roughly 60 μm wide multi-mode end of a 37-core photonic lantern that has been coated with PLL and SERS nanoparticles

This particular concept was investigated simultaneously to those detailed in the following two sections. Although it helped refine the technique of depositing SERS particles on fibre end faces, the greater promise of the following designs meant that this particular one was never properly tested.

3.3.4 Little & large core fibre

An extension of the photonic lantern idea, Dr. Fei Yu designed this fibre with a small, single-mode, excitation core and a highly multi-mode signal collection core, with a diameter of over 20 μm . Figure 3.8 shows an optical image of the fibre's end face.

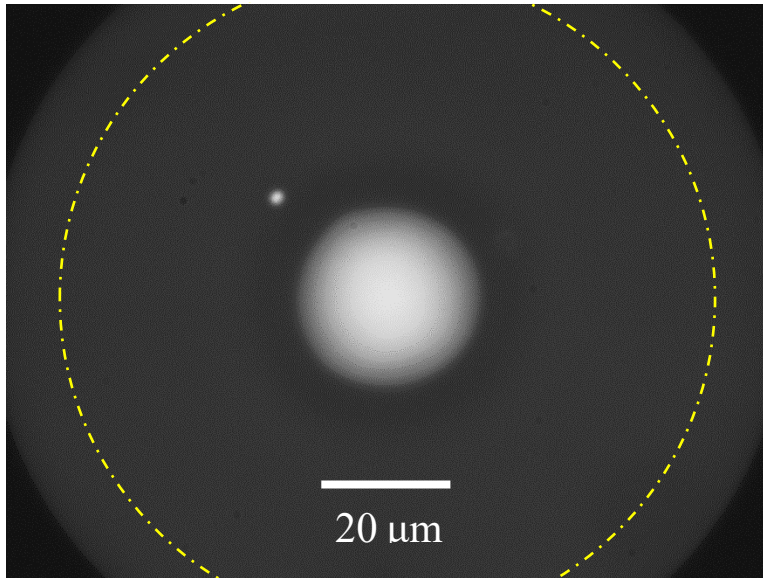


Figure 3.8: An optical image of the cleaved end of the little-and-large core fibre with both cores excited. The dashed circle indicates the position of the 100 μm core of the multi-mode fibre that was subsequently spliced on.

A length of 100 μm core fibre was spliced to the end and cleaved back so only 2 mm remained. This spread the excitation light from the small core over the 100 μm diameter core to excite the maximum amount of SERS. The signal light was then guided back via the large core with high collection efficiency. Again, light returning from the small excitation core is spatially filtered out as it contains the majority of the fluorescent and Raman background.

This method showed some promise, but the spliced 100 μm core fibre was difficult to cleave sufficiently short to prevent excessive background generation. The fibre was taken to Edinburgh where Heriot Watt's optical physicists achieved a good splice and machined silica end caps for it. They published results from the fibre in 2017 [62].

3.3.5 Hollow core fibre

The basic theory of these types of fibre was discussed in chapter 2. Because hollow core fibres guide light in an air-filled core, the Raman background generated by the surrounding silica should be several orders of magnitude lower than with solid core fibres.

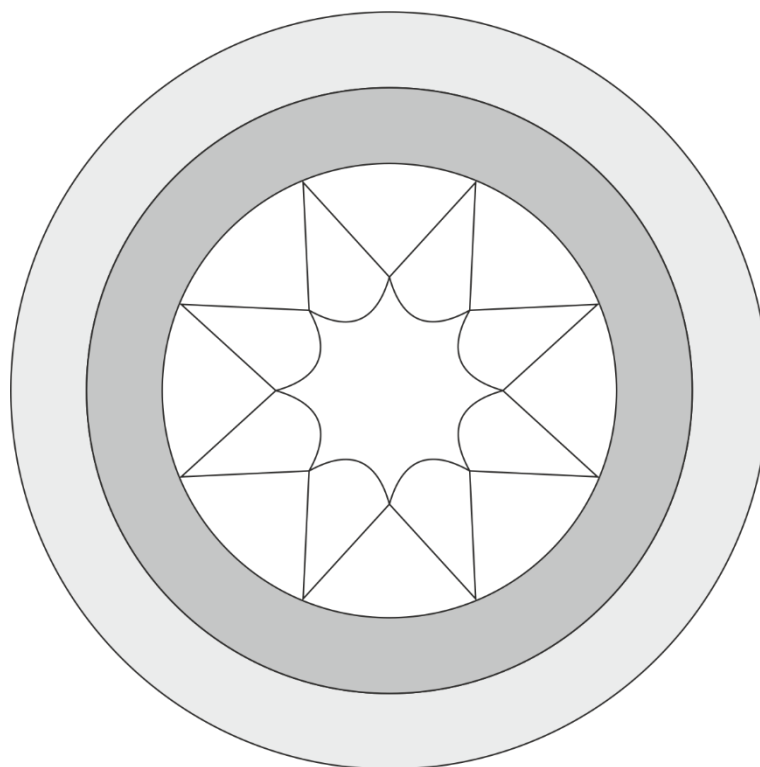


Figure 3.9: A schematic diagram of an anti-resonant negative curvature hollow core fibre. The fine, ice-cream cone shaped structures are pure silica webs that form the air-filled anti-resonant structure, with a central core boundary that has negative curvature. The darker internal ring represents solid, pure silica, and the lighter, external ring is the fluorine doped silica outer jacket.

The numerical aperture of hollow core fibres is small, so the collection efficiency of scattered light from SERS particles is very low if unaided. For this reason, Dr. Fei Yu fabricated a negative curvature hollow core fibre with a fluorine doped silica jacket surrounding the standard silica & air structure, as shown in figure 3.9.

Fluorine doped silica has a lower refractive index than pure silica, so the jacket-core boundary in figure 3.9 guides light through total internal reflection. The fibre end can be collapsed on the taper rig to seal the end, and provide a large multi-mode core to illuminate, and capture light from, the maximum sample area. The return path of the signal light is in the silica inner cladding.

The setup in figure 3.10 was used to test the fibre using a Renishaw Raman microscope as the spectrometer. The microscope's own beam was blocked, and a 785 nm laser was used as the excitation source, producing the spectra in figure 3.11.

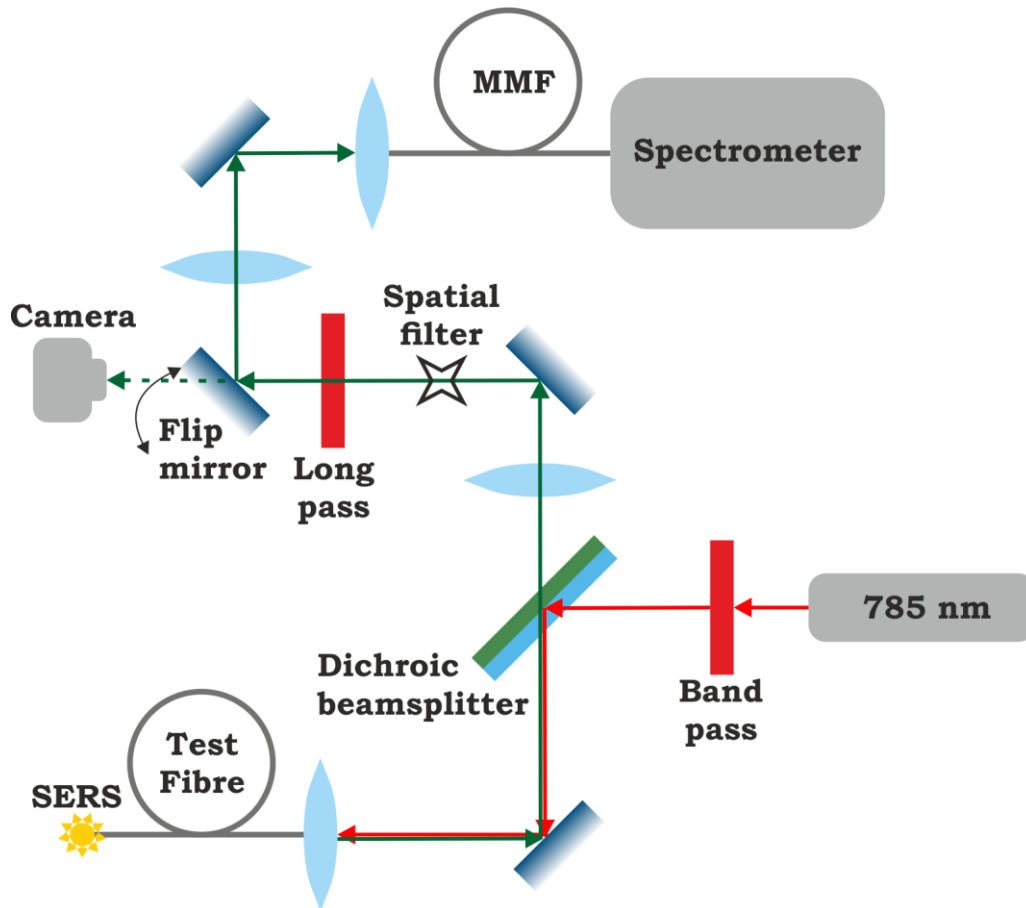


Figure 3.10: A diagram of the setup used to test the various SERS fibre devices. The 785 nm laser was initially filtered to refine its spectrum, before being reflected from a dichroic beamsplitter and coupled into the test fibre, exciting the SERS particles on the distal end. In the single-pass arrangement of this experiment, the signal light was collected directly from the fibre's end using a Raman microscope. In the final experiment the signal light was guided back through the collection cores, coupled out and passed through the dichroic beamsplitter again, separating out the majority of the returning pump light. The lens after the dichroic beamsplitter formed an image of the fibre's output at the spatial filter, which removed any remaining light returning from the excitation core. A flip mirror was used to ensure correct alignment of the spatial filter system. The remaining signal was coupled into a multi-mode collection fibre (MMF) and fed into the spectrometer.

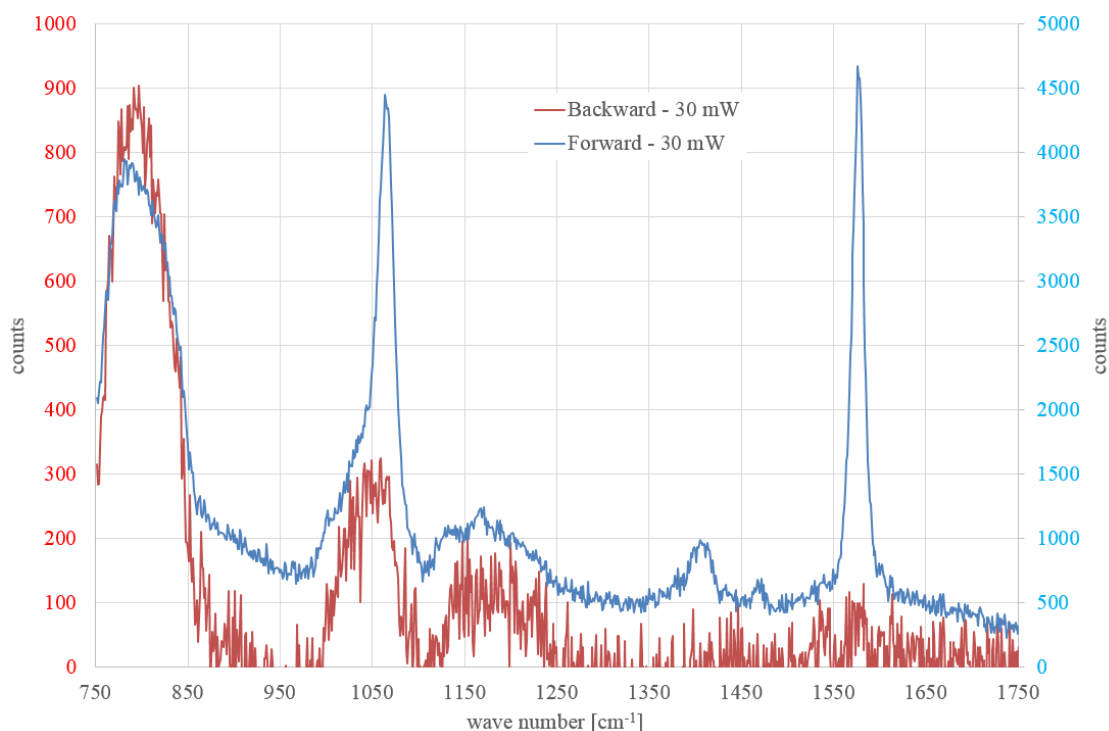


Figure 3.11: Raman spectra of MBA functionalised SERS particles, obtained using the Renishaw microscope and the double-clad hollow-core fibre. The blue trace is the data gathered with the light passing through the fibre only once. The red trace is where the light is coupled down the fibre, and the backscattered light is collected and returned by the fluorine doped outer cladding. Both were taken using 30 mW of laser power and 30 seconds of integration time.

Limited success was achieved using this method. The first set of data was gathered with the collapsed distal, SERS-coated, fibre end directly under the microscope objective to allow the measurement to be made in a “one-pass” regime. The second set of data was gathered using the “double pass” setup where the fluorine doped outer cladding guides the backscattered light back to the detector. In both datasets the Raman background is far lower than with any previous experiment. However, most of the signal light was lost on the return path, likely due to the difficulty in aligning such a complex experiment.

This experiment did prove that the hollow core fibre could guide light without generating background, but research ceased when Dr. Fei Yu left the project in 2016. Dr. Stephanos Yerolatsitis continued this research when he joined in late 2016, and has since published a paper on it [63].

3.4 Conclusion

In this chapter I have discussed several novel, fibre based, endoscopic sensing probes that were designed to enhance the signal to noise ratio. Most of these designs achieved this by reducing the excitation light's interactions with the fibre's silica glass. The work done to produce a photoluminescence sensing fibre ultimately led to a simple design with 19 multi-mode, graded index cores. The end face was etched and sensing beads were embedded, or polymerised, directly in the path of the excitation light. This was published in the Journal of Biomedical Optics [48].

During the studies into surface enhanced Raman probes we found that, out of the all-solid fibre designs, the fibre with a small excitation core and a large core for signal collection was best able to improve the signal to noise ratio by approximately a factor of 100 by reducing the silica Raman background. It was also a comparatively simple and scalable design, and has been used to produce a publication in Optics Express [62]. We found that the ultimate Raman sensing fibre would require the use of a hollow core fibre to guide the excitation light as this can reduce the background by a factor of more than 1000. Work to perfect this is still ongoing, but has recently yielded a paper in Optics Letters [63], where they also demonstrate that the background is suppressed sufficiently to observe intrinsic Raman signal from organic compounds.

Chapter 4

Imaging fibres

Chapter 1 explained the significance of imaging fibres from a historical, a commercial, and the Proteus project's perspective. Building on the basic fibre fabrication tutorial in chapter 2, the first two sections of this chapter cover the challenges of designing and fabricating effective imaging fibres, the approaches commonly taken to overcoming them, and the relative effectiveness of different designs. From section 4.3 onwards I discuss the progress that the Proteus project has made in this field of research, with a particular focus on my own work and contributions. The latest iterations of the project's imaging fibres have led to the completion of critical project milestones and papers [64], to which my academic and practical contributions have been instrumental.

4.1 Inter-core coupling

If the fields of modes are overlapped, they will interact and exchange energy in a process called coupling - also referred to somewhat interchangeably as crosstalk. As discussed in chapter 2, evanescent fields extend beyond the index boundaries of cores. This means that modes can couple together even past core boundaries [65]. Therefore, a good understanding of coupled mode theory is essential to the design and fabrication of any multicore fibre, especially when the cores are so densely packed as is necessary in imaging fibres. In these fibres crosstalk of light from one core to its neighbours effectively blurs the image [66]. This section will explain how coupled mode theory has influenced the designs of both commercial imaging fibres, as well as those produced during this project.

4.1.1 The resolution/wavelength limit

At first, it may seem intuitive that in order to increase the resolution of an imaging fibre it is necessary to make the cores smaller and closer together – effectively increasing the image's pixel density. In fact, as figure 4.1 shows, the closer together a pair of cores is the more the evanescent field of an excited core can couple energy to an otherwise un-excited mode of a neighbouring core [65,66]. This

blurs the resulting image, limiting the benefits of this design philosophy and necessitating a balance between the density of the cores and the rising crosstalk.

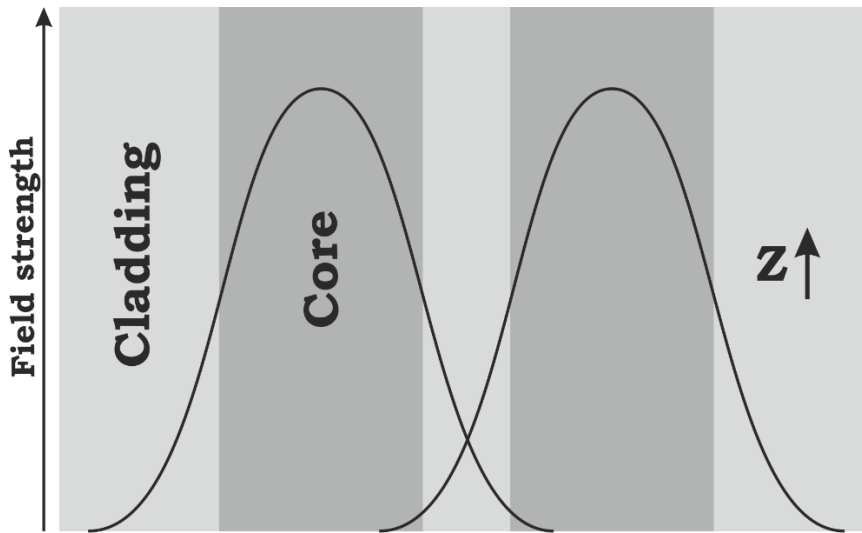


Figure 4.1: A pair of step index cores arranged so closely that the evanescent fields of their modes are overlapping.

Because modes' fields spread further at longer wavelengths, crosstalk also increases, effectively resulting in a long wavelength limit to their performance. Chen *et al.* explore this wavelength dependence using a commercial imaging fibre in their paper [66]. This limit depends strongly on how well the field is localised to the cores, and to understand it we revisit equation 12 from chapter 2,

$$V = \frac{2\pi}{\lambda} \cdot a \cdot NA, \quad (12)$$

showing the relationship between a core's V number, its radius, and its numerical aperture. A V number below 2.405 indicates that all higher order modes are cut off, and the fundamental mode is becoming less well confined within the core; the mode's evanescent field spreads further from the bounds of the doped region, and includes a greater proportion of the total energy [65]. From equation 12 we see that increasing the core diameter (fewer will fit in the imaging fibre) or raising the numerical aperture increases the V number. Higher V numbers better confine the modes, decreasing field overlap and reducing crosstalk.

Consequently, most imaging fibres have their cores and cladding doped to produce the maximum NA practically achievable. The reason for this maximum is the change in thermal expansion coefficient that results from doping the glass which causes stress to build up at the core-cladding interface. Additionally, the more heavily doped a preform is, the more expensive the glass costs to produce, both due to the raw material costs and the higher failure rate during heating and cooling, the results of which can be seen in figure 4.2.



Figure 4.2: A shattered stub from a highly germanium doped graded index preform with an NA of 0.3. A 250 mm length of the preform was being held in a vertical lathe and fused to a pure silica tube using a hydrogen torch. Stress between the differently doped glasses built up over the previous draws in the furnace and uneven heat from the torch caused it to shatter violently, leaving this stub in the chuck.

4.1.2 Non-identical core pairs

The examples of coupled cores discussed above are all pairs of identical cores. To explore what happens when this is not the case, we turn to “Optical Waveguide Theory” by AW Snyder and JD Love [65]. The book explores this problem in detail and provides an equation for the fraction of optical power coupled from an excited core (subscript 1) to its neighbour (subscript 2):

$$P_2 = F^2 \sin^2 \left(\frac{C_{\text{avg}} \cdot z}{F} \right), \quad (16)$$

where F is defined as

$$F = \frac{1}{\left[1 + \left(\frac{\beta_1 - \beta_2}{2C_{12}C_{21}} \right)^2 \right]^{1/2}}, \quad (17)$$

and C_{avg} is the average of the overlap integrals of the evanescent field of the mode in core 1 with core 2, C_{12} , and the field of core 2 with core 1, C_{21} . These are defined as

$$C_{12} = \frac{k \cdot NA^2}{2n_0} \int_{\text{core2}} \widehat{\varphi}_1 \widehat{\varphi}_2 dA, \quad (18)$$

where $\widehat{\varphi}$ is the mode field of each core.

Although one might expect an equilibrium to be reached when there is an equal amount of light in both cores, this is not the case. Instead, the sinusoidal nature of equation 16 indicates that

the power beats back and forth between the cores as the light propagates along their length, with a period of C_{avg}/F . This is because there is a $\pi/2$ phase difference in the light that is coupled across. It is also clear that any increase in the value of F^2 consequently increases the *maximum* power transferred to the neighbouring core. Equation 17 shows us that if the cores are identical $F=1$, meaning all of the power in one core will couple to the other over one beat length, but F decreases as the mismatch between the propagation constants of each core, β_1 and β_2 , is increased [67]. This means that regardless of how spatially overlapped the modes' fields are, if their propagation constants are different enough, then the detuning will keep the coupling interactions weak. Factors affecting the propagation constant of light in a core include the refractive index, core diameter, and which mode is propagating. As it is beneficial to have the highest refractive index step possible, and the number of modes is a bi-product of this and core size, the one remaining variable for controlling β is core diameter. During the course of her PhD, Kerriane Harrington has extensively studied the mathematics of how coupling between pairs of cores is affected by their doping profiles, and her calculations have informed our designs discussed later in this chapter.

4.1.3 Anderson localisation

In 1980, Abdullaev and Abdullaev published a paper in Radiophysics and Quantum Electronics [68] where they consider the implications of coupled mode theory in their model of an infinite close packed lattice of dielectric fibre waveguides, with randomised refractive indexes and diameters, that is invariant in the direction of propagation. Logically, the propagation constants of each core will also be random, decreasing coupling between cores as discussed in the section above. They draw a comparison to the mathematics of Anderson's model of electronic motion in a random lattice from 1958 [69] as it applies not just to quantum mechanics, but wave theory in general. Using this, they show that light in a single core of their random fibre lattice model is expected to remain localised to a group of cores around and including the original. This effect would come to be called Anderson Localisation and heavily influence the design of imaging fibres to the present day.

4.2 Prior work

This section provides a brief overview of the most well-established imaging fibres in industry.

4.2.1 Fujikura

A good example of the commercial state-of-the-art, Fujikura's FIGH-30-650S [70], shown in figure 4.3, is used widely in clinical endoscopic devices, including the version of Cellvizio used for bronchoscopy. This fibre is the standard against which many, including Proteus, compare their work.

Most of the technical and fabrication details of this fibre remain undisclosed by Fujikura, leading us to conduct our own investigations. Beginning with the structure, the cores are roughly $2\ \mu\text{m}$ in diameter, $3.2\ \mu\text{m}$ apart, and vary in size by around 10% [66]. They appear to be in a close packed hexagonal arrangement at short range, but there is also no long range order. This suggests that the fibre was simply stacked by randomly bundling different sized single core fibres and inserting them in a jacket tube – an incarnation of the model discussed in the above section on Anderson localisation. Although random stacking means there should be points at which the cores cross over one another in the stack, a large draw down ratio could be used so the short lengths of fibre (1-3 m) that are sold are effectively coherent along their length.

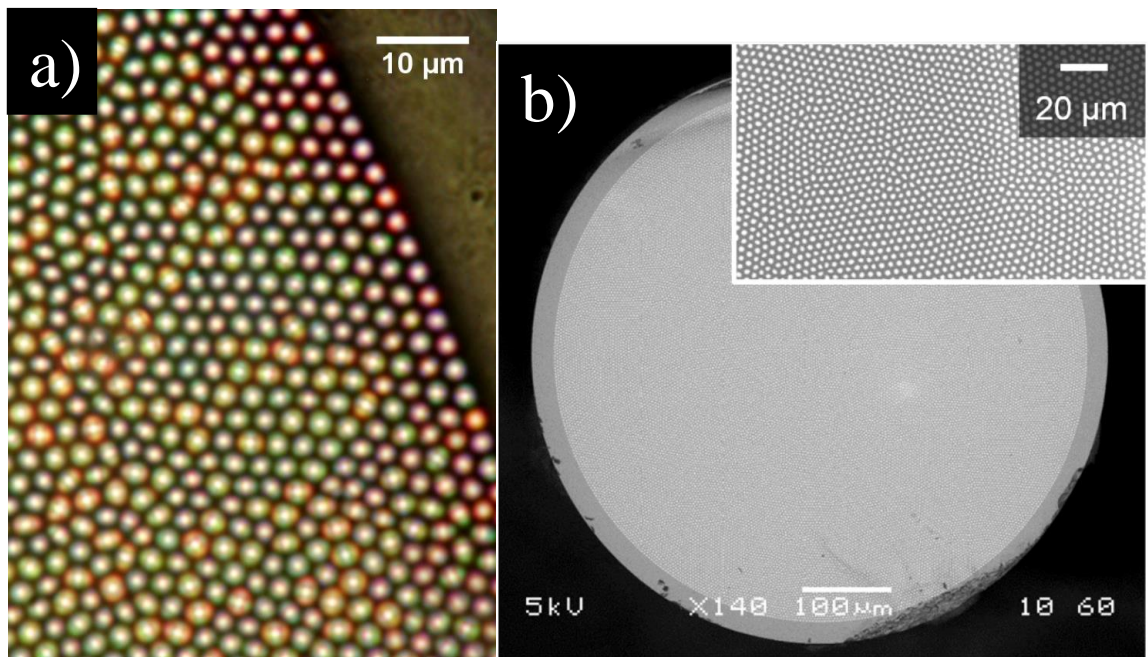


Figure 4.3: a) optical and b) scanning electron micrograph images of Fujikura’s FIGH-30-650S.

Reports in literature put the NA of the cores at a staggeringly high value of 0.39 [66]. Interest in how this had been achieved prompted Kerriane and I to use energy dispersive X-ray (EDX) spectroscopy with the SEM in Bath’s microscopy analysis suite (MAS). This technique uses the X-rays scattered from the microscope’s electron beam as it collides with atoms in the sample to provide a measure of the relative abundances of different atomic species, allowing us to investigate how much of each dopant is in the core and cladding glasses of this fibre. By comparing to a piece of preform with a known NA and doping profile, it was found that the reports of the fibre’s NA were accurate. It has been achieved using both germanium in the cores (raising the index) and fluorine in the cladding (reducing the index). This is beyond what can be obtained in Bath due to the resulting thermal stress that was discussed in section 4.1.1. It is possible that aluminium was also added to

the glass to help relieve stress in the structure, however, the SEM chamber and sample mount are both made of aluminium, making this hypothesis difficult to confirm or deny.

The challenges associated with reaching such a high NA are likely one of the core reasons why these fibres are so expensive. The stress due to the dopant also produces more dangling bonds in the structure which have been shown to fluoresce [71]. The emission peak is in the green part of the visible spectrum – coincident with the emission of fluorescent bacterial marker probes, and the autofluorescence of lung tissue. The fibre's fluorescence is strong enough to overwhelm many of the subtleties of the images, nullifying much of the benefit from decreasing core crosstalk. Probably because of this problem Fujikura provide two types of the FIGH-30-650S, one designed for the lab with the highest possible NA, and another for the clinic with smaller cores, less dopant, and consequently increased coupling.

4.2.3 Leached fibre bundles

The cores of these fibres are usually fabricated from a single core preform with the addition of an external layer of soluble cladding material. These are stacked in a jacket tube that is also soluble, and drawn to make an imaging fibre. The fibre is submerged in an acid solution or strong solvent, apart from a small length at either end, to dissolve away the cladding material joining each core to its neighbours, resulting in them being physically and optically isolated from one another.



Figure 4.4: A soft chalcogenide glass fibre bundle fresh from having its polymer cladding leached away in a solvent bath. It is shown here partially submerged in water [72].

Figure 4.4 shows the result of this; an imaging fibre with separate core strands for the majority of its length, with identically arranged high resolution fused sections at either end. This reduces

coupling between the cores and drastically increases flexibility at the expense of durability as the core fibres on their own are fine and weak, usually meriting an additional external polymer coating, as with the instrument in figure 4.5. Even with this added protection, these fibres usually have a limited lifetime before the individual cores begin to fracture within.



Figure 4.5: An endoscope including a commercial leached fibre bundle fabricated by Schott [73].

Surface imperfections on the fine core fibres can lead to scattering of the light they guide, and therefore high loss. This means this imaging fibre design is mainly used for purposes requiring only short lengths with high flexibility.

4.2.4 Phased array imaging

A spatial light modulator can be used to control the phase of coherent light being coupled into each core of the proximal end of a multicore fibre. This allows the phase of the light emerging from the distal fibre end to be controlled. By interfering the individual cones of light from each core a high intensity spot can be formed, and made to scan across a sample. The returning scattered or fluorescent light from the spot is guided back through some combination of the fibre's cores, and its intensity is recorded. Knowing this intensity and the corresponding position of the scanning spot allows images to be built up, at resolutions that are not limited by the core size or spacing [74]. Instead, the scanning spot size is theoretically limited by the wavelength of the light used, and practically, by the quality of the fibre's cores, to a few micrometres in the case of early examples [74]. This concept also enables the delivery of pulses of light that are too low power to undergo significant nonlinear processes in the fibre itself, but nonlinear microscopy can be achieved using the high intensity interference spot.

The major challenge with phased array imaging lies in knowing the phase delay of each core. This is why the fibres used for these projects have usually been designed to have identical cores, which means that they must be kept widely separated to avoid coupling. Additionally, even slight

bends in the fibre will increase the path length of the cores on the outside relative to the inside, causing the light to reach the distal end out of phase.

As part of his PhD, James Roper of the University of Bath CPPM produced the fibre in figure 4.6. By spinning the preform during the fibre draw, the cores were made to be helical about the fibre axis so that they spend equal time on the inside and outside of bends in the fibre. The resulting phase delays of the outer cores (their helical path is longer) relative to the central ones was compensated by stacking successively smaller cores each layer away from the centre to decrease their delay [75].

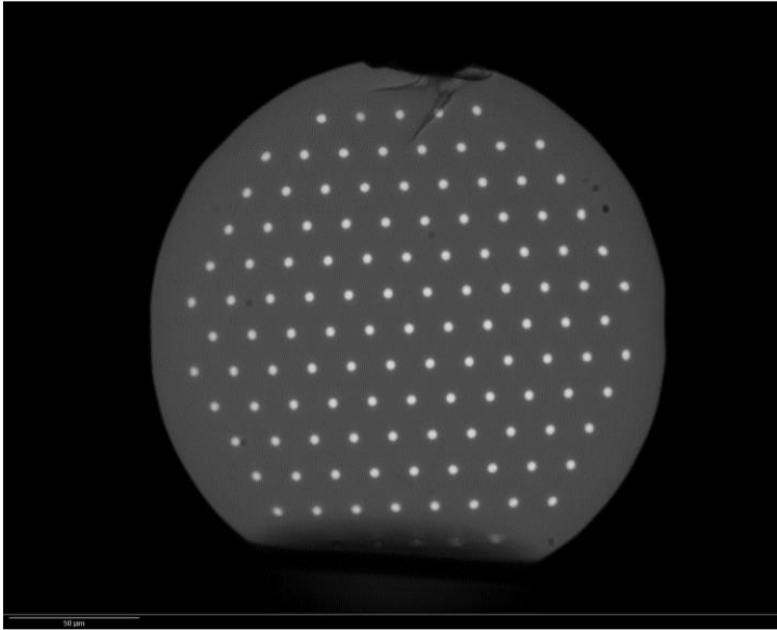


Figure 4.6: An optical microscope image of James Roper's 200 μm OD helical phased array imaging fibre, illuminated from beneath [75].

Regular core lattices also present a problem as, when scanning the central spot, higher order fringes can impinge upon the imaged object and contribute false signal, limiting the effective scan area. This can be avoided by using a fibre with randomly arranged cores, as was done with Dr. Fernando Fevero's fibre, featured in [76], and a similar fibre fabricated by physicists in the Fresnel Institute of Marseille [77].

For a phased array imaging fibre to be as effective for medical endoscopy as commercial imaging fibres are, it would need to marry both the concepts I have discussed. This means fabricating a helical fibre with randomly arranged cores, all of which have their phase delay matched. Each part of this was a great feat of science and engineering on its own, so it was decided that incorporating this technology into Proteus' endoscope devices would be too challenging at this early stage.

4.2.5 Multi-stacking techniques

Aiming to produce an imaging fibre of superior quality to Fujikura's FIGH-30-650S for the Panoptes bronchoscope system, Dr. Jim Stone and other researchers began by investigating flaws in the commercial fibre's design. A random arrangement of a continuous range of core sizes has two problems: Cores of similar sizes can end up side by side, coupling strongly together, and intermediate core sizes can provide pathways for light to couple between even the most dissimilar cores. Consequently, the fibres developed for the Proteus project all involve a regularly arranged lattice of a minimal number different of core sizes to guarantee no similar cores end up as nearest neighbours. figure 4.7 shows this type of design in the case of a hexagonal stack. As these stacks are drawn down without an outer jacket the canes they produce are also hexagonal. Therefore, when thickness of these structures is discussed in this thesis, I refer to the distance from one flat face to its diametrically opposite side.

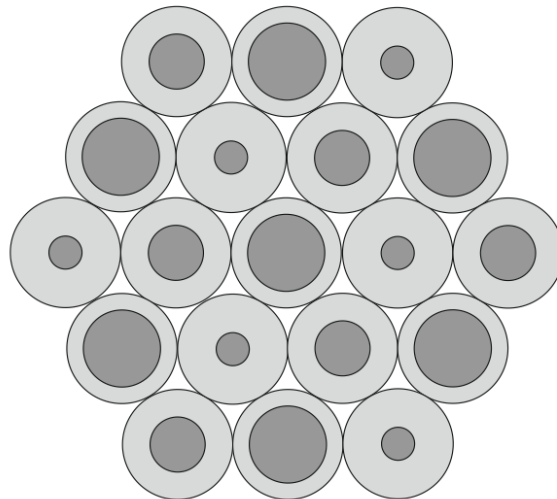
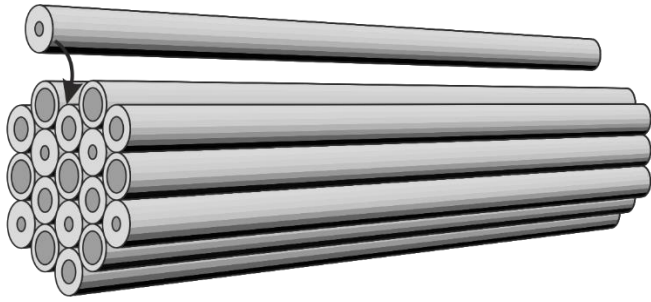


Figure 4.7: An example hexagonal stack with cores of 3 different sizes arranged to minimise coupling.

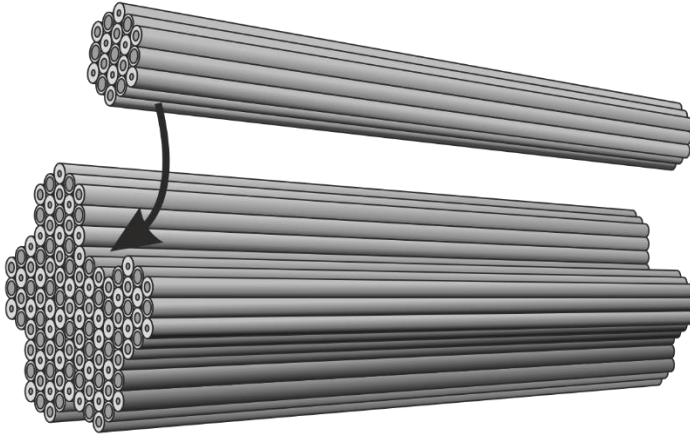
This design paradigm has seen extensive use in the optical fibres developed for the telecoms industry, where it is often referred to as space division multiplexing [78]. Regularly stacking the thousands of cores necessary for imaging in this way would be impractical. Instead, we employ multiple unjacketed stack-and-draw stages to increase number of cores in the canes multiplicatively instead of additively, as shown in figure 4.8.

Chapter 4: Imaging fibres



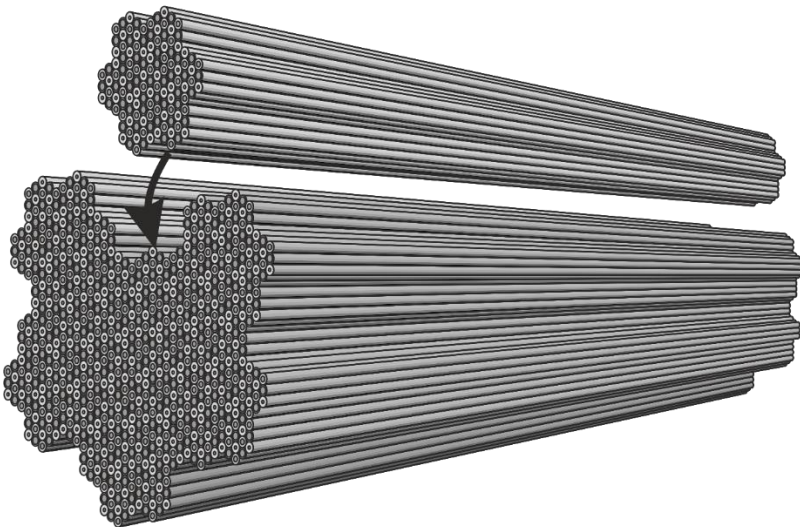
Assemble a primary stack of core canes.

Draw down to form primary canes.

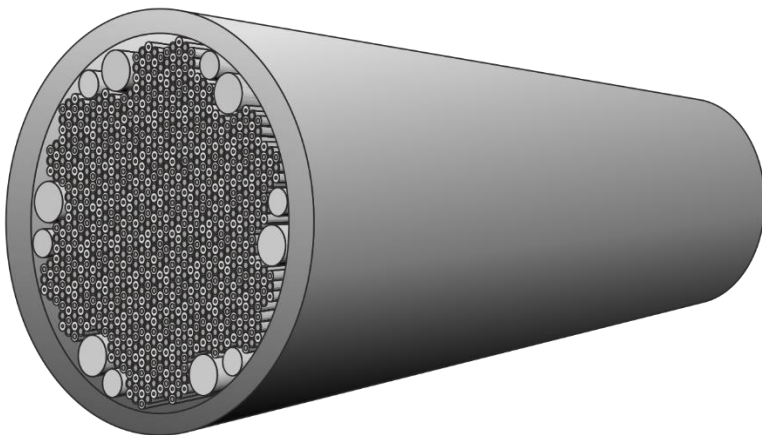


Assemble a secondary stack of primary canes.

Draw down to form secondary canes.



Assemble a tertiary stack of secondary canes.



Slide tertiary stack into jacket tube and pack edge spaces.

Draw down to preform canes or fibre.

Vacuum can be applied to the end to collapse interstitial spaces

Figure 4.8: An illustration of the multi-stacking process.

Dr. Jim Stone fabricated the first of the Proteus project's imaging fibres, shown in figure 4.9, using this multi-stacking technique. The sole intent of this early prototype was to investigate the practicality of multi-stacking, so for the sake of efficiency (both in terms of resources and time) considerations of crosstalk were set aside and only one graded index doped preform was used for the cores. This resulted in all the cores of the final fibre being the same size, and crosstalk heavily limiting the imaging capabilities of the fibre. Nonetheless, an imaging fibre of over 5000 cores had been fabricated with relative ease; an adequate demonstration of the potential of these techniques.

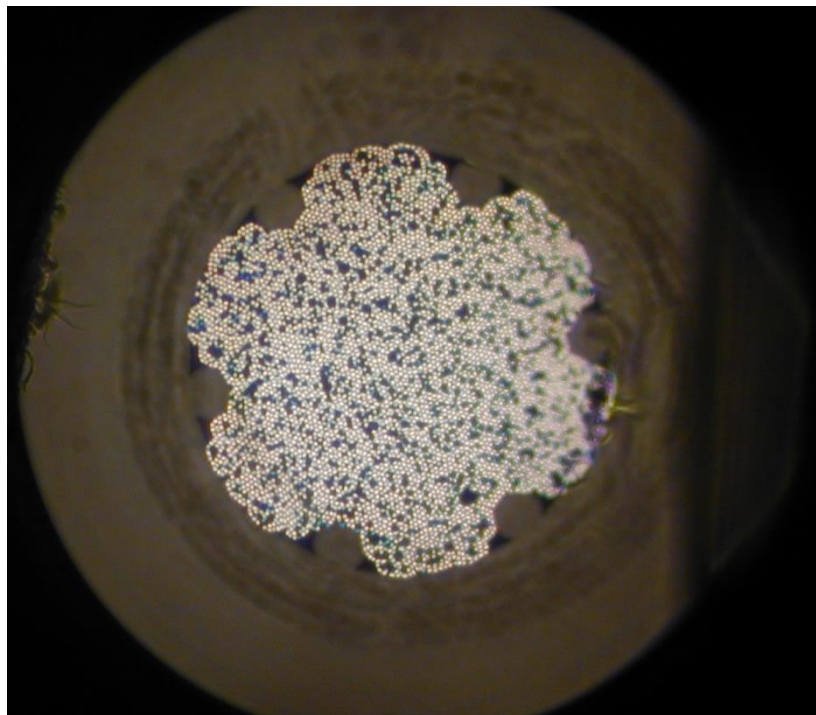


Figure 4.9: An optical image of the cleaved end of the first prototype hexagonally stacked imaging fibre, illuminated in transmission by a white light bulb, courtesy of Dr. Jim Stone.

4.3 Panoptes imaging fibres

In this section I discuss the designs for some of the imaging fibre prototypes produced for the Panoptes probe, the nuances of their fabrication techniques, and give a qualitative appraisal of their performance. Many prototype imaging fibres were fabricated during this iterative design process that would eventually produce the final, medical-grade product. I have chosen to discuss this small selection for two reasons: Firstly, these versions were among those in which I personally played a critical role in every stage, from conception to characterisation. Secondly, this is a subset of those versions that, with hindsight, can be identified as the most significant stages of this work, both due to design choices and maturation of the fabrication techniques. For brevity, OD refers to the outer

diameter of silica rods or tubes, and ID to inner diameter of the tube or the doped core region of a rod.

To begin the design process it was important to revisit Proteus' goals with respect to the imaging fibre, which were outlined in chapter 1. It was required to match or improve upon the following characteristics compared to the leading commercial fibre, Fujikura's FIGH-30-650S: Resolution, operational wavelength range, outer diameter, minimum bend radius, background fluorescence, and cost. With respect to the final point, cost, achieving these goals using the standard, mass produced, doped preforms used in the telecommunications industry would reduce the imaging fibre's price per meter to the point where the devices could be disposable after a single use. Without the need to sterilise the systems between uses, clinical workflow would also be improved. This prospect was so appealing to the clinicians that it eventually became the main focus of the Panoptes imaging fibre's design.

4.3.1 50,000-core fibre

The first imaging fibre made during this PhD was also one of the most ambitious in terms of scale, allowing me and Kerriane Harrington to practice our stack-and-draw techniques. Originally designed to have hexagonal stacking stages of 61, 37, and finally 19, producing 42,883 cores, the fibre was never intended to be part of a bronchoscope system as it would likely need to be drawn to too large a diameter to function at wavelengths longer than 500 nm. Instead the purpose was to refine the techniques Dr. Jim Stone had employed in fabricating his earlier multi-stacked fibre, test the scalability of the fabrication techniques, and the effects of crosstalk on the image quality of this type of fibre.

4.3.1.1 Fabrication

Beginning with a simple graded index preform with a parabolic doping profile (ID/OD 16.8/23 mm and 0.22 NA) the 3 different core size canes were made by drawing down to 21 canes of 2 mm and 4 canes of 6 mm OD, cleaved to 1 m lengths. The 6 mm rods were then jacketed in 6/10 mm and 6/7.5 mm ID/OD pure silica tubes respectively, all of which were drawn down to 2.5 mm canes using vacuum to collapse any gap between the cane and the tube. This produced 40 canes, all of 2.5 mm OD to allow hexagonal stacking, 20 of which had 1.5 mm ID and 20 of 2 mm ID. All 61 of the 2.5 mm canes were then stacked on the hexagonal jig in a close packed structure, arranged so that no two neighbouring canes had the same core size, as shown in figure 4.10 (a).

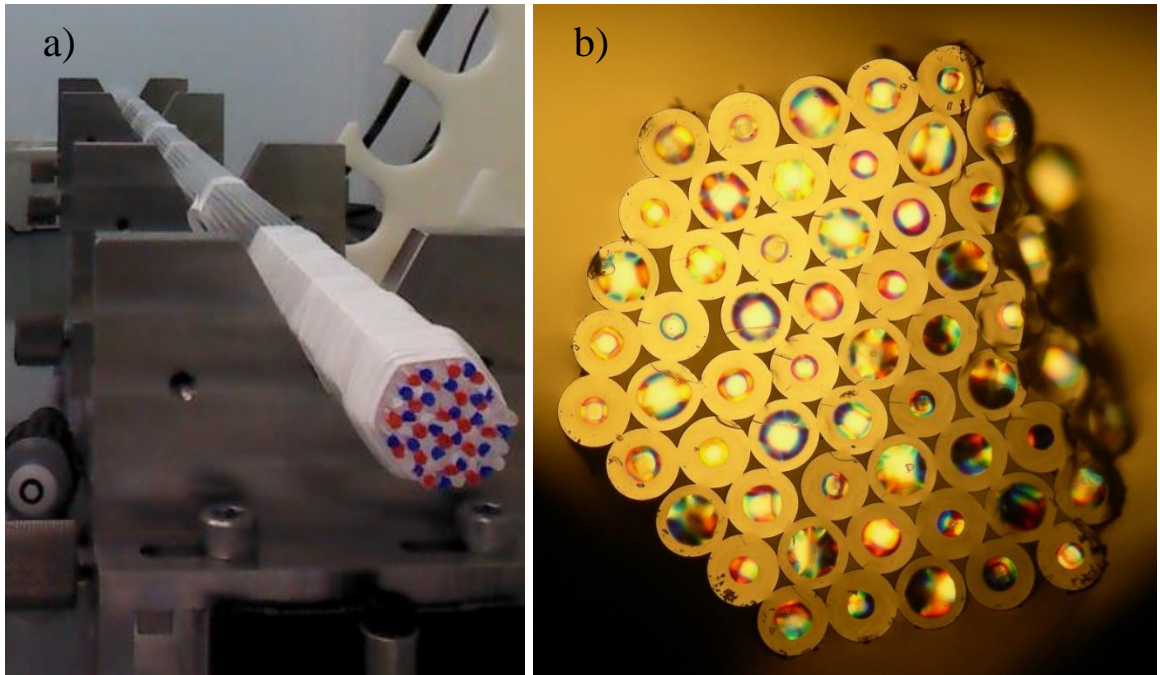


Figure 4.10: (a) an image of the stack of 61 canes. The ends of the smallest core canes are marked red, medium in blue and the largest are left colourless. The PTFE binding for clamping in the tower chuck can be seen at the close end, along with smaller strips at intervals along the stack's length. (b) an optical microscope image of the resulting 2.5 mm hexagonal cane, ready for the second stacking stage.

The stack was held together without a jacketing tube by using several strips of polytetrafluoroethylene (PTFE) tape wrapped at roughly 20 mm intervals along the length, and a large amount of tape to safely secure the stack in the cane drawing tower's chuck, as seen on the near end of the stack in figure 4.10 (a). The stack was arranged so that the canes produced naturally presented parallel flat faces to the pulling belts. If the cane is not aligned in this way the belts will forcibly twist it into alignment when clamped, producing a twist in the glass in the furnace. This twist is followed by the belts, resulting in helical canes. Even slightly twisted canes make subsequent stacking stages nearly impossible.

The PTFE strips were removed one by one during the drawing process as they approached the furnace. Because the stack is unsupported within the furnace, the drop-off can have unfused canes or groups of canes that have become separated. By feeding the glass at half the intended speed while bringing the drop-off down past the cane pulling belts, the canes within the furnace touched and fused together into a solid hexagon. Great care was taken that the drop-off remained straight until the cane was clamped in the pulling belts to avoid twists. 37 well fused hexagonal canes of 2.5 mm were produced, shown in figure 4.10 (b).

Next the 37 hexagonal canes were stacked, bound, and drawn down similarly to the stack of 61, producing the canes in figure 4.11. Unfortunately, instead of the intended 3.7 mm these canes were drawn to only 3.2 mm thick as the laser mic was measuring the corner to corner size instead of

the flat-to-flat thickness. The design was amended to have 24 smaller canes in the final stack, producing a fibre with a roughly oval field of view with 54,168 cores.

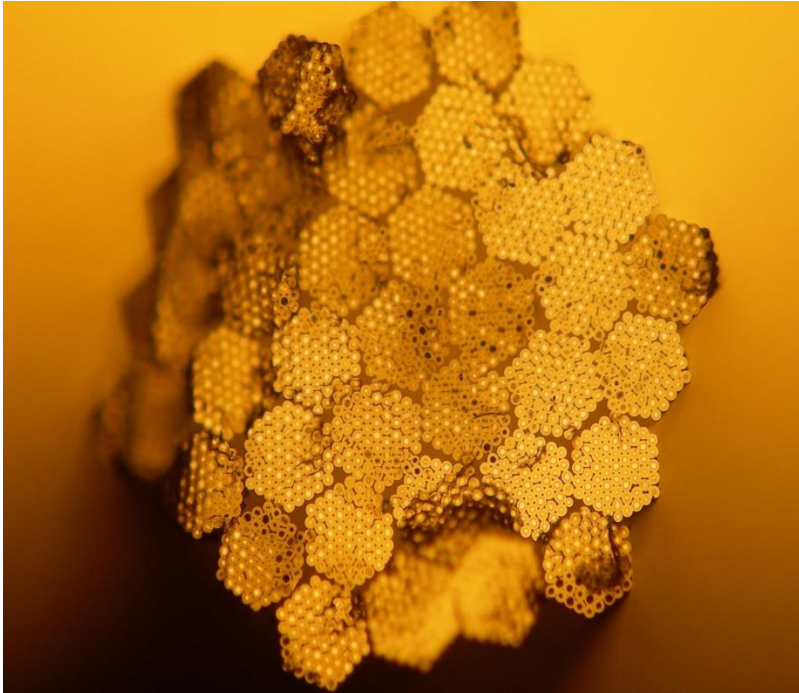


Figure 4.11: A transmission optical microscope image of a cane drawn from the secondary, 37×61 core stack.

For the final stage the 24 canes were stacked and inserted into a 21/25 mm ID/OD jacket tube. The surrounding gaps were packed out using pure silica packing canes of various diameters, and the tube sealed using the furnace to fuse the glass at the bottom and by PTFE tape and a brass piece at the top. This preform was then drawn to several fibres of various diameters while a vacuum was applied via the brass chuck to collapse any interstitial gaps. The fibre in figure 4.12 (a) & (b) was produced from this stack. It has an OD of $760 \mu\text{m}$, an imaging circle of roughly $660 \mu\text{m}$, and core diameters 0.9, 1.2, and $1.6 \mu\text{m}$, with a centre-to-centre spacing of $2.4 \mu\text{m}$. From here on I will refer to it as the 50,000-core fibre.

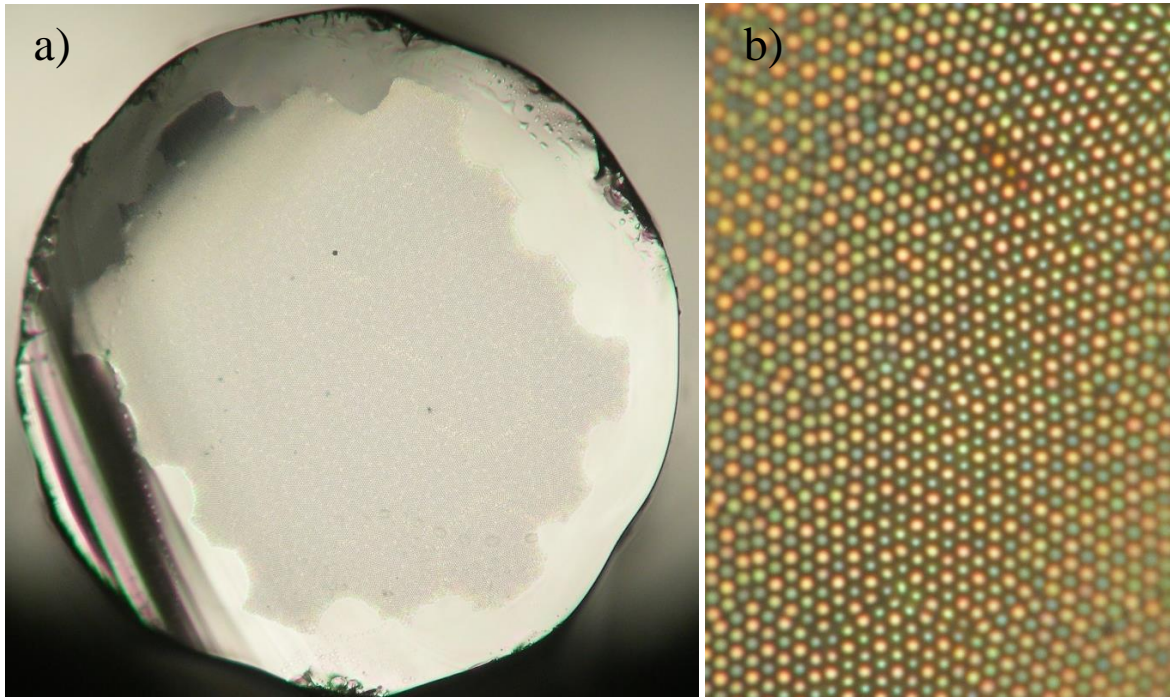


Figure 4.12: Optical images of a stub of 760 μm 50,000-core fibre, (a) at 20 \times , (b) 100 \times . The core sizes are 0.9, 1.2, and 1.6 μm , with a spacing of 2.4 μm .

The different colours of each of the 3 core sizes, figure 4.12 (b), are because the smaller cores guide the longer wavelengths less effectively. This therefore also resulted in the smaller cores appearing dimmer in grayscale images.

4.3.1.2 Imaging characterisation

The characterisation of the quality of the prototype fibre began with simple observations of the quality of images of cells obtained via a ~ 50 cm length of the 50,000-core fibre. The cells chosen were from an onion membrane due to their transparency and convenient feature size; 20 μm average thickness, 100 μm length, 5 μm thick walls and 10 μm diameter nuclei. The cells were placed on a slide, stained with iodine and moved to zero working distance against the cleaved distal fibre end face using a 3 axis stage. A supercontinuum fibre white light source was used to illuminate the sample from behind. The light was coupled out of the proximal end of the imaging fibre and onto a monochrome CCD camera using an aspheric lens. Note that to properly couple light out of an imaging fibre and obtain an accurate image of the near-field, it is necessary to use a lens of equal or greater NA than that of the fibre's cores. Failure to do so risks blurring fine details, especially those of the higher order modes in the cores. Figure 4.13 shows an image of the onion cells using the 50,000-core fibre and 450 nm light.

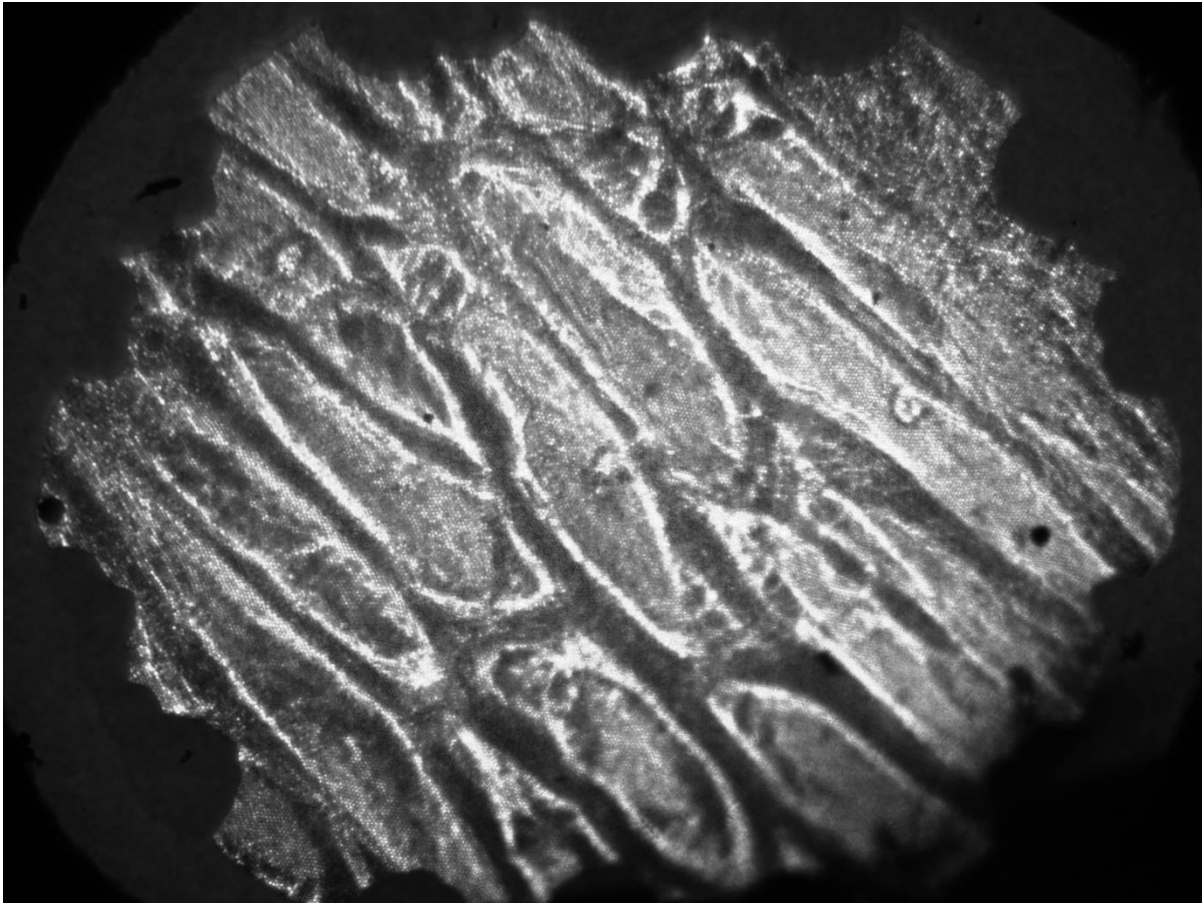


Figure 4.13: An image of onion skin cells through a ~50 cm length of 760 μm OD 50,000-core fibre using a monochrome camera and supercontinuum filtered to 450 nm.

At wavelengths shorter than 500 nm the images were startlingly good; however, a great deal of coupling was observed at wavelengths longer than 600 nm, degrading the images beyond recognition. To better characterise this fibre's performance across the whole visible spectrum we drew the remaining preform down to 1 mm diameter canes to be used in further experiments. Scaling up the structure in this way increases the sizes and separations of the cores, and therefore shifts the fibre's performance profile to a correspondingly longer wavelength.

4.3.1.3 Coupling characterisation

The early imaging experiments, although successful at demonstrating imaging, provided only qualitative evidence of image quality and coupling characteristics of the fibre. For this reason, I proceeded to couple a supercontinuum light source into individual cores of the middle size and observe the relative output power from the surrounding cores due to crosstalk. The resulting near field images, band pass filtered to three visible wavelengths, are in figure 4.14. The increase in crosstalk with longer wavelengths is immediately apparent, with fields of cores of the medium size family coupling together in the 600 nm image of figure 4.14. The fact that only one size family

couples together in each of these images is good evidence that nearest neighbour coupling has indeed been suppressed. We had initially assumed that, because of the distortions of the core shapes that arise when the interstitial spaces are collapsed during fabrication, that next-nearest neighbour coupling would be negligible. Clearly this was not the case when compared to nearest neighbour coupling, despite the fact that little thought was put into the core diameter ratios, as it was only a trial of the fabrication techniques. In an effort to quantify the extent of the next-nearest neighbour coupling, I produced intensity profile scans such as those in figure 4.15.

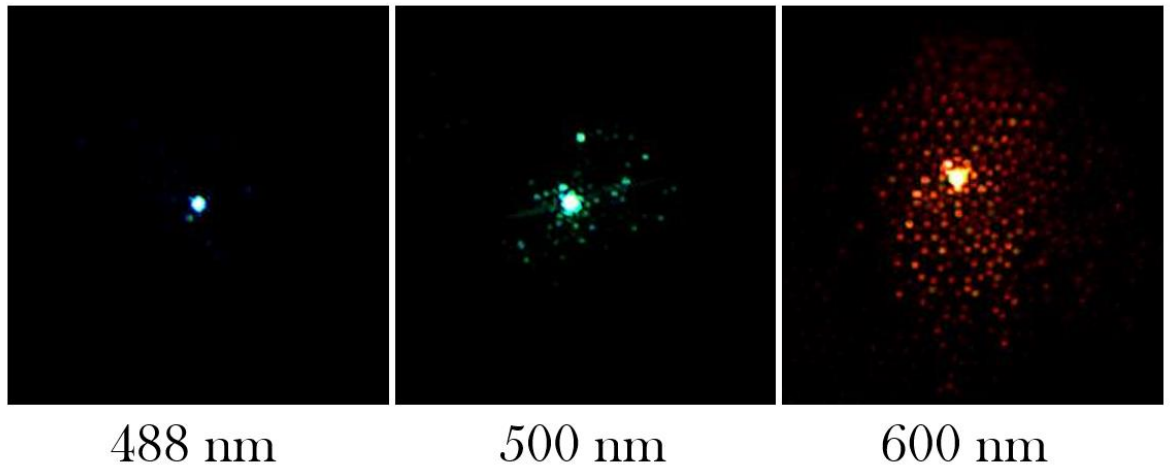


Figure 4.14: Images of the proximal end of the 760 μm OD 50,000-core fibre when coupling a supercontinuum source into a single, medium sized core from the distal end. The light was filtered to 3 different wavelengths as indicated below each image, and the coupling observed using a colour camera.

Using a 550 nm filter and a monochrome camera the traces in figure 4.15 (d) were produced by plotting the intensity along each of the line profiles indicated in the nearfield images (a to c) when coupling into first one of the big cores, then a small one, and finally one of Fujikura’s cores for comparison. As expected, next-nearest neighbour coupling dominates in the 50,000-core fibre, with the smaller core coupling more than 40% of its power to the other core compared to less than 15% with the large core. This made it clear that the smallest core was too small, and that the core sizes of future fibres could afford to be more similar as next-nearest neighbour coupling was so dominant. Due to Fujikura’s randomly arranged structure, nearest neighbours naturally dictate the coupling characteristics, with approximately 27% of the power coupling to the chosen neighbour core.

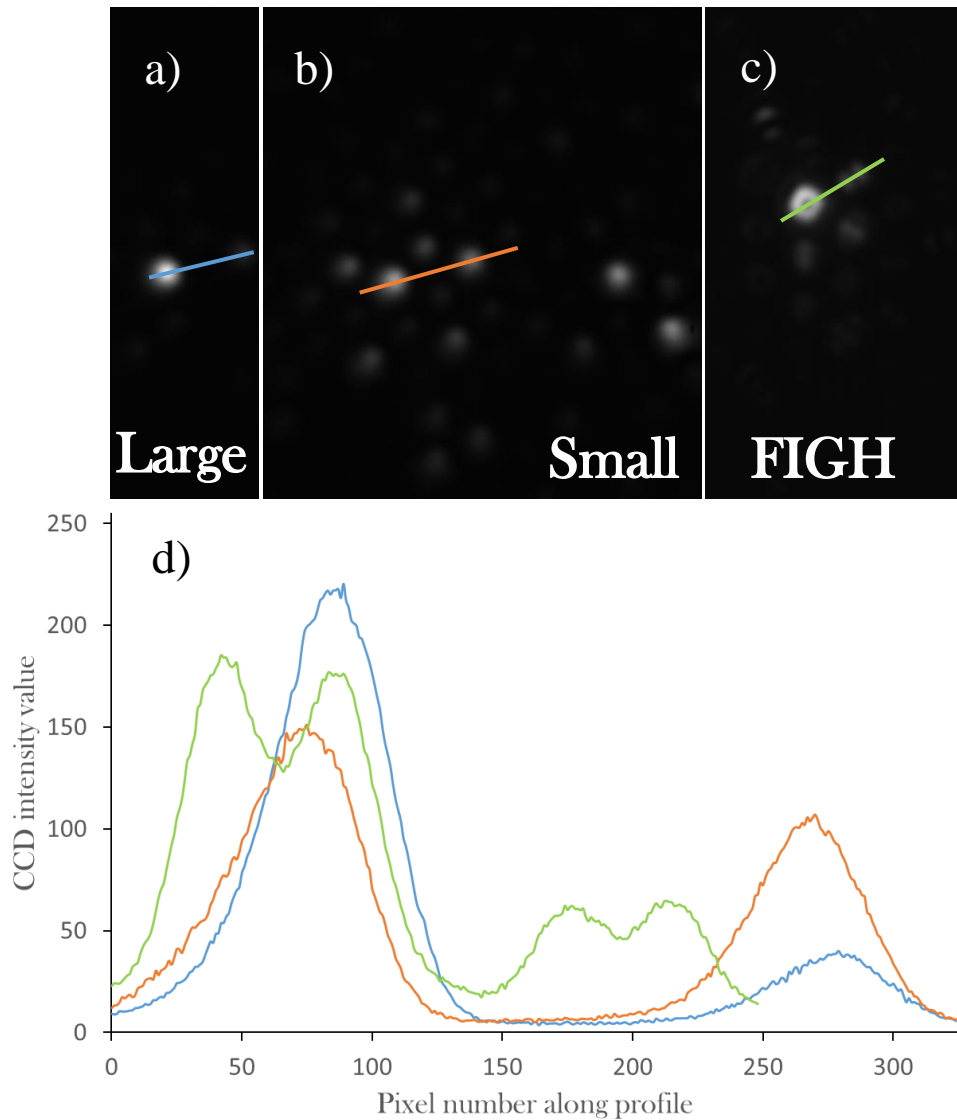


Figure 4.15: a) b) c) three near field images of the proximal end of the 50,000-core fibre (a & b) and the FIGH-30-650S (c). A single large core was excited for (a), a small one for (b), and a randomly selected FIGH core for (c). The excitation source was a supercontinuum filtered to 550 nm. d) The line profiles on each image indicate the intensity profiles used to produce the traces to the bottom of the figure. In each case, the trace begins to the left of the intentionally excited core and runs over the brightest cross-coupled core in the image.

4.3.2 The step index Panoptes imaging fibre – PSI1

Believing that the hard boundary of a step index profile would better contain the mode fields, Dr. Jim Stone, Kerriane Harrington, and I began work on the first Panoptes prototype. The smallest core size was set by the need to guide light at 520 nm, and the largest by the requirement of single mode performance. This second constraint arose because the evanescent fields of higher order modes are more spatially expansive. It can therefore be inferred that they couple together more, and so were to be avoided. The corresponding middle core size for minimal inter-core coupling, found using

Kerriane's coupling calculations, should be slightly larger than half way between the other two. This is because, as discussed in chapter 2, the smallest core allows its fundamental mode field to spread the furthest, requiring a slightly larger mismatch in propagation constant to achieve the same F^2 (equations 12 & 17) with the middle core compared to that between the middle and large cores. Simulations of pairs of these cores showed that they would couple together less strongly at 500 nm than was observed experimentally with the FIGH-30-650S in the previous section.

4.3.2.1 Fabrication

Three step-index preforms of NA 0.22 and core/cladding ratios 0.35, 0.42, and 0.48, all with the same outer diameter of 25 mm were commissioned from the Draka Prysmian group. These were drawn in a multi stage stack and draw fabrication procedure similar to the one used to make the 50,000-core fibre. This time 61 canes were used in the first stage, 19 in the second, and 7 in the final stack packed within the jacket tube. The fibre fabricated from this preform is shown in figure 4.16, with 8113 cores of radii 1.30, 1.54, and 1.78 μm , roughly 3.5 μm spacing, and an outer diameter of 310 μm . This meant that the largest core was just below the second mode cut-off at 520 nm.

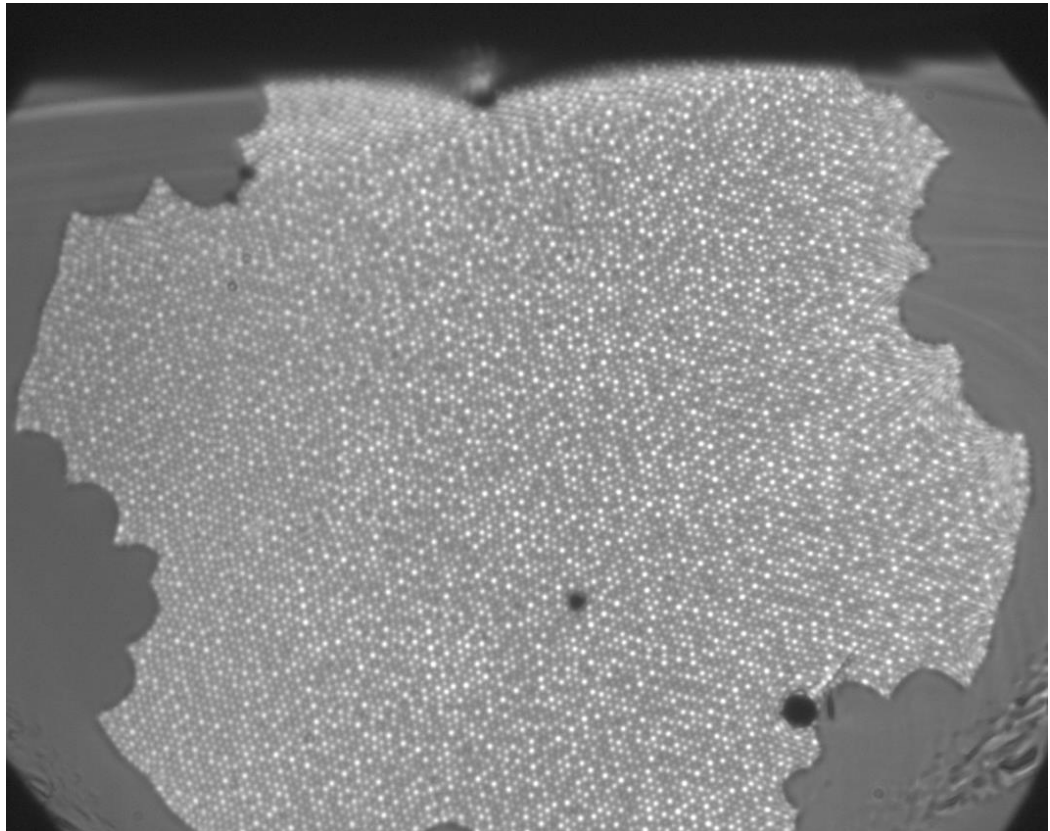


Figure 4.16: The step index prototype imaging fibre for Panoptes – PSII. Two small air bubbles are present at this end face, one near the centre, the other at the edge of the imaging area.

4.3.2.2 Characterisation

Several imaging standards were used to attempt to characterise this fibre. Coupling was so much worse than with the FIGH-30-650S and the 50,000 core fibre that no features in any of the images could be discerned. This was primarily due to the NA being almost half that of the FIGH-30-650S (0.22 compared to 0.39). In retrospect, it was naïve of us to assume that simulating pairs of cores would be a true indication of how they behave in a comparatively infinite core lattice, as is their situation in imaging fibres.

4.3.3 Panoptes graded-index imaging fibre – PGI1

By using a graded index preform with a parabolic doping profile, the stresses in the glass are spread over a larger volume, making it easier to dope the core to a higher peak index without fracturing during heating. Figure 4.17 compares the index profiles of two commercial preforms that have been doped with germanium to the full extent that the internal stress allows. Kerriane Harrington's simulations showed that the advantage this higher peak index contrast provides outweighs any shortcomings resulting from the more gradual index change.

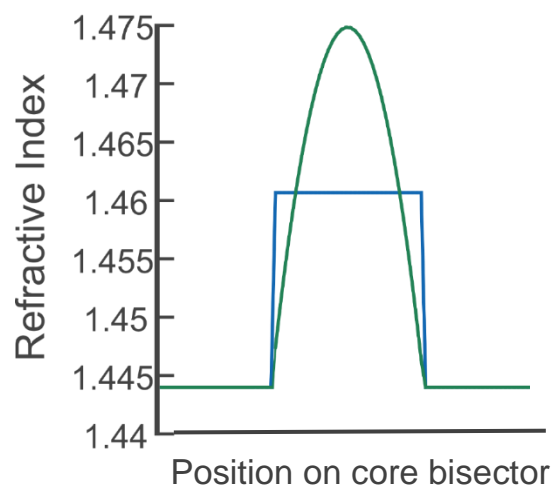


Figure 4.17: A comparison of the typical index profiles of maximally doped graded (green) and step (blue) index cores, courtesy of Kerriane Harrington.

Draka Prysmian fabricate preforms with a parabolic index profile, peak NA of 0.3, core/cladding ratio 0.75, and OD of 32 mm - just small enough to fit in the bore of our cane drawing furnace. These preforms are also low cost as they are commonly used in the telecoms industry, meaning orders often come straight off the shelf with a comparatively short lead time of only a few weeks. Although this is a small consideration for a research project, to the medical industry this is a huge advantage as low cost imaging fibre could mean disposable probes.

4.3.3.1 Fabrication

I began by drawing a graded index preform to 2 and 5 mm canes, jacketing the 5 mm canes in 5/6.4 mm or 5/5.87 mm ID/OD tubes, and drawing these down to 2 mm also. Note that with the thinner jackets if the furnace temperature is too high the jacket collapses to form bubbles before the vacuum can remove the air. 61 canes of 2 mm OD were stacked and drawn down, similar to the first stage of the 50,000-core fibre. The second stage consisted of 19 of these canes, and the final stage of 19 of those, producing a 22,021 core fibre, shown in figure 4.18. It is clear from this image that the furnace temperatures used were too high, trapping bubbles within the structure that have subsequently expanded. Another possible explanation is that there were dust particles and impurities that were trapped within the stack and then vaporised, forming pockets of gas.

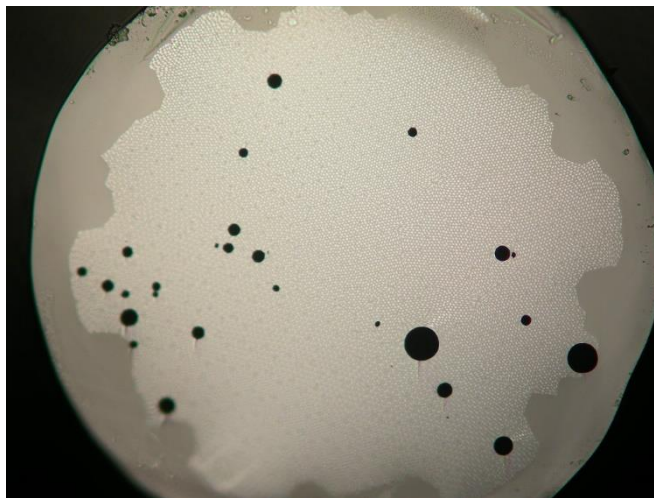


Figure 4.18: An image of the end of a 700 µm diameter Panoptes graded index imaging fibre – PGI1. The bubbles in the structure are due to drawing with too high a furnace temperature causing some of the tiny interstitial spaces to seal before being evacuated, and then expand. It could also possibly be due to the vaporisation of some internal impurities.

4.3.3.2 Characterisation

A more repeatable image standard than cells was required, and so USAF test targets of the 1951 variety depicted in figure 2.14, chapter 2, were purchased and used from this point on. We have mostly used the negative versions of these targets, as the wide dark regions surrounding the transmissive lines allow the full extent of any long-range coupling to be observed.

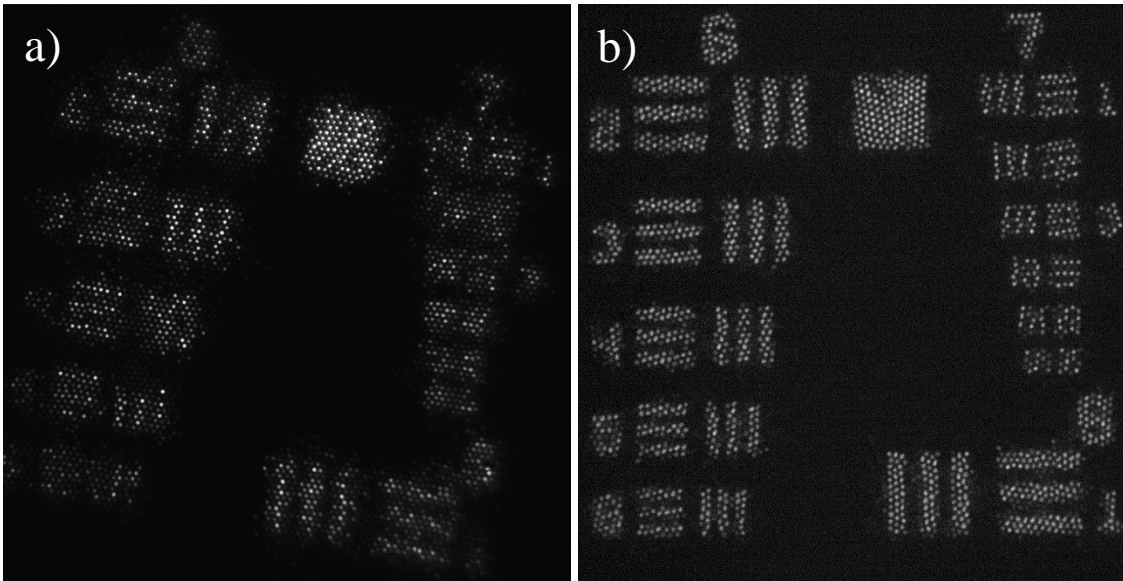


Figure 4.19: Negative USAF test target images taken using 600 nm light and the Panoptes graded index imaging fibre (a), and FIGH-30-650S (b) for comparison.

Images of a USAF resolution test target are shown in figure 4.19, through PGI1 (a) and the FIGH-30-650S for comparison (b). Although the non-uniform imaging circle, air holes, and lattice imperfections make the quality patchy at best, where the structure is good the images are of high enough quality to identify the different test target groups, but still a far cry from the performance of the FIGH-30-650S.

4.3.4 Panoptes graded-index – PGI9

Between myself, Kerriane Harrington, and Dr. Jim Stone, 8 more graded-index Panoptes imaging fibre prototypes were made using the techniques discussed so far. Limited coupling simulations were carried out to guide the work, but the complexity of simulating a real structure with tens of thousands of cores was beyond what we were capable of, leading us to an iterative and experimental design process. Some fibres failed to achieve better results in the characterisation stage than the first Panoptes graded-index fibre due to structural imperfections, and several simply failed during their fabrication due to technical difficulties with the tower, and particularly the coating material. Many of the issues with imaging using the earlier fibres were due to the expansion of sealed bubbles in the structure or the collapse of large gaps between the canes distorting the cores. Additionally, cores at the edges of stacks that ended up next to an identical core in a neighbouring stack would couple strongly. Sometimes this produced entire rows of strongly coupled cores along the boundaries of the stacks, and it is extremely challenging to stack accurately enough to avoid it entirely. One of the more significant causes of these problems are the lattice dislocations that would frequently arise between the canes stacked in the second and third stages because of the bumps on the primary stack canes (from the original single core canes) making it difficult to mesh them together correctly.

Because of this, I decided to fabricate Panoptes graded index 9 (PGI9) with only two stacking stages. The 331 elements in the first stack results in a smoother edged set of canes that fit together better, both with each other, and with the packers inside the jacket tube.

This fibre has featured in two papers our group has published; one of which was written by me [79], and the other by Dr. Jim Stone [64], with sections of text and figures describing this imaging fibre and its fabrication contributed by me.

4.3.4.1 Fabrication

The core canes were fabricated as with the first Panoptes graded index fibre, with the exception that I drew them to 1 mm diameter so a stack of 331 would fit on the jig. This stack was drawn down a thickness of 2.1 mm as in figure 4.20. 37 of these canes were restacked, and packed into a jacket tube. Drawing this directly to 525 μm fibre produced the cross section in figure 4.21. These images show that the strategy of using only two stacking stages helped produce a fibre with very few imperfections. The structure is so uniform that it is difficult to see the borders between stacks, but they can be found by looking for neighbouring cores of similar size.

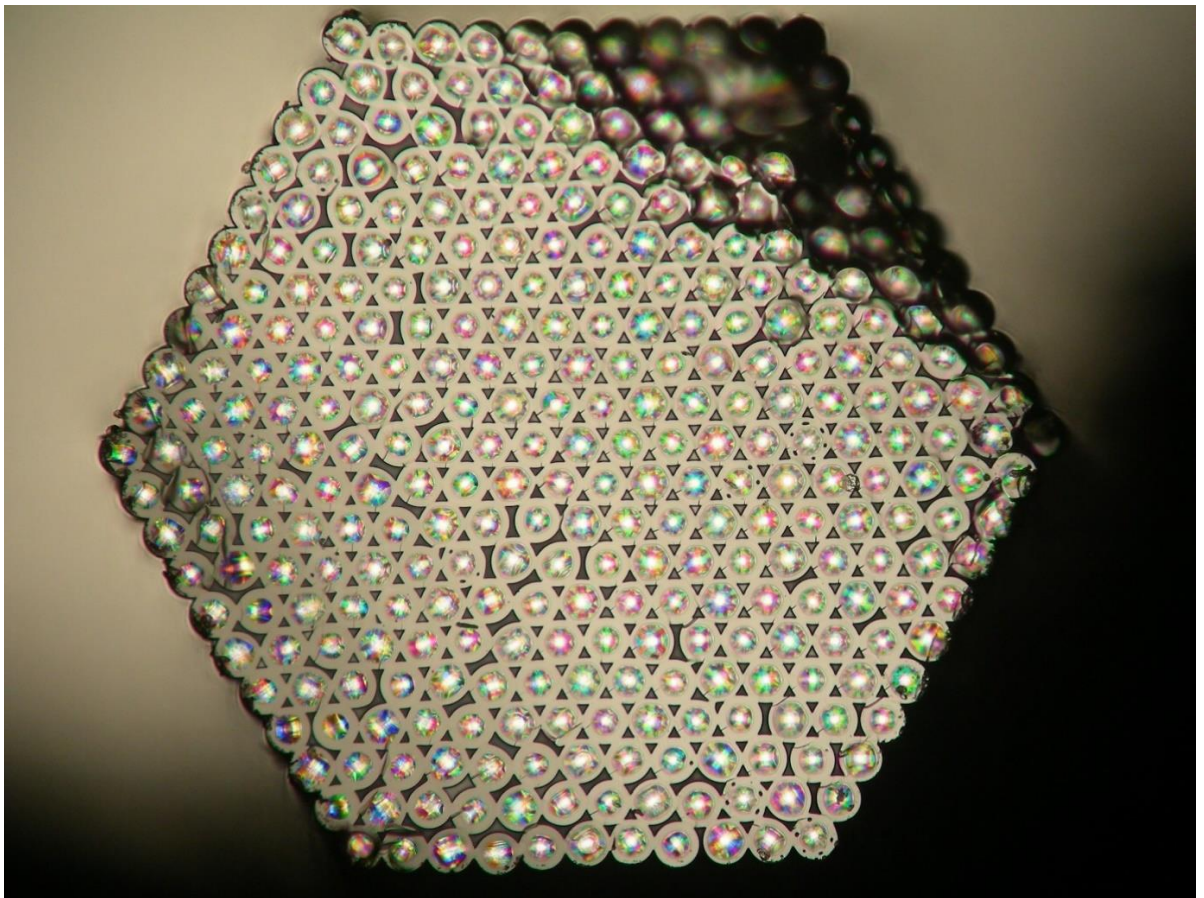


Figure 4.20: A 2.1 mm thick 331 core hexagonal cane.

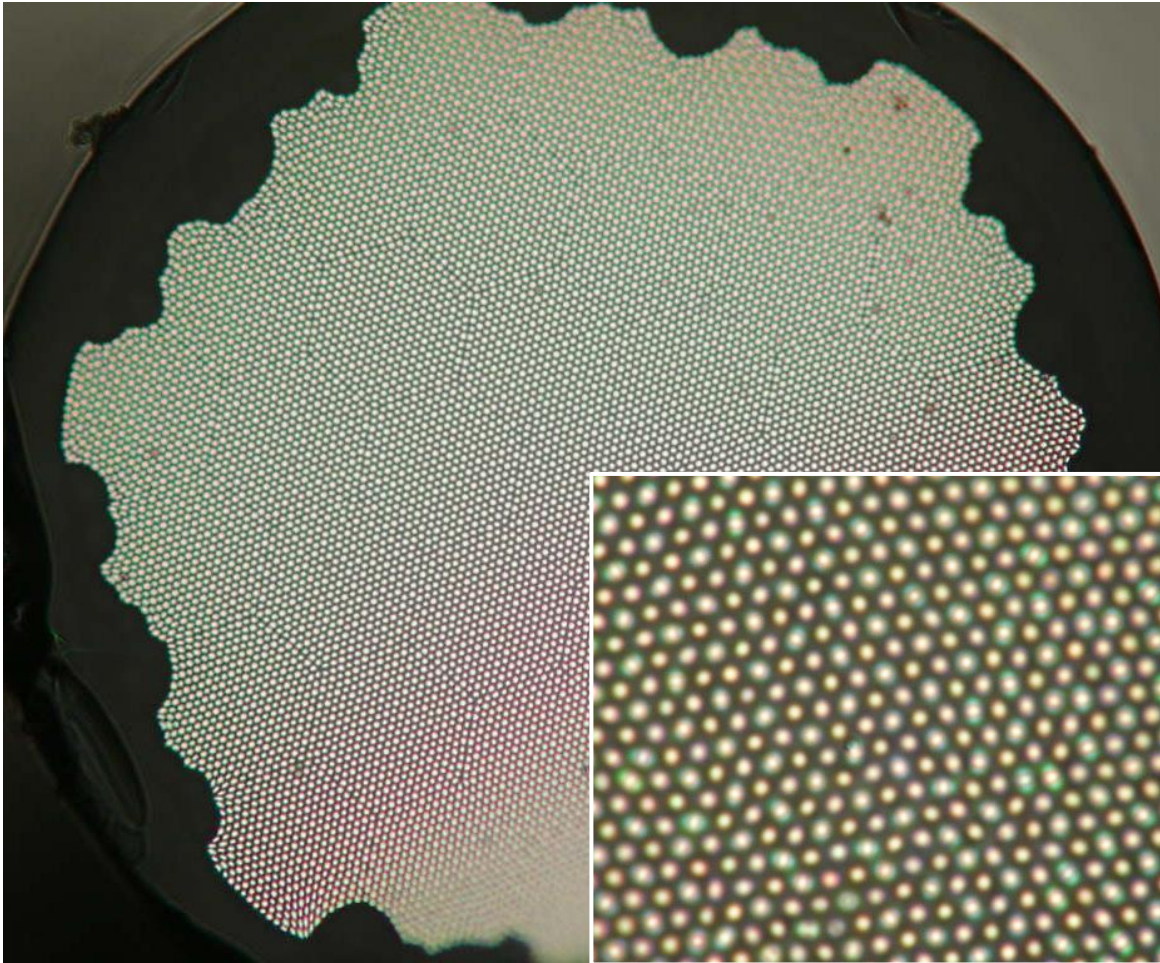


Figure 4.21: Transmission optical microscope images of the end face of a stub of 525 µm OD PGI9.

4.3.4.1 Characterisation

The test chart images in figure 4.22 show that even element 6 of group 6 is clearly visible at 550 nm, corresponding to a resolution of 114 line pairs per millimetre (LP/mm) or 4.38 µm. This indicates that PGI9 is our first fibre with an OD smaller than that of the FIGH-30-650S to offer comparable resolution at wavelengths shorter than 600 nm. Past 600 nm core crosstalk increases quicker with rising wavelength than in the FIGH-30-650S, likely due to the lower NA of this fibre's cores (0.3 compared to 0.39).

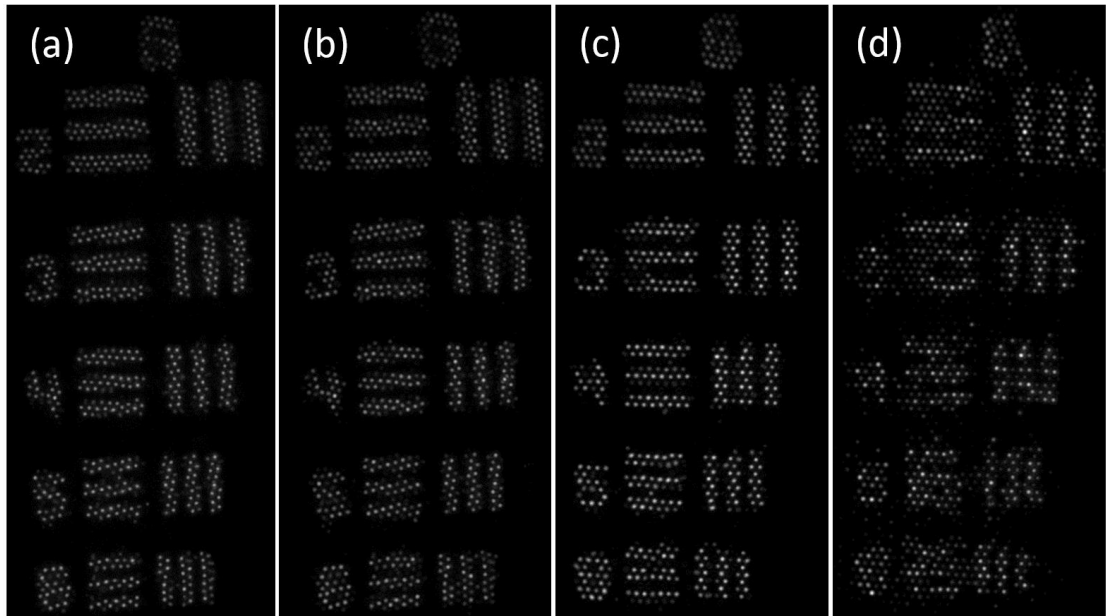


Figure 4.22: Images of group 6 elements of a US Air Force test target taken using the FIGH-30-650s (a) & (b) and PGI9 (c) & (d) at zero working distance, illuminated in transmission by 550 nm (a) & (c) and 650 nm (b) & (d) light. The lines of element 2 have a width of 7.81 μm .

4.3.5 Square array imaging fibre

The process of jacketing standard preforms to produce the two canes with a smaller core to cladding ratio, but the same outer diameter, requires significant time and effort to be spent on the drawing tower in preparation for the first stack. This prompted Dr. Jim Stone to investigate alternative stacking methods that could accommodate different sized canes, eliminating the need to jacket them. Jim demonstrated that a square array stacking method allowed the canes to be of different sizes but still produce easily stackable square second stage canes. At this point I began working with him in a joint effort to refine the fabrication techniques and produce the medical grade imaging fibre that is now being integrated into the prototype Panoptes 3-in-1 bronchoscope devices in Edinburgh.

4.3.5.1 Fabrication

Several of these fibres were fabricated, only to fail mechanically as the fibre crumbled away, even within the coating. We discovered this was due to microscopic surface imperfections on the preforms that were incorporated into the internal structure of the fibres. These were originally treated by the manufacturer using hydrofluoric acid etching until they cut this stage from the procedure, likely due to cost and safety concerns. Once we learned of this, we added an additional step to the very beginning of our fabrication processes where we flame polish the outer surface of the preforms. This was done in the CPPM fibre fabrication facility by using a hydrogen torch to raise the preform's surface temperature to the point where the surface softened and any defects were smoothed.

Figure 4.23 shows a preform lit from below by the light from the furnace. The top part was left untreated so light is being scattered from the abundance of surface defects, whereas the lower part had the defects removed by flame polishing. The flame polished preform was drawn down to 5 sets of 5 canes, each of 2.23, 2.52, 2.74, 2.95, or 3.17 mm in diameter. These 25 canes were stacked as in figure 4.24, using a square stacking jig. The decision to use a 5 by 5 stack was based on the fact that although a 3 by 3 would offer the most distinct core sizes, and therefore lowest nearest neighbour coupling, next nearest neighbour coupling would still be a greater issue, as it was in our previous hexagonal fibres. A 5 by 5 stack offered a good selection of disparate sizes, while also helping reduce next nearest neighbour coupling.



Figure 4.23: A graded index preform, lit from below by the furnace. The lower part has been flame polished to remove the surface imperfections that are causing the scattering seen from the top part of the preform, and weakness in the resulting fibre.

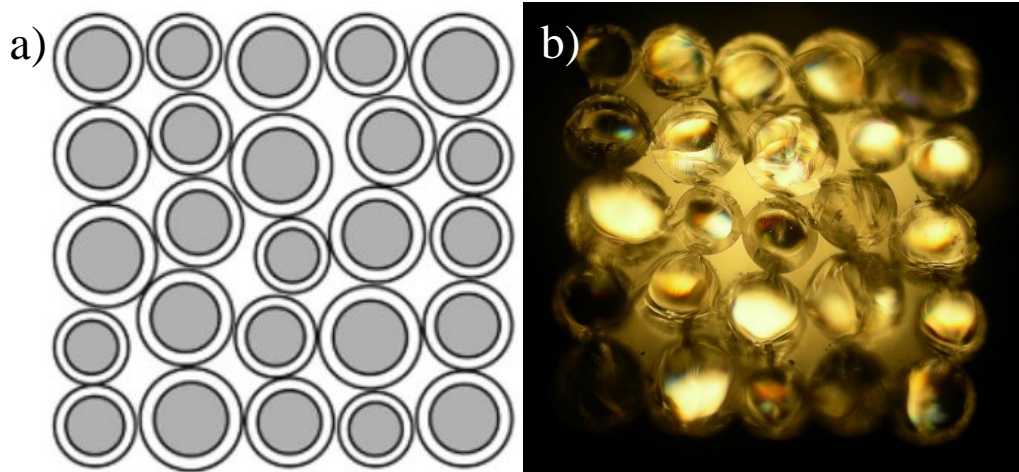


Figure 4.24: (a) the 25-cane square array stack design. (b) the 2.5 mm thick cane fabricated from one such stack.

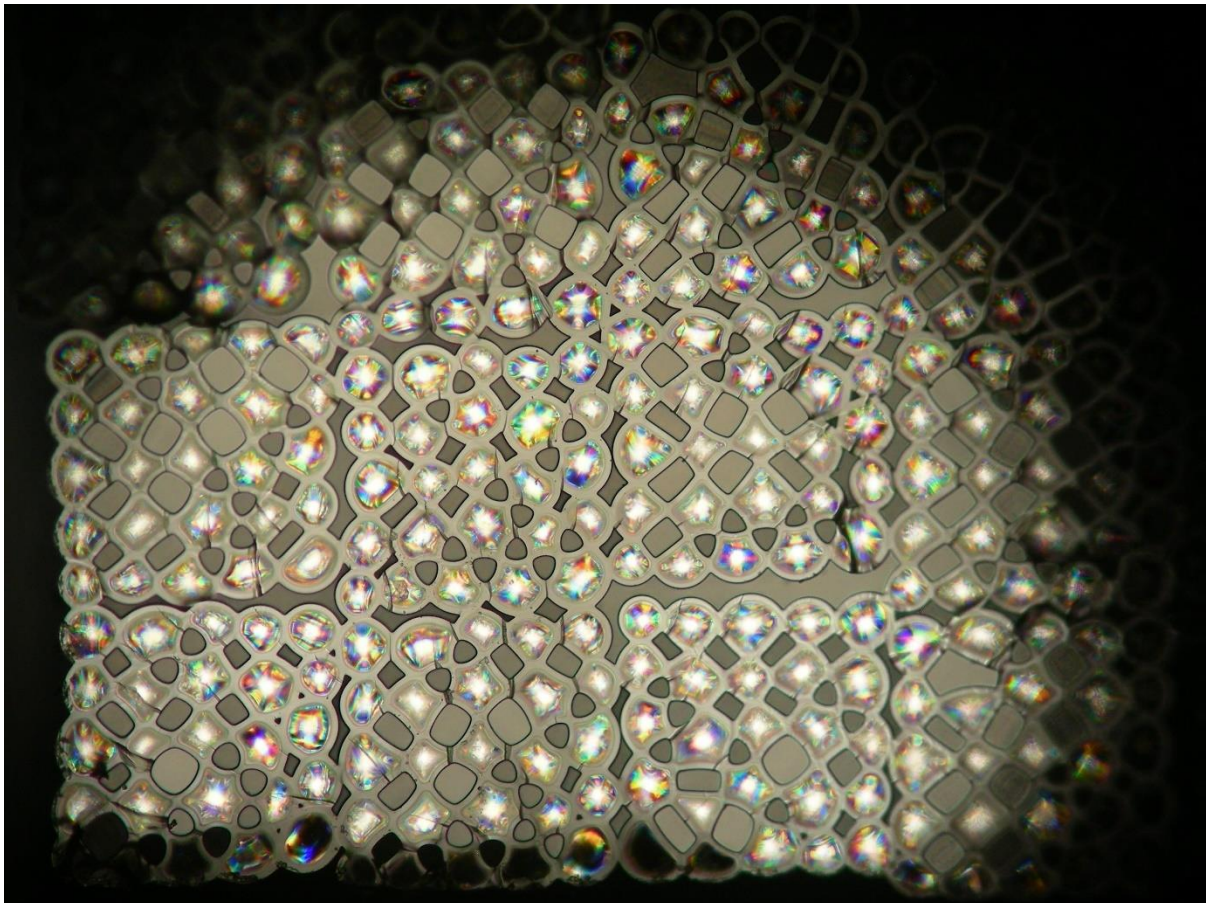


Figure 4.25: The corner of a 36×25 core square array cane. The 25 core elements are now roughly $750 \mu\text{m}$.

This stack is bound with PTFE tape, the bottom end fused using the vertical lathe and hydrogen torch, and a 40 cm long pure silica tube is fused to the top to act as a handle for the drawing process, allowing almost the whole stack to be used. The stack is drawn down using the same

techniques as with the hexagonal stacks to a width of 2.5 mm. A secondary stack of 36 canes is made and drawn down to 4.5 mm thickness using the same procedure, figure 4.25. Core shape deformities pervade the structure at this stage, but do not hinder the performance of the fibre as non-circular cores generally exhibit some amount of birefringence. Having different propagation constants for different polarisations helps to further reduce coupling to neighbouring cores. This also follows the logic established in section 4.1.3 on Anderson Localisation. It is critical that the interstitial holes remain open at this stage as they must be collapsed in the final fibre draw to ensure no bubbles are trapped in the structure.

A tertiary stack of 9 canes is made, inserted into a 22/19 mm OD/ID jacket and the edge holes packed out to produce the stack shown in figure 4.26.



Figure 4.26: A square array fibre stack ready to be drawn to preforms or fibre. 9 imaging canes can be seen supported by 4 sets of 5 packers inside a 22 mm OD jacket tube.

For the earlier iterations of this fibre these final stage stacks would be drawn to 5 mm canes (using a vacuum to collapse the interstitials) to allow multiple attempts at drawing strong fibre of good optical quality. However, this wastes material in the drop-off and top end of each cane. Having found stable tower parameters, all the subsequent draws done to produce fibre for Panoptes devices were done directly from the jacketed final stack (again with vacuum), producing fibre of the cross section shown in figure 4.27.

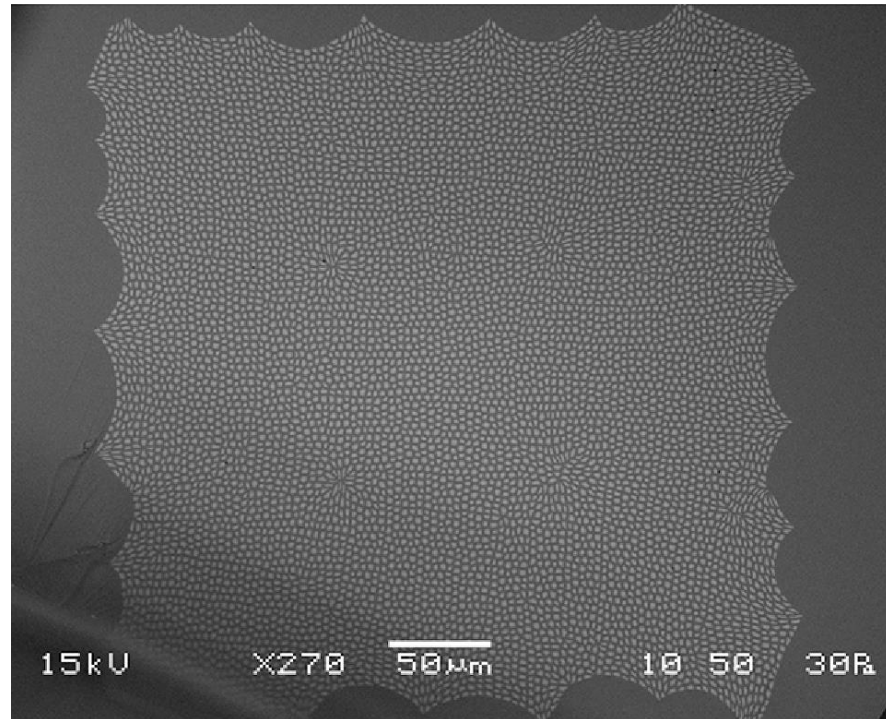


Figure 4.27: An SEM image of a stub of square array imaging fibre.

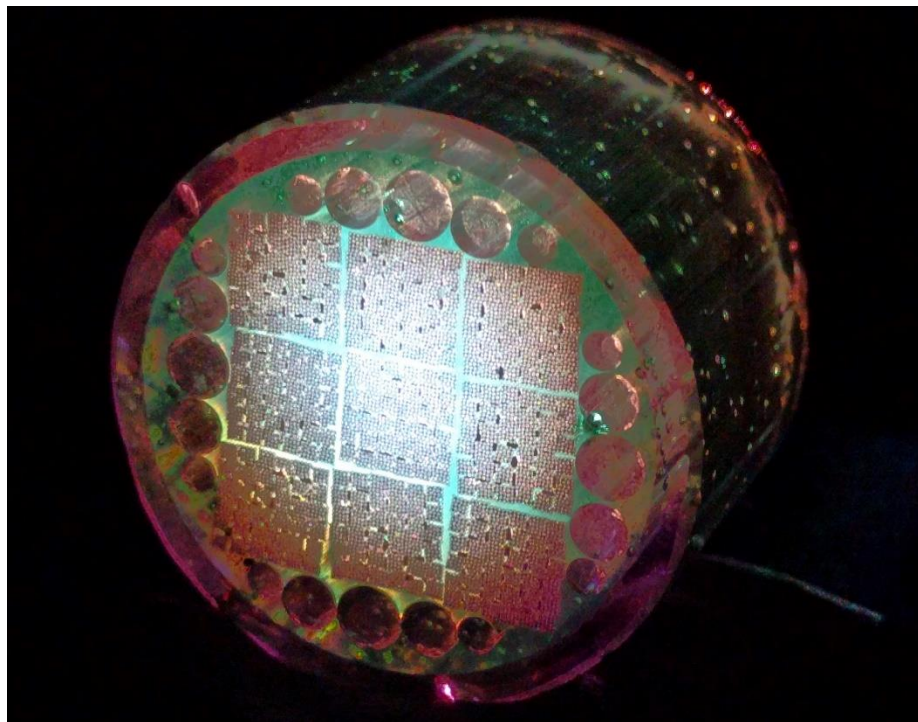


Figure 4.28: A stub of square array imaging fibre stack within its 22 mm OD jacket tube, filled with green dyed resin and lit from behind by supercontinuum light.

By filling the interstitials with resin, the preform could be chopped into 1 cm thick pucks and polished flat to produce the example pieces shown in figure 4.28. These have been used by the Proteus team in numerous outreach events to illustrate how imaging fibres are made, and how the thousands of light guiding cores work together to transmit a coherent image.

4.3.5.2 Characterisation

Beginning with the USAF test target images shown in figure 4.29, the imaging quality of the most recent square array fibres is shown to be similar to the FIGH-30-650S up to 600 nm wavelength, resolving features down to 3.10 μm (group 7 element 3). Although the imaging quality of the square array fibre suffers from more coupling than the FIGH-30-650S at 700 nm, it is still sufficient to resolve 3.91 μm features. By reaching this benchmark performance using only mass-produced telecoms material, this fibre design represents a highly competitive alternative to the already well established commercial fibres. In addition to this, the fabrication technique is simple and scalable, facilitating adaptation into an industrial technique. On these grounds we have published a paper describing the square array fibre and PGI9 titled *Low index contrast imaging fibres* in Optics Letters in 2017, and filed a patent to protect these designs and fabrication techniques [64].

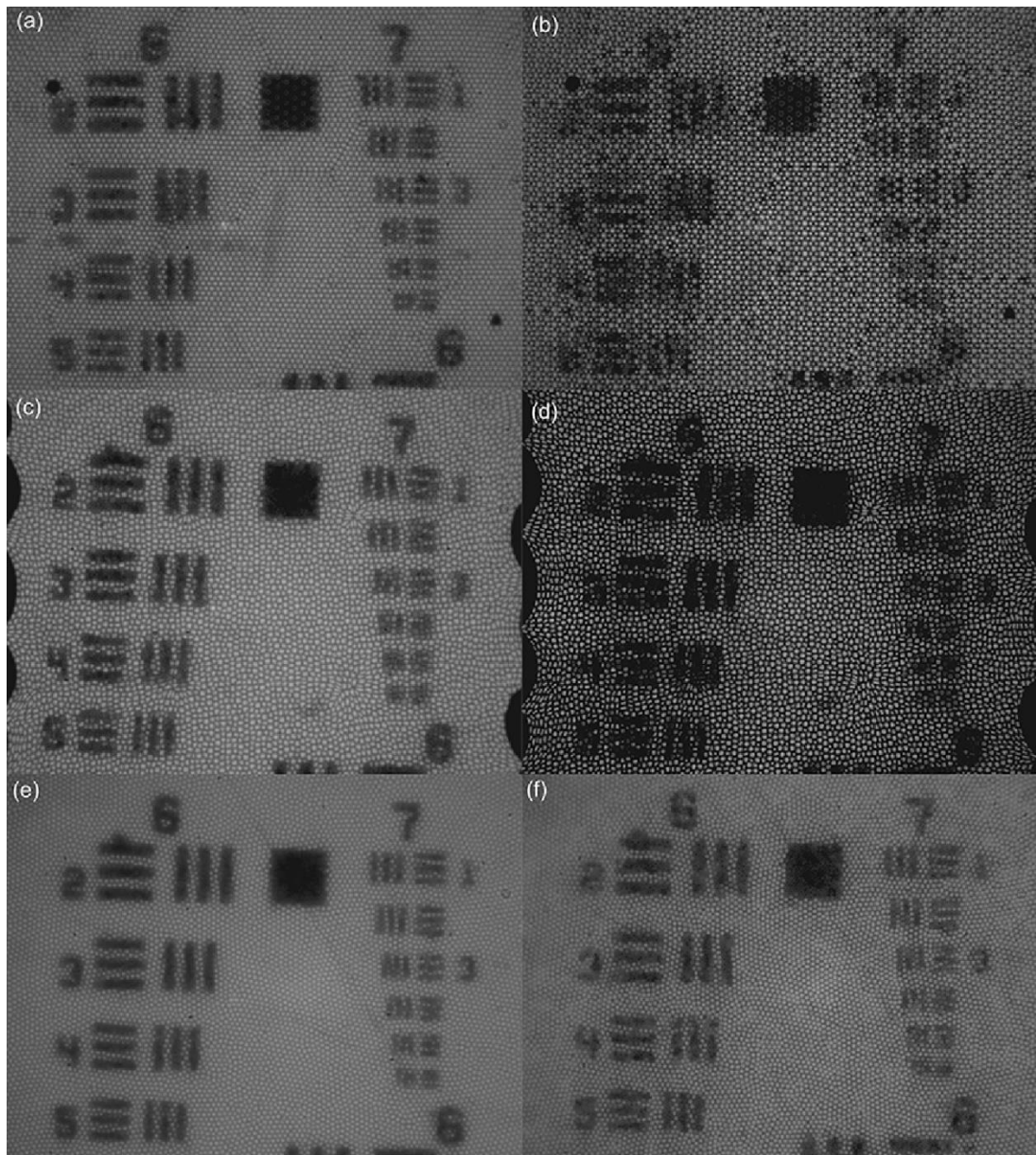


Figure 4.29: A series of USAF test target images taken using PGI9 (a & b), the square array fibre (c & d), and the FIGH-30-650S (e & f) at 520-600 nm (a, c, & e) and 650-700 nm (b, d, & f). The sides of the square at the top middle of each image (right of group 6 element 2) have a side width of 35 μm . The lines of group 7 element 3 are 3.1 μm thick.

4.4 Conclusion

I have presented a representative selection of solid imaging fibres that were developed for the Panoptes work package. The iterative process of their development involved far more intermediary stages, setbacks, and solutions than described in this chapter, which instead presents only the most significant strides taken towards the final medical-grade fibre designs. The fabrication techniques used for each fibre have been summarised, and their imaging quality characterised and compared.

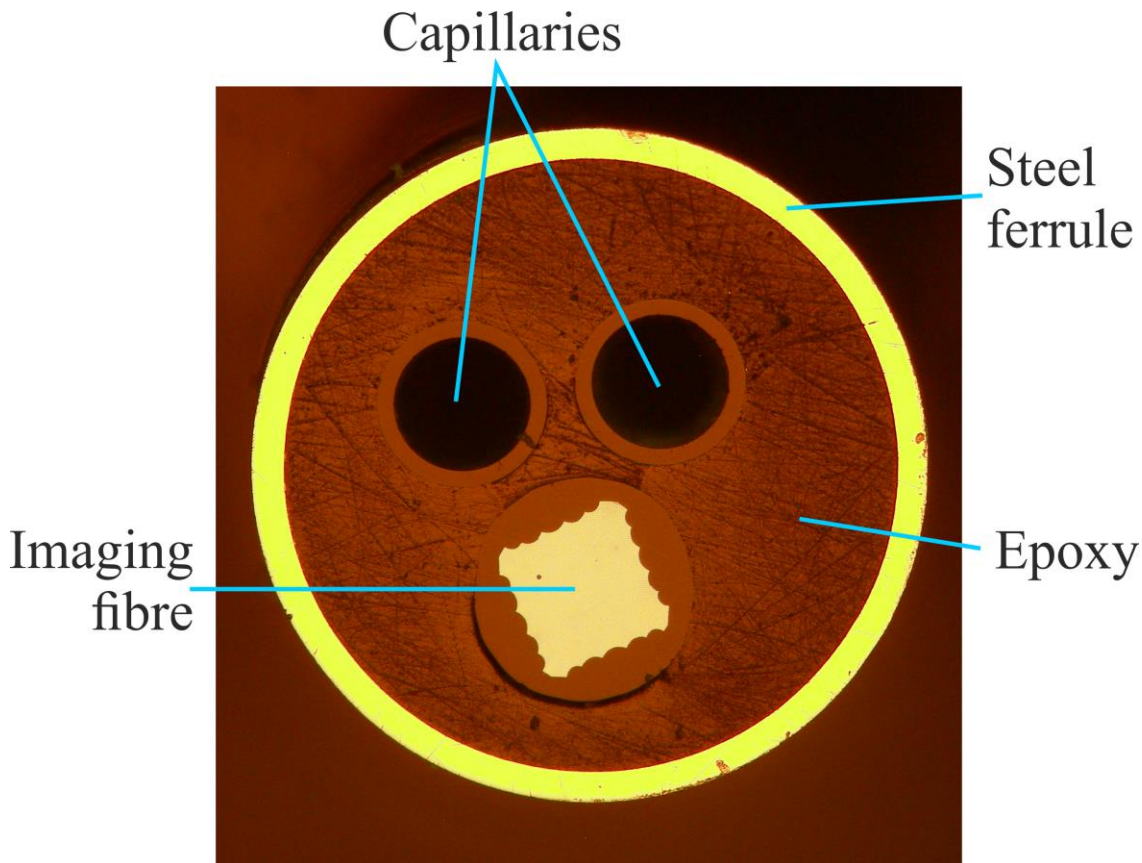


Figure 4.30: A microscope image of the end face of the final Panoptes probe, with 2 hollow capillaries and a square array imaging fibre encased in resin, within a stainless steel ferrule, illuminated in reflection.

The square array fibre has been incorporated into a bronchoscope probe system with two capillaries, shown in figure 4.30. The capillaries can be used to do local lavages as discussed in chapter 1.

From these experiments we have learned that the detrimental effects of core crosstalk to image quality of coherent fibre bundles can be minimised by arranging the cores so that no neighbours have the same diameter. The thousands of cores necessary for imaging can be regularly arranged in this way by employing multi-stacking techniques. The primary advantage of such imaging fibres is that they can resolve structures as small as $3\ \mu\text{m}$ with image quality that is competitive with world leading commercial equivalents, but without the need for expensive specialised doping techniques. Although, when made perfectly, hexagonally stacked fibres have marginally better performance than square array ones, the fact that a square array does not require each core to be jacketed greatly reduces fabrication time and workload, making them a better option for large scale commercialisation.

Chapter 5

Imaging fibre characterisation

A diverse range of imaging fibres have been fabricated during this project. Characterisation has formed a key step in the iterative process of their evolution, informing us of the effectiveness of each design choice. This chapter first discusses the relative merits and shortcomings of the methods most commonly used in industry, before presenting our group's quantitative characterisation technique. This was a key side project that I have driven to completion, and published in Optics Express in early 2017 [79].

5.1 Established methods

This section contains a brief description of the two methods most frequently used to characterise a fibre's imaging quality, as well as a common metric for quantising an optical system's performance – the modulation transfer function, or MFT.

5.1.1 Test target imaging

Already described in chapters 2 & 4, test targets have been used widely for many years to assess the imaging quality of not only optical fibres, but optical systems in general. The different forms of target all involve using geometries of known size to quantify the characteristics of an optical system. These characteristics include resolution, astigmatism, chromatic aberration, and more.

This method is simple and effective for quickly identifying issues in image quality. It is, however, not without its limitations. Consider the resolution investigations presented in chapter 4; the smallest elements that can be distinguished is a judgement that is made subjectively, and often varies person to person. This is compounded by the fact that many results published using this technique do not use the elements, but the numbers on the target as their standard instead [80]. It also does not consider the contrast of the images produced, which can also diminish their clarity. Several methods exist that are capable of mathematically quantifying the difference between two similar images. These include the mean square error (MSE) and mean structural similarity index

(MSSIM), both of which can be used to measure the fidelity of a test target image after transmission through an imaging fibre [81].

A further issue with the use of test targets is that imaging fibres (especially prototypes) can possess inhomogeneous core structures. Each set of elements only tests a very small area of the field of view, so it could be that the elements close to the average resolution limit of the fibre lie on a particularly good or bad area.

5.1.2 Coupled power characterisation

By coupling light into a single core and imaging the near-field of the output face, the percentage power that moves to the core's neighbours due to crosstalk can be measured. I carried out a basic version of this experiment on my 50,000-core imaging fibre in chapter 4, and it has also featured prominently in a paper by X. Chen *et al.* in *Optics Express* [82]. In their paper they describe the theoretical and experimental analysis of core crosstalk in a commercial imaging fibre, and its implications on imaging quality.

Doing these measurements precisely takes time, so characterising a representative sample of the thousands of cores in an imaging fibre is highly impractical. Its recurring use in literature for studying just a few imaging fibre cores is questionable because of the inhomogeneity of the structures, as mentioned in the last section.

5.1.3 Modulation transfer function

Although rarely used to characterise imaging fibres, the modulation transfer function (MTF) provides a quantitative measure of the contrast that an imaging system can achieve with a range of spatial frequencies [83]. The measurement is usually performed using either a “knife edge”, with a single sharp transition from opaque to transparent, or a row of identical parallel opaque bars of known width as the standard object. For example, the latter standard can consist of a set of thin lead rods when characterising an x-ray imaging system [84], or a Ronchi pattern mask for visible wavelengths [85]. Usually, only one spatial frequency can be investigated at a time using these types of pattern. More recently, other patterns that allow a spectrum of spatial frequencies to be investigated simultaneously, such as a Steiner Star, have seen use [86]. In this case the technique was combined with Fourier analysis to form an automated technique of obtaining the transfer function.

Although this is arguably the most effective characterisation method I have discussed, it is still imperfect due to the targets that are used. This is because they are almost always of binary opacity, essentially forming some kind of a square wave. The mathematics of the MTF are instead based on finding the contrast of a sinusoidal wave intensity pattern [87]. Consequently, whenever the MTF is used it is almost always an estimate.

5.2 Quantitative interferometric characterisation

My technique for quantitatively characterising imaging fibres uses an interference pattern of continuously variable wavelength and pitch as the standard image. The output images of the fibre being tested are analysed using two methods to investigate the visibility of the fringes, which decreases as core crosstalk deteriorates the image quality.

In the following sections I summarise the basic theory of the technique, the preliminary experiments that were not included in the paper, and the key results it does present.

5.2.1 Theory and preliminary work

The visibility of an interference pattern depends on how well correlated the phase of the two beams is at the point of arrival, as well as their relative intensities – maximum fringe visibility requires beams of equal intensity. Matching the phase of the beams at the point of recombination requires that the paths they take be identical in length to within their coherence length. The coherence length of light is inversely proportional to its spectral bandwidth, $\Delta\lambda$, as

$$L = \frac{2\ln(2)}{\pi n} \frac{\lambda^2}{\Delta\lambda}. \quad (19)$$

This means that, although possible to produce high visibility fringes with white light, the two beams must travel the same optical path to within less than one wavelength. Therefore, for the initial proof of concept experiment I chose a 633 nm helium neon laser as the source as its extremely narrow linewidth provides a coherence length greater than 10 cm without additional stabilisation.

The experiment was first assembled as in figure 5.1. The fringe pitch, Λ , can be varied by changing the angle θ that the beams are recombined. The relationship is described by the equation

$$\Lambda = \frac{\lambda}{2\sin\theta}. \quad (20)$$

The angle θ was set by measuring the distance between the points at which the mirrors reflect the beams coming from the beamsplitter, and setting the test fibre at the corresponding distance that is calculated using simple trigonometry. It was relatively simple to ensure that the triangle was isosceles by observing the reflections of each beam from the fibre end face (the reflection is particularly strong if a metal ferrule is used to connectorise the fibre) and ensuring that the reflected beam coincided with its incoming counterpart.

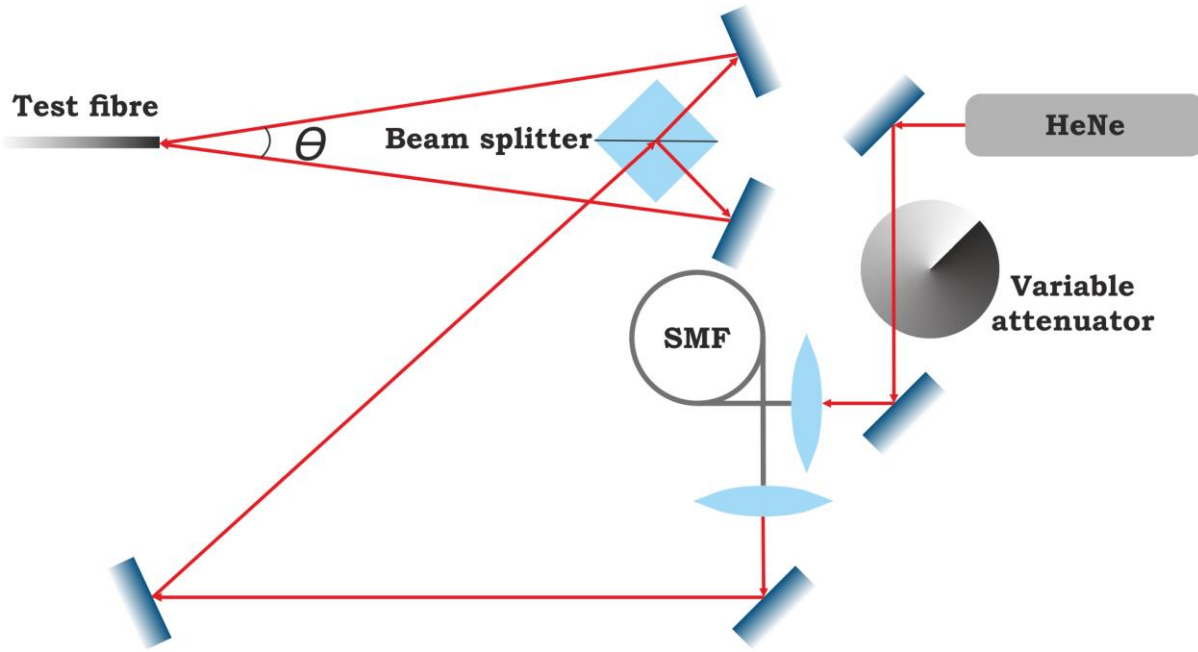


Figure 5.1: A diagram of the prototype interferometric imaging fibre characterisation setup. SMF stands for single mode fibre.

Figure 5.2 shows the decrease in fringe visibility when changing from a pitch of 13 to 9 μm . With this evidence that the technique could be useful, the next step was to develop methods of quantitatively analysing the fringe visibility in these types of image.

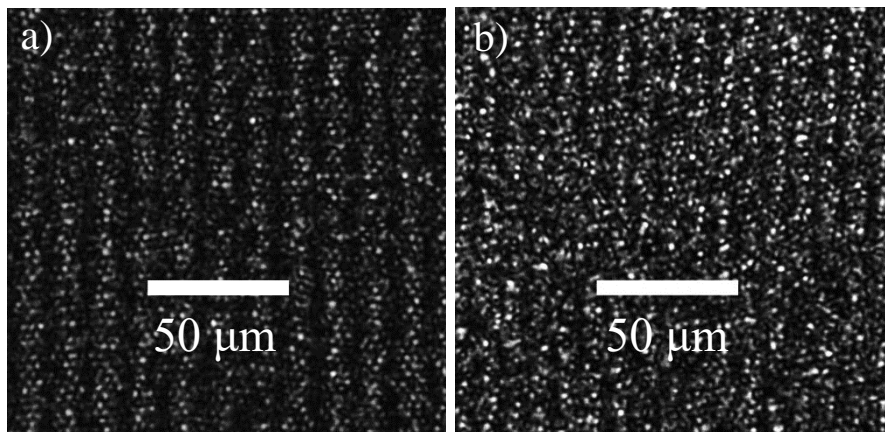


Figure 5.2: Images of interference patterns taken using the 1 mm OD 50,000-core fibre and the 633 nm HeNe laser. The fringes have a 13 μm pitch in (a), and 8 μm in (b).

5.2.2 Fringe visibility analysis

The first method I developed involves binning the pixels parallel to the fringes, and fitting a sine squared function to the resulting data points. A typical plot is shown in figure 5.3.

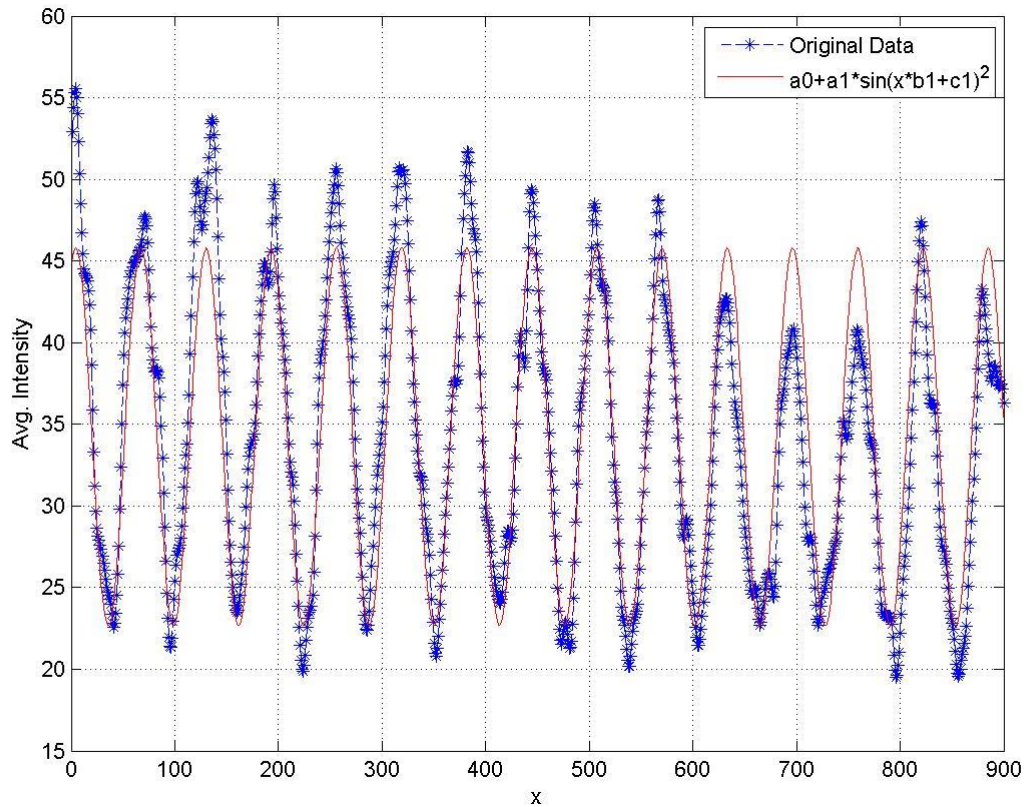


Figure 5.3: The binned intensity data in blue and a sinusoidal fit in red.

The form of curve fitted to the above data is given by

$$I(x) = a_0 + a_1 \sin^2(bx + c), \quad (21)$$

and the fringe visibility can be found using the constants a_0 and a_1

$$Visibility = \frac{a_1}{a_1 + a_0}. \quad (22)$$

This method requires that the fringes be aligned either vertically or horizontally to the CCD to facilitate accurate binning of the pixels. Using a goniometer to rotate the camera relative to the fringes was the simplest way of achieving this. The fringes were properly aligned when the visibility value from the binned data was at its highest.

The second method begins by taking a fast Fourier transform (FFT) of the image, two examples of which are in figure 5.4. The features of this FFT are derived from a combination of both the structures of the fringe pattern and the fibre itself. In the very centre of each image is the DC peak, corresponding to the overall brightness of the original image. To either side of this are the satellite peaks attributed to the interference pattern. Around these are features corresponding to some of the highest spatial frequency details of the image; the core pattern of the fibre. This manifests as a ring in figure 5.4 (a) as the FIGH-30-650S has no long-range order or directionality to its core

pattern. In figure 5.4 (b), instead of a ring there is a set of 6 broad peaks, corresponding to the close packed hexagonal core structure and spacing in the 50,000-core fibre.

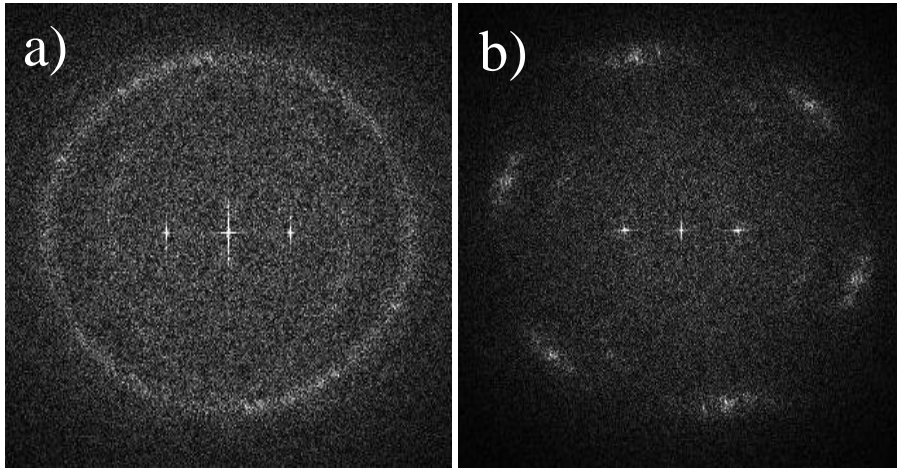


Figure 5.4: Two 2D FFTs of fringe images taken using a) the FIGH-30-650S, and b) the 50,000-core fibre. They have been cropped down to spatial frequencies equal to, or lower than, those corresponding to features of the fibres' modes.

By normalising the intensity of the satellite peaks against the DC peak, an accurate measure of the contrast of the fringes in the original image is obtained - hereafter called the Fourier contrast. This has the advantage of being insensitive to the orientation of the fringes relative to the CCD, as well as providing the aforementioned information on the structure of the fibre under investigation.

With the success of the preliminary work, the next step in developing the technique was to rebuild the experiment with a variable wavelength light source.

5.2.3 Final experiment design

I replaced the HeNe laser with a visible supercontinuum source; the PCF, kindly provided by Jim Stone, was pumped by a 1064 nm pulsed microchip laser. By coupling the beam into an Edmund Optics manual mini monochromator (part #37-598) the beam's wavelength is continuously variable between 450 nm (the short wavelength cutoff of the supercontinuum) and 800 nm (limited by the transmission window of the lens' anti-reflection coatings [88]). The final experiment design is shown in figure 5.5. A delay arm was added to the beam path at (3) in figure 5.5 in order to balance the two path lengths to within the coherence length of the new source – at least 22 μm , dependant on alignment. All lenses after the supercontinuum fibre were replaced with achromatic equivalents to avoid having to realign parts of the experiment when changing wavelength.

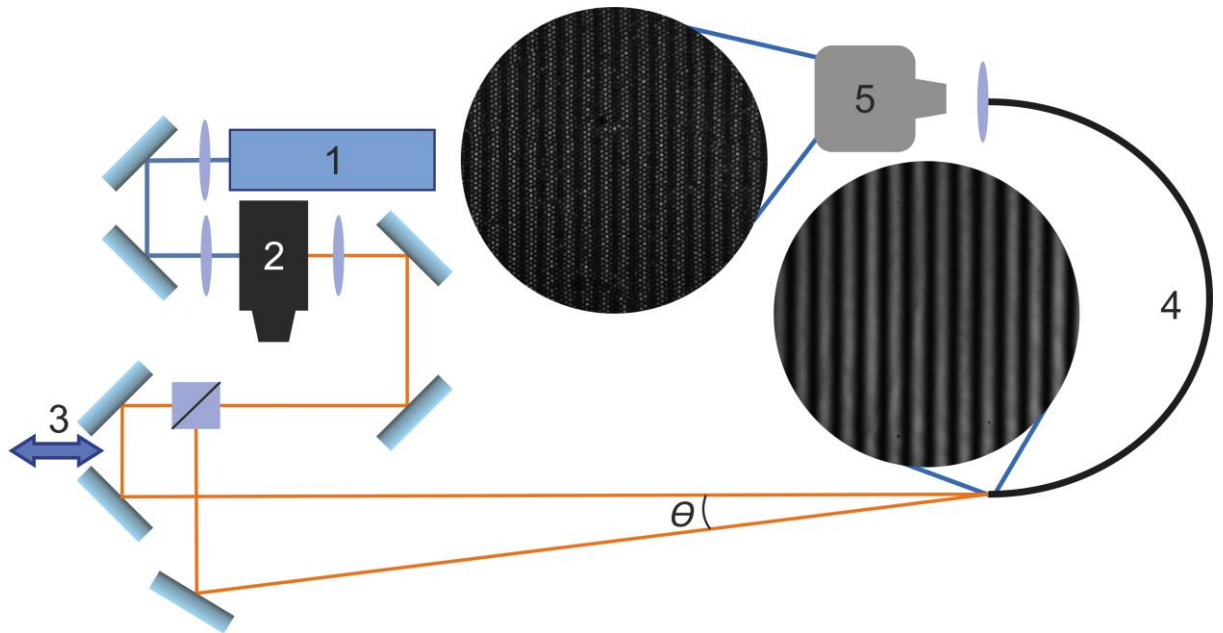


Figure 5.5: Diagram of the apparatus used: (1) supercontinuum source, (2) mini-monochromator (3) delay line mirrors (4) imaging fiber under test (5) camera. The insets show an image of the interference pattern formed on the input end of the fiber and the resulting near field image at the test fibre's output. Taken directly from my paper [89].



Figure 5.6: An image of the beam profile from the monochromator.

Figure 5.6 shows the beam profile from the monochromator – it is linear because the point-like beam of supercontinuum is spread by the monochromator's grating and filtered by the output slit. This also means that although it appears to the eye to be monochromatic, the beam profile actually has a short and a long wavelength end, spanning roughly 5 nm. One consequence of this is that the beams must be overlapped precisely so that each wavelength falls the same wavelength in its counterpart. Another is a strong dependence of fringe visibility on the focus of the beams – the different wavelengths overlap when defocused, decreasing the fringe visibility. With accurate alignment, because the fibre is small by comparison to the beams it acts as an additional slit, effectively filtering the light to a bandwidth of approximately 1 nm.

I found that the boundaries of the image act as a square window when the FFT is applied. The Fourier transform of a square wave is a Sinc function. This has the effect of subtly spreading the features of the transform (including the central peaks) into further small satellite peaks as the image

is effectively convolved with a low frequency top hat function. For this reason, I rewrote the image analysis code to apply a Gaussian window mask to the image prior to the FFT [90]. Because the Fourier transform of a Gaussian function is also Gaussian the features of the FFT are now resolved more clearly as single spots instead of multiple, noisy peaks. Figure 5.7 shows the effectiveness of this windowing technique when compared to figure 5.4. It is now clear that the rings, or 6-fold peaks, from the core lattices of the two fibres are convolved with the three central peaks.

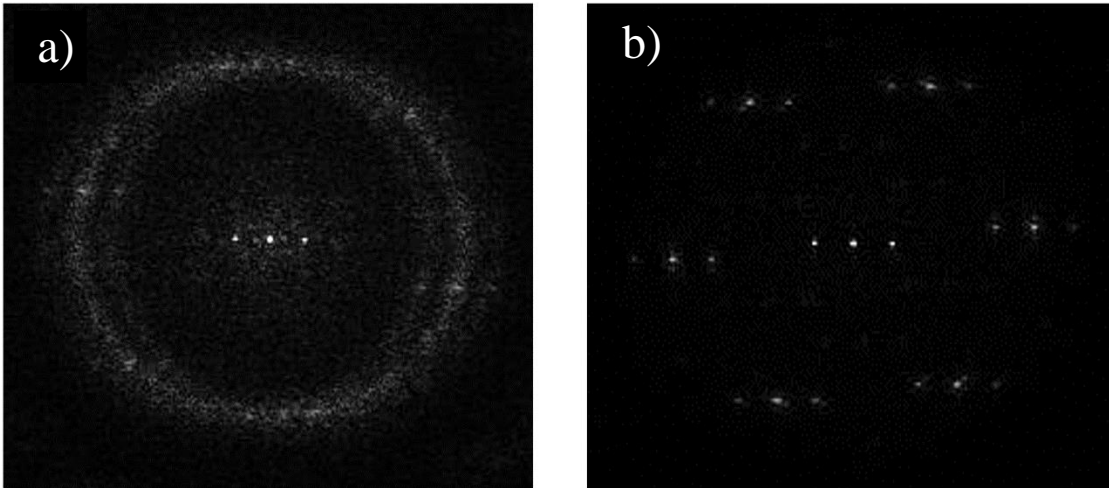


Figure 5.7: FFTs of fringe images from the (a) FIGH-30-650S and (b) PGI9 after applying a Gaussian window.

5.2.4 Data

For the purposes of the paper, two fibres of diameters 525 and 470 μm were drawn from PGI9's stack, called PGI9-525 and PGI9-470 respectively. They were structurally identical, but different scale versions of each other. This meant that their performance profiles were expected to also be identical in shape, but shifted to different wavelengths due to increased crosstalk in the smaller fibre. This allowed the characterisation technique itself to be tested as we knew the expected relationship between the datasets. Fujikura's FIGH-30-650S was also used for comparison as it has been a reliable performance benchmark for many groups in the field of imaging fibres.

I set the angle between the interferometer's beams to $\theta = 2.29^\circ$, corresponding to a fringe period of 15 μm at 600 nm. For each fibre I swept the wavelength from 500 to 700 nm in 10 nm increments and recorded both the binning and Fourier contrast. From this data figure 5.8 was produced.

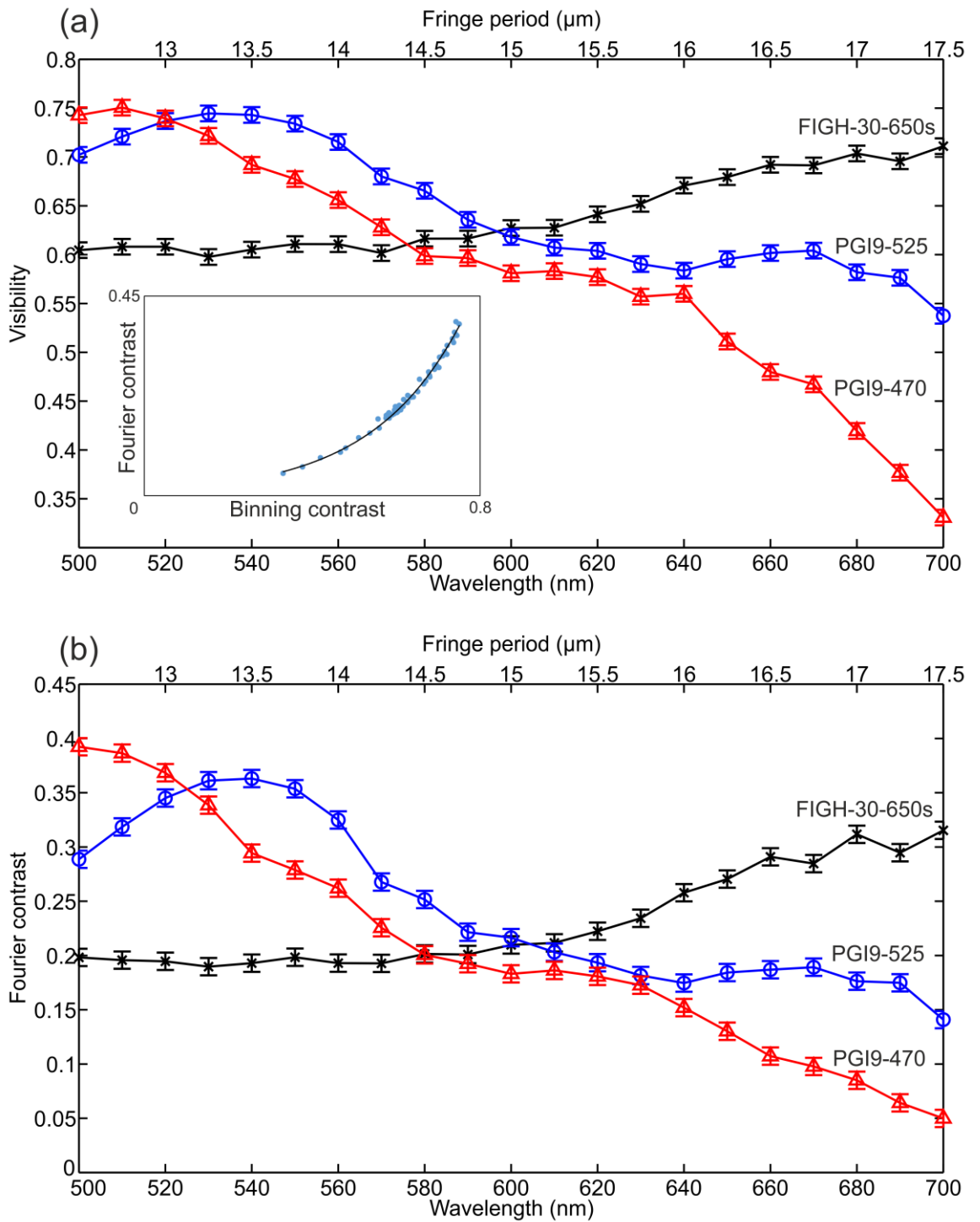


Figure 5.8: Fringe visibility determined by binning method (a) and Fourier method (b) for each of the three fibres, versus wavelength. Error bars represent the standard deviation of a series of 14 data points taken at a single wavelength, realigning the system between each measurement. The beam angle θ of $2.2 \pm 0.1^\circ$ was chosen to give a fringe period of $15 \mu\text{m}$ at $\lambda = 600 \text{ nm}$; the period at other wavelengths is indicated on the upper x axis. The inset in (a) is a plot of each wavelength's Fourier contrast value (y -axis) against its corresponding binning-derived visibility value (x -axis), with an exponential fit; $y = 0.0115e^{4.669x}$.

Chapter 5: Imaging fibre characterisation

As indicated by equation 20, the pitch of the fringes is dependent on wavelength. For this reason, the top axis has been added to each graph. The inset in figure 5.5(a) is a plot of each Fourier contrast data point against its counterpart visibility value from the binning method. The trends shown using each method correlate well with their counterparts from the other method – a strong indication that both function as intended. This is clear when observing the wavelengths at which each curve crosses another – they are the same in both plots (a) and (b) of figure 5.8.

From figure 5.8 we can see that the performance of both PGI9-525 and PGI9-470 is particularly good at the short wavelengths where smaller core spacing provides higher resolution imaging, up until the wavelengths where crosstalk becomes detrimental. It is interesting that their performance profiles, although similar, also show differences that were not expected considering their identical structures. This could be explained by a slight dependence of the results on the orientation of our fibres' core patterns relative to the fringes; both Fourier and binning contrast rise when the rows of cores run parallel to the fringes. This effect was particularly noticeable when using fine fringes, producing regular light and dark rows of cores when alignment is good, otherwise, with only slight misalignment moiré patterns were observed.

The upwards trend of the FIGH-30-650S' performance with increasing wavelength is a strong indication that, in this regime, it is limited by its core spacing instead of crosstalk. At short wavelengths its core spacing of 3.2 μm (compared to just 2.1 μm in PGI9-470) produces poor contrast fringe images. As the pitch increases with wavelength, and crosstalk is still weak, the fibre is simply imaging the increasingly large features better.

By also scanning through different beam angles to vary the fringe pitch, surface plots such as the one in figure 5.9 can be produced. In this case, the performance of an early graded index Panoptes fibre was tested, showing that it has reasonable performance at short wavelengths and large fringe periods, but abysmal performance past 600 nm wavelength. Although useful for a general impression of the overall performance of these fibres, these plots take a long time to produce, and are less useful for direct comparison of two fibres.

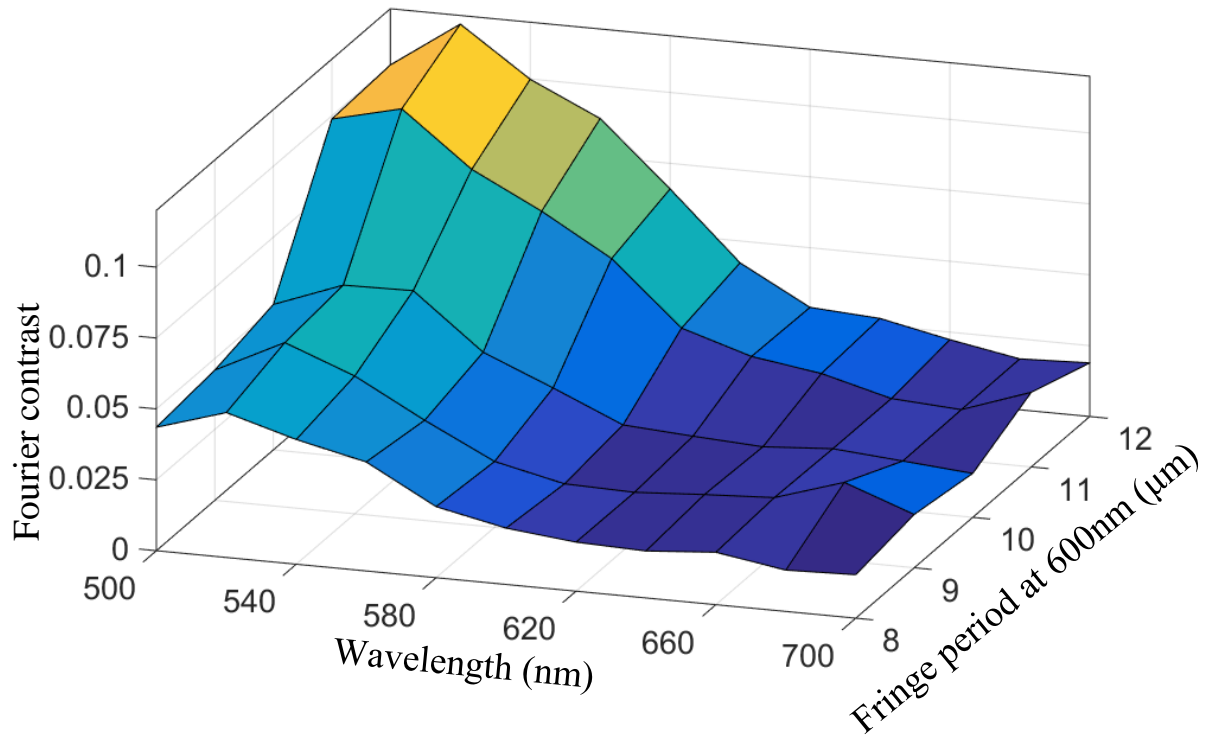


Figure 5.9: A plot of the performance of an early graded index imaging fibre for the Panoptes work package that had very poor performance past 600 nm. The Fourier contrast is also lower than it should be by a factor of 2 due to a mathematical error in early versions of the code.

5.2.5 Further development

This technique has already proved valuable for quantifying the subtle differences that occur in the imaging capabilities of similar fibres, prompting the question; can it be useful for analysing other imaging apparatus as well? Clearly, any imaging apparatus that relies on a scanning spot, such as the phased array fibres discussed in chapter 4, cannot be analysed using this technique as there is no target to scatter light off. It is also important to consider the implications of the use of coherent light. This means the technique will only work in experiments that image the local light intensity without retaining phase information. Fibres that do coherently transmit phase information will instead form a different interference pattern directly on the detector. I can, however, envisage a similar setup that can characterise infra-red imaging fibre bundles, such as the leached fibre bundles mentioned in chapter 4.

A potential improvement to the experiment that would be relatively easy to make is to calculate the MTF (discussed in section 5.1.3) instead of visibility from the binned fringe data. Because the MTF is supposed to be performed using sinusoidal test patterns, my interferometer could offer a far better imaging standard than the square wave patterns that are often used in industry.

Chapter 6

Air-clad imaging fibres

6.1 Introduction

As established at the beginning of chapter 4, the two primary methods of reducing crosstalk between cores are to either better confine and isolate the evanescent fields from one another, or ensure a mismatch of the propagation constants of the light within them. The latter option was explored during the production of the imaging fibres discussed in chapter 4. From section 6.4 onwards I describe my design and fabrication techniques for imaging fibres with an extremely high NA, achieved by using a capillary lattice as the cladding material, with an effective index close to that of air. Before this, I will describe the origins of the project, and some background of recently published research into high NA optical fibres, or fibre designs that offer similar advantages such as functionality in the infra-red.

This side project began life as an idea in the head of Proteus' Dr. Jim Stone, who was inspired by the work he carried out during his PhD in photonic crystal fibres (PCF) [91]. Some of the fibres he produced were designed to confine the mode excited by infra-red laser pulses to such a small volume of glass that the field amplitude was great enough that the resulting nonlinearity generates white supercontinuum light. One such fibre, shown in figure 6.1, has been used as the broadband light source in the dispersion characterisation rig discussed in chapter 2, and my quantitative characterisation technique discussed in chapter 5, as well as all of the characterisation images in chapter 4 where the samples were illuminated in transmission.

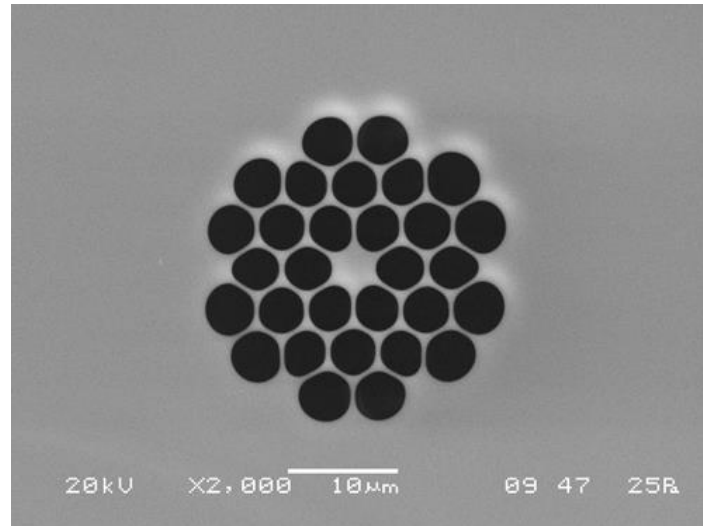


Figure 6.1: An SEM image of the end face of a PCF designed for supercontinuum generation [92].

The walls of the array of silica capillaries around the core of highly nonlinear fibres are too thin to effectively guide light of visible or longer wavelengths, so when light interacts with this region it is instead affected by a refractive index that is only slightly above that of air. This provides a far larger index step to the core than anything that can be achieved by doping, due to the stresses induced in the preform fabrication stage as discussed in chapters 2 and 4.

It has long been recognised that an air cladding would be highly advantageous to imaging fibres, but due to the difficulties associated with scaling up the number of cores in the stack-and-draw process they have remained a white whale for many research groups.

6.2 Prior work

With the potential for high resolution imaging at wavelengths into the infra-red, air-clad imaging fibres present many advantages that traditional silica imaging fibre bundles cannot hope to achieve. In this section previous attempts at fabricating similar multi-core PCF structures, as well as a selection of other types of optical fibres for infra-red imaging are discussed.

6.2.1 Hollow core imaging fibres

First discussed in chapter 2, hollow core fibres guide light due to the anti-resonance property of their cladding. This means that they are not limited to wavelengths that have low loss in silica, but can in fact guide light well past $3\ \mu\text{m}$ [93]. Imaging fibres that operate in this regime would be extremely useful for thermal imaging in industry, medicine [94, 95] and defence applications. One of the most effective examples of this technology is shown in figure 6.2.

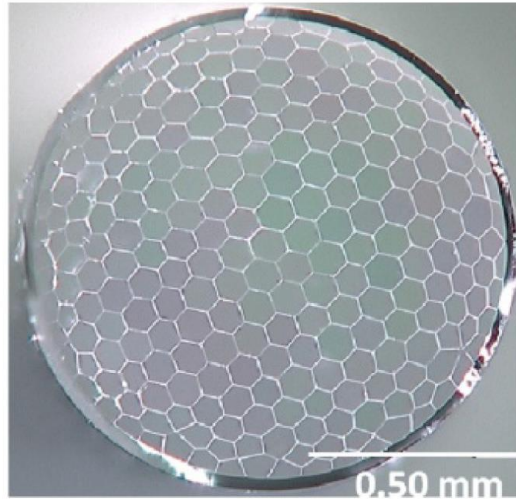


Figure 6.2: A hollow core imaging fibre [96].

Fabricated by Kobayashi *et al.* and published in their 2016 optics express paper; “Multi-element hollow-core anti-resonant fiber for infrared thermal imaging”, the fibre is limited to only 245 cores [96]. This is due to a combination of their large core size (more than $20\ \mu\text{m}$ in most cases to accommodate the wide fundamental modes at thermal wavelengths) and the practical limitations of the traditional stack and draw techniques. Rudimentary imaging was demonstrated, shown in figure 6.3.

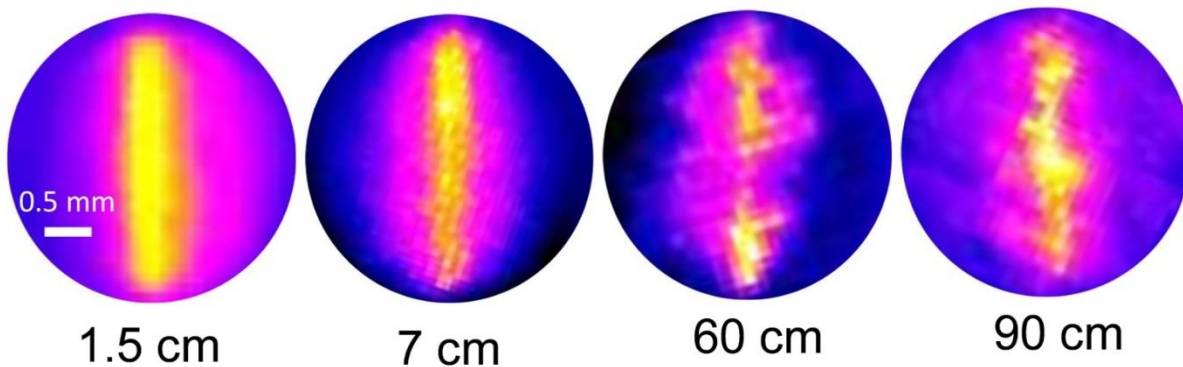


Figure 6.3: Thermal ($3\text{-}5\ \mu\text{m}$ wavelength) imaging of a heated $200\ \mu\text{m}$ thick wire using different lengths of the hollow core imaging fibre [96].

6.2.2 Chalcogenide glass fibre bundles

Chalcogenide glasses often have longer wavelength transmission windows, and thermal compatibility with certain low index polymers and other soft glasses makes them attractive materials for thermal imaging purposes. B. Zhang *et al.* fabricated the leached fibre bundle shown in figure 4.4 of chapter 4 in 2015 for thermal imaging [97].

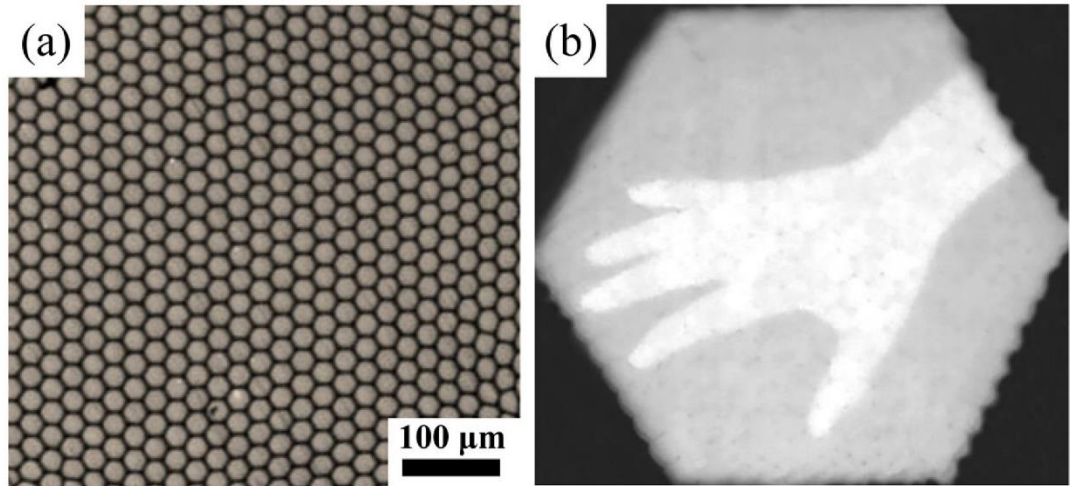


Figure 6.4: a) An optical image of the GATSe/PEI thermal imaging fibre bundle's core structure. b) A thermal image of a human hand using the 5 cm fibre bundle and an IR camera [98].

The fibre consists of approximately 200,000 15 μm diameter Ge-As-Te-Se chalcogenide glass cores in a low index polyetherimide cladding. They demonstrate highly effective thermal imaging, as seen in figure 6.4, albeit using a length of only 5 cm.

6.2.3 Multi-core photonic crystal fibres

Multi-core PCFs have been developed primarily for use as fibre lasers [99] and high-power femtosecond pulse transmission [100]. To my knowledge, no published fibre has had more than 19 solid cores within common air cladding. An unpublished result of the CPPM's coherent anti-Stokes Raman scattering (CARS) Explorer project in 2011, the fibre in figure 6.5 contains 30 birefringent cores within an air-filled capillary cladding. Its existence was unknown to me until well after I had fabricated my fourth air-clad fibre, discussed later in this chapter.

Ali Muir fabricated this fibre as an investigation into the feasibility of using PCF stack and draw techniques to produce an air-clad coherent fibre bundle for imaging. This branch of the CARS project was set aside to focus on phased array and hollow core imaging, despite active interest from commercial parties such as Mauna Kea Technologies. This was likely due to the apparent difficulty in scaling the structure to higher core numbers.

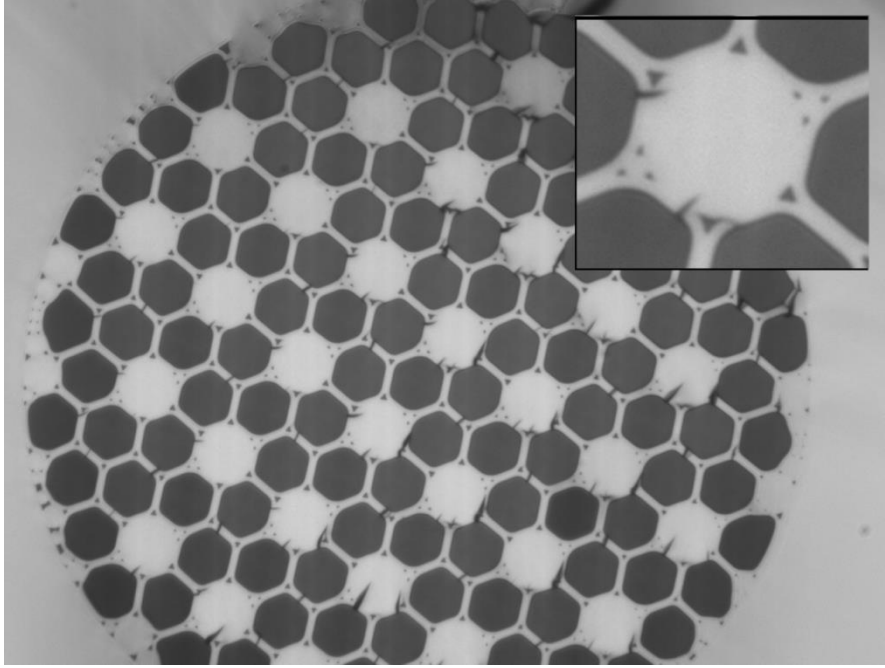


Figure 6.5: A 30 core PCF designed and fabricated by Dr. Alistair Muir. The inset shows two small interstitial inclusions to cause the cores to be birefringent.

6.2.4 Disordered fibres

De Raedt *et al.* built on Abdullaev and Abdullaev's theoretical work (discussed in chapter 4) in their 1989 Physical Review Letter in which they explore the mathematics and theory of Anderson Localisation applied to 2D waveguides at its logical extreme; a distribution of refractive index that is entirely random in 2 transverse dimensions and invariant in the longitudinal one. They show mathematically that the random scattering that occurs in the transverse direction interferes in such a way that an input beam will spread to a certain transverse localisation length during propagation, but no further.

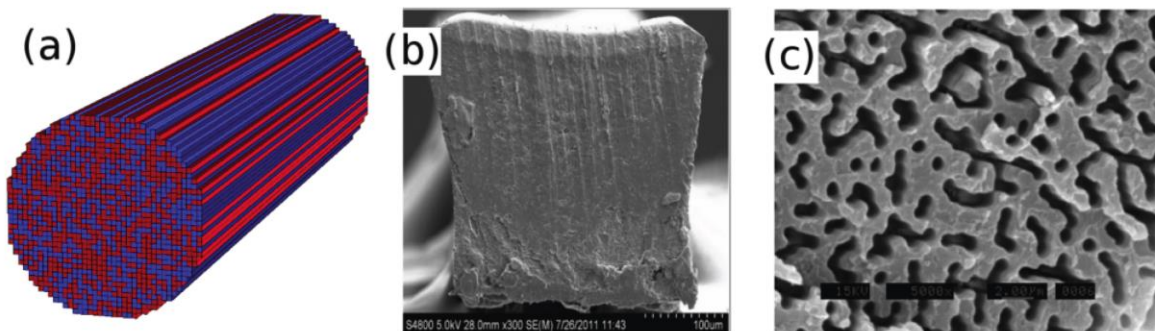


Figure 6.6: Random polymer fibre fabricated by Karbasi *et al.* a) a diagram of an example of random PMMA and PS fibre stacking. b) an SEM image of the fibre end. c) the fibre tip after dissolving away some of the PMMA [80,101].

One of the first experimental demonstrations of Anderson Localisation, published by Karbasi *et al.* in 2012, showed that the diameter of a propagating beam in a polymer fibre of random transverse index distribution, figure 6.6, approached that of an equivalent semi-random glass fibre. They randomly stacked rods of the high index polymer polystyrene (PS) and low index poly-(methylmethacrylate) (PMMA), and drew this to fibre. This work, as well as the experimental and theoretical results of many other groups, is discussed in Arash Mafi’s excellent summary of the topic, “Transverse Anderson localization of light : a tutorial”, published in a 2015 edition of *Advances in Optics and Photonics* [101]. At that point the only random air-silica fibres to be produced had poor performance due to a very low filling fraction of air.

All this work has culminated in a paper published in 2018 *Scientific Reports*, by Zhao *et al.*, in which they present an air-silica fibre with high enough air filling fraction to establish effective imaging [102].

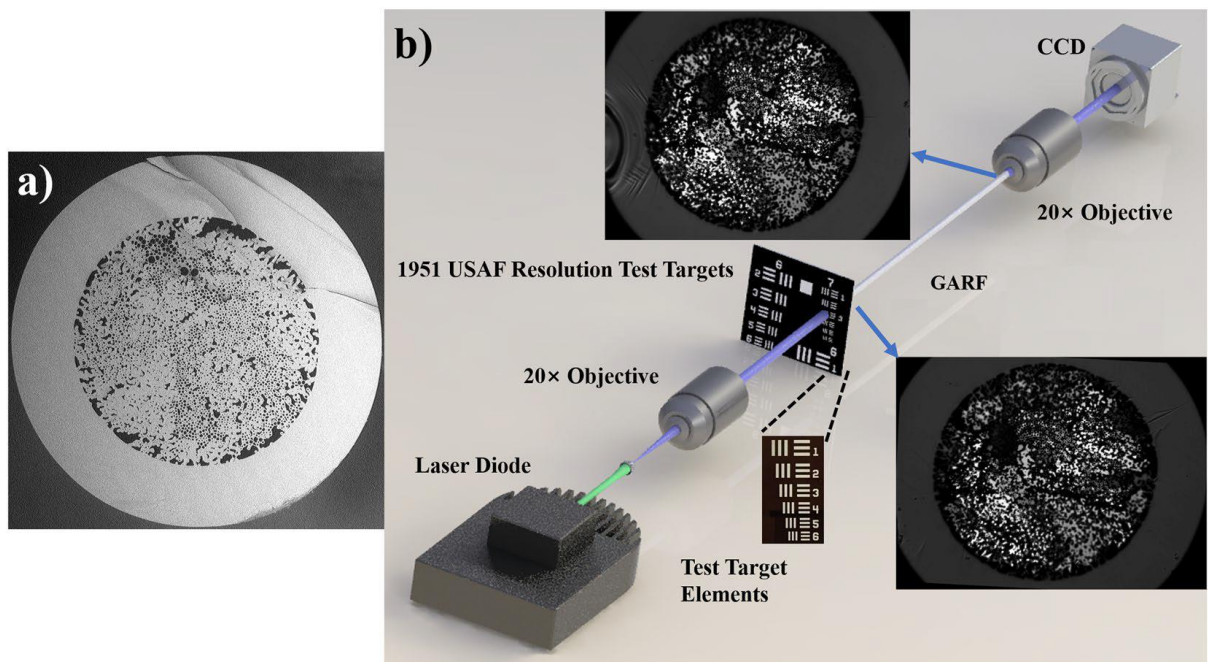


Figure 6.7: The glass-air random fibre (GARF) [102].

Shown in figure 6.7, the Glass-Air Random Fibre (GARF) was fabricated by randomly stacking thousands of silica capillaries of different inner and outer diameters within a jacket tube, and drawing down to fibre.

They extensively study the quality of transmitted USAF test target images using both the mean square error (MSE) and mean structural similarity index (MSSIM) as quantitative measures of the difference before and after their GARF and Fujikura’s FIGH-10-500N for comparison. According to their analysis, both the commercial fibre and a 90 cm length of GARF are capable of resolving features as small as 18 and 22 μm using 405 and 635 nm illumination, respectively. This

contradicts the results provided by other groups that show the FIGH-10-500N can resolve features smaller than $10\ \mu\text{m}$ at $768\ \text{nm}$ [66]. This is likely because the authors have chosen to focus on larger resolution features that the GARF is capable of imaging, and because their numerical methods interpret the lower contrast images obtained using the FIGH-10-500N to be of lower quality. It is also worth noting that the minimum bend radius they have used was $20\ \text{cm}$, far too large for many medical endoscopy applications, and many of their measurements were conducted with $4.5\ \text{cm}$ pieces of straight GARF.

6.2.5 Air-polymer microstructured fibre

In 2004 M. A. van Eijkelenborg published a paper in *Optics Express* describing a PMMA optical fibre with an air-hole lattice microstructure for light guidance and imaging, shown in figure 6.8. They demonstrate image guidance using both the 112 holes and the 89 solid interstitial cores, but with so few cores the images are crude and have a minimum resolution of $42\ \mu\text{m}$ due to the hole spacing. Considering the prohibitively large $800\ \mu\text{m}$ outer diameter, this is a far cry from the performance of doped silica fibres of the same diameter, but it does have the advantage of a very small minimum bend radius of $3\ \text{mm}$ due to its material. Although a $250\ \mu\text{m}$ OD fibre is also mentioned, and they claim to have achieved similar results with it, no evidence to this effect is provided. It is also stated that useful lengths are limited to less than a meter by excessive loss.

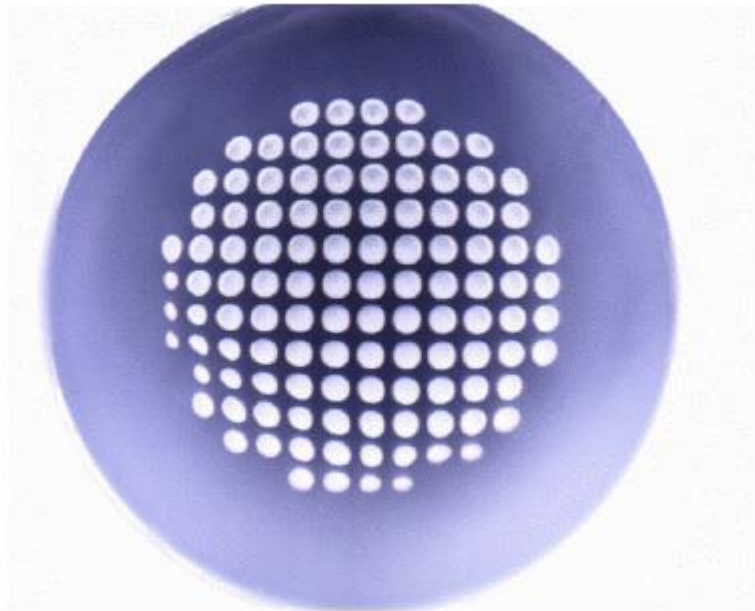


Figure 6.8: The microstructured PMMA imaging fibre from [103], with $800\ \mu\text{m}$ outer diameter and $42\ \mu\text{m}$ hole spacing.

6.2.6 Superlattice microstructured optical fibre

In 2014 Tse *et al.* published an article in *Materials* describing their superlattice fibre, figure 6.9, and their three-stage stack-and-draw fabrication technique. Although this work was unknown to me at the time of fabricating the fibres discussed later in the chapter, the fabrication techniques are similar; both involve a primary sublattice stacking stage of capillaries and solid glass canes, and drawing this down without a jacket to produce canes for the secondary, superlattice stack. Their goal in this case was to produce a highly birefringent PCF, in which they succeeded.

To my knowledge, this is the only published case of multi-stacking that involves drawing down unjacketed capillary-cane stacks. The sublattice stack includes a full layer of solid canes surrounding the capillaries, which should provide good structural strength during the first drawing stage.

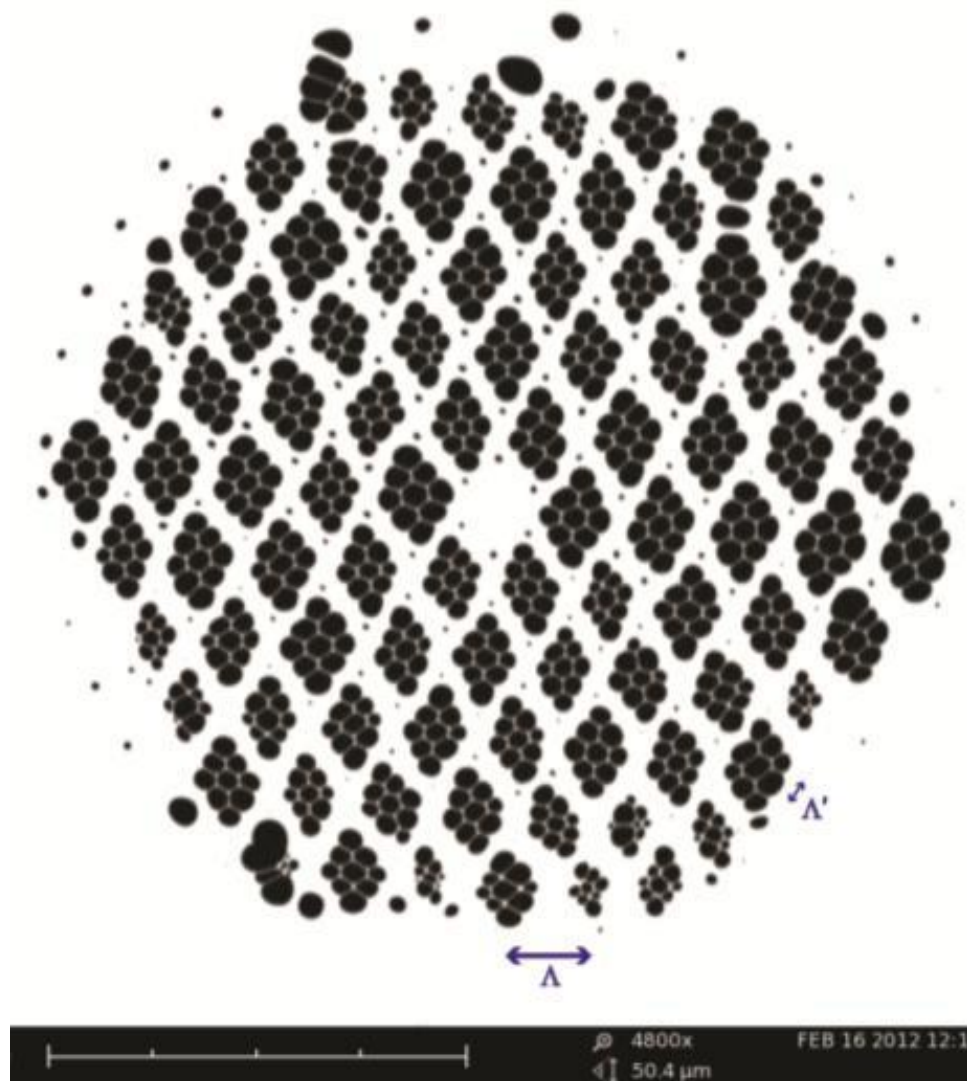


Figure 6.9: The superlattice microstructured optical fibre from [104].

6.3 PCF imaging fibre

Midway through Proteus' Panoptes work package in 2016, Dr. Jim Stone began work on his "air-clad" imaging fibre. His fabrication process consisted of two stages: In the first he fabricated a fibre with a single core inside a capillary cladding. In the second stage he fabricated the imaging fibre by bundling thousands of the air clad core fibres.

The first stage was commenced by stacking 8 fine capillaries around a central solid silica rod and inserting the stack into a thin outer jacket to keep the structure together. This was drawn to fibre using the standard, actively pressurised PCF fabrication techniques described in chapter 2. One change to the fabrication was made; no polymer coating was applied. This produced over 1000 m of the bare 400 μm fibre shown in figure 6.10.

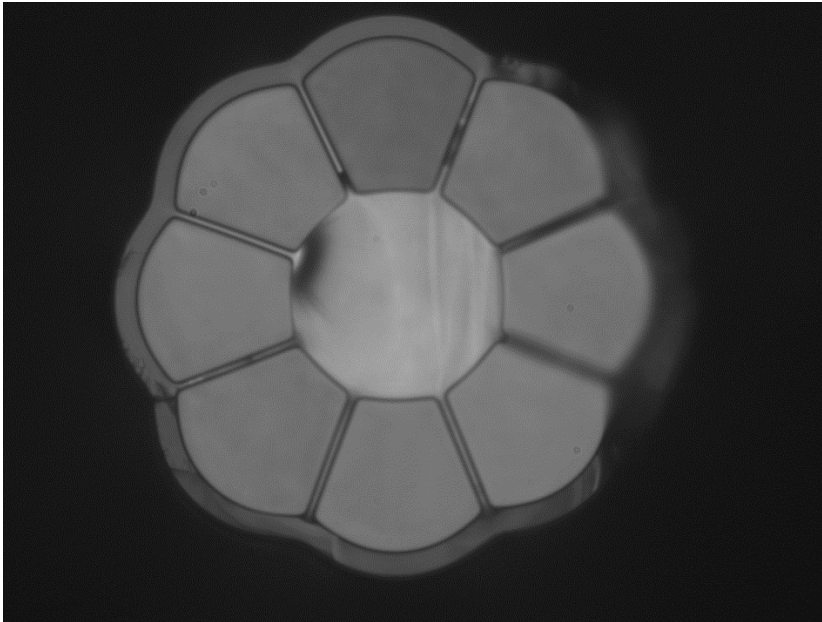


Figure 6.10: The cross section of one of Dr. Jim Stone's 400 μm air-clad core fibres.

With the fibres wound onto a 1 m circumference drum a perpendicular strip of masking tape was used to secure them, and a cut was made below it, separating the fibre into 1000×1 m long strands. These were hung using the tape to allow anti-static devices to remove any surface charge that had been built up during fabrication before they were bundled together and inserted into a jacketing tube for a secondary drawing stage.

This bundle was drawn down using the same standard PCF techniques, producing the fibre shown in figure 6.11, where each of the first stage fibres forms a core within its own set of air cladding capillaries.

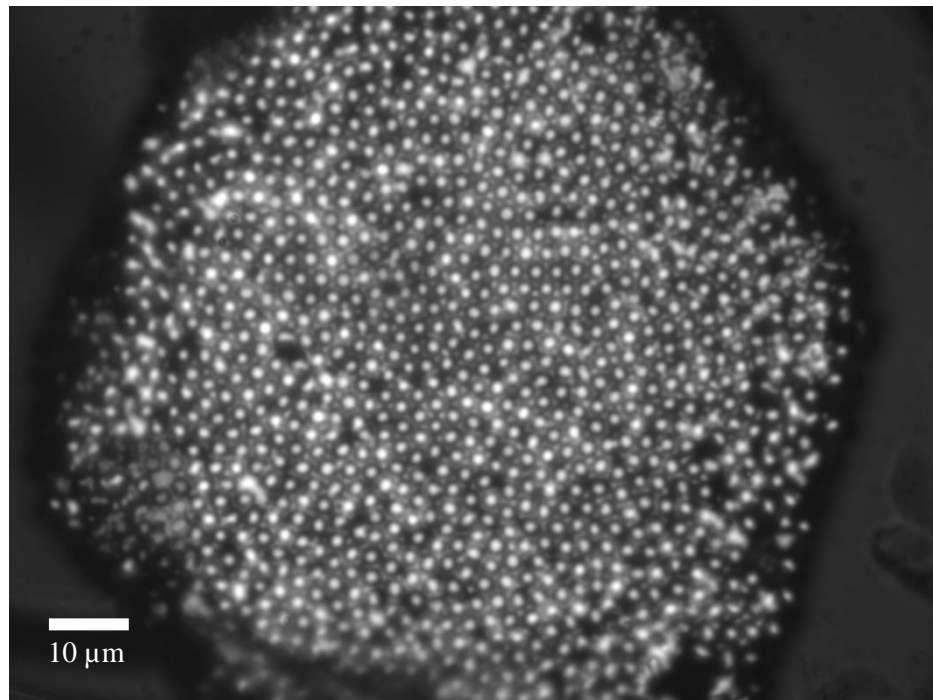


Figure 6.11: An optical microscope image of Dr. Jim Stone's first air-clad fibre.

Figure 6.12 shows Jim's air clad fibre transmitting images of a copper mesh SEM calibration target, compared to images taken using Fujikura's FIGH-30-650S. Although the field of view is small and patchy, the image quality was approaching that of the FIGH-30-650S at wavelengths around 550 nm, but showed great promise past 950 nm as very little crosstalk is observed in the air clad fibre. The main optical issue that reduced performance at short wavelengths was the presence of cladding modes that blurred details finer than around 15 μm .

There were also several issues with the fabrication of this early design: Breakages while drawing the single-core fibre were common due to the lack of coating to protect from the mechanical stresses involved with going around the various belts and wheels. The act of inserting the core fibres into the jacket tube was also fraught with difficulty as the fibres were not only fragile, but easily built up a static charge because of their large surface area. This project was then set aside because of the frustratingly high failure rate of this step, and the resulting concerns around scaling up the number of cores in the structure.

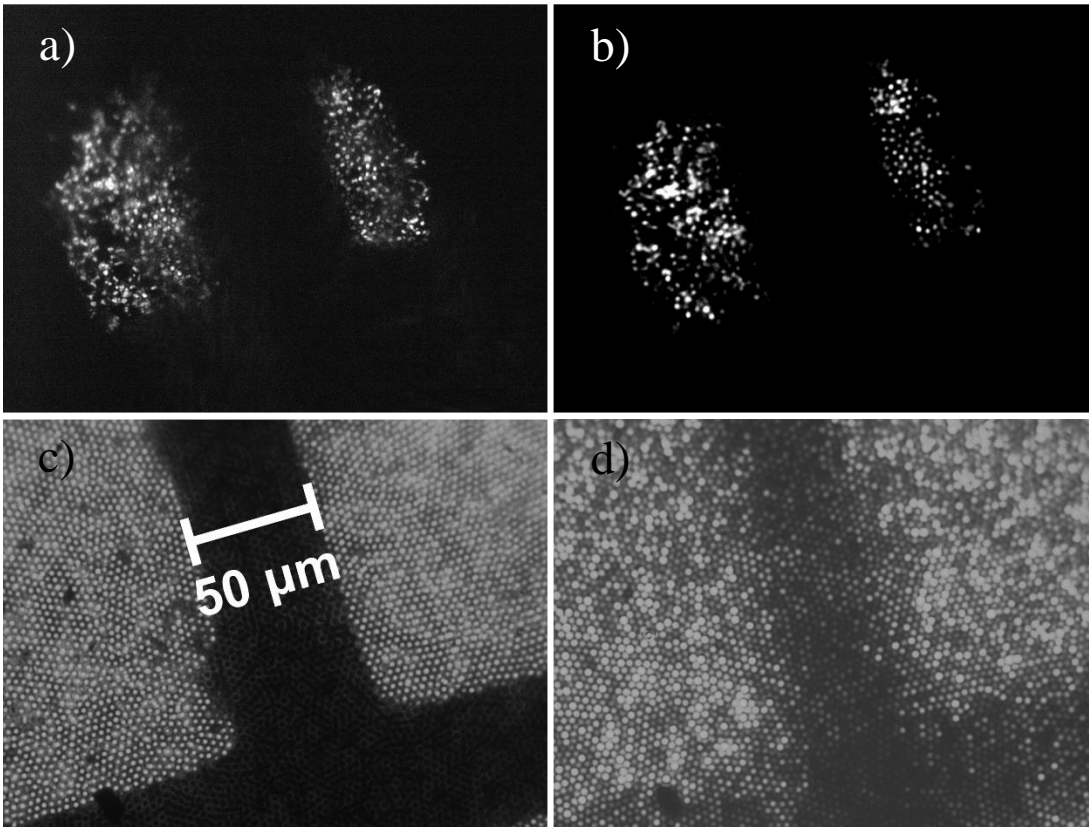


Figure 6.12: images of a copper SEM calibration target, taken using Jim's air clad imaging fibre (a, b) and the FIGH-30-650S (c, d). In (a, c) 550 nm light was used, and 950 nm in (b, d).

6.4 Air clad imaging - ACI1

At this point I reached a natural pause in my work after having published the paper on my quantitative characterisation technique, detailed in chapter 5, so I adopted the air-clad imaging fibre project as my own. In this and the following sections I will provide an account of this idea's evolution, as well as detailed instructions on how to produce these fibres. As with the imaging fibres in chapter 4, all results of characterising my fibres in this chapter were obtained using approximately 1-meter lengths of the fibre unless stated otherwise.

6.4.1 Fabrication

Confident that the key to raising the number of cores lay in multi-stacking techniques like those used to produce our solid fibres, I began by designing the stack shown in figure 6.13.

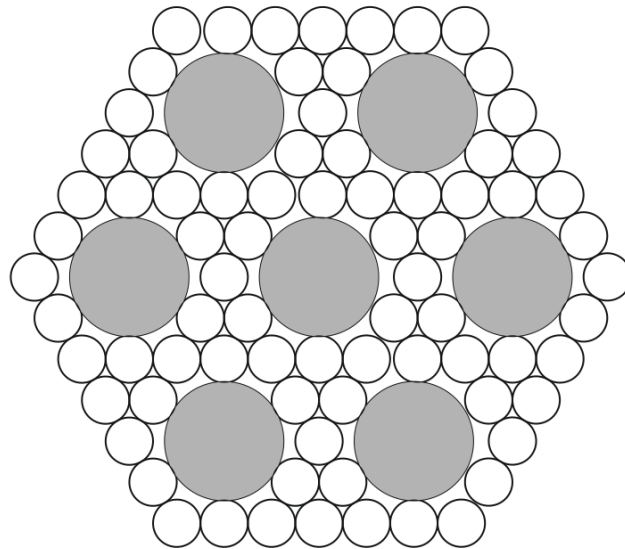


Figure 6.13: The design for the initial stack of ACII. The grey circles represent solid silica, and the white circles capillaries.

I began work by drawing down a 20 mm solid silica rod to 5 mm canes to make the cores. A 19.8/21 mm OD/ID silica tube was drawn to 2 mm to form the cladding capillaries. The stack in figure 6.13 was bound together on the jig using PTFE tape and drawn down to 1.26 mm canes, removing each piece of tape as it approached the furnace. As with the hexagonal canes fabricated for our solid imaging fibres, care needed to be taken during the start of the draw to avoid twisting the canes. In addition to this, at these scales the force of surface tension dominates and can easily cause the capillaries (particularly the outer ones) to collapse at high drawing temperatures. At low temperatures, however, they can crack due to the force exerted on them by the pulling belts. For this reason, I began at high furnace temperature as the collapsed structure is less prone to cracking. Once the draw had reached steady state, the temperature was gradually decreased and regular samples of the cane were taken until the structure looked like figure 6.14. In this case the furnace temperature was 1850°C.

During this process the belt pressure should be monitored closely to avoid crushing the outer capillaries, or slipping on the glass as the change in the draw rate causes bulges at furnace which will crack in the belts. If breaking does occur, the belts must be cleaned thoroughly to avoid debris causing cracks in subsequent attempts. Once the fluctuations in cane thickness are less than 25 μm they can be collected.

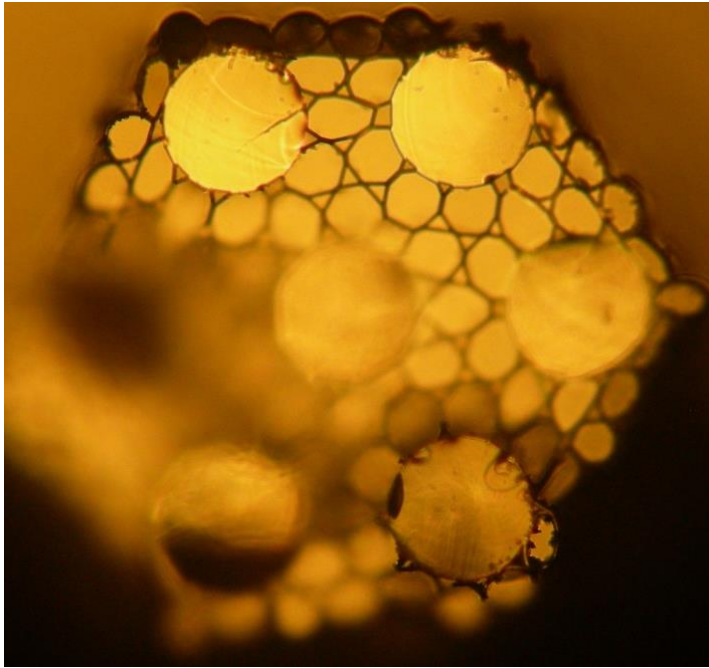


Figure 6.14: A first stage cane from ACI1. Cleaving is challenging due to the strength of the cores compared to the fine capillary cladding, causing the out of focus regions.

I made a stack of 169 of the 7 core canes and packed it into a jacket tube. I drew this down to 4.3 mm OD canes using the passively pressurised PCF technique, which I then drew to the desired fibre diameter; 200 μm in the case of figure 6.15.

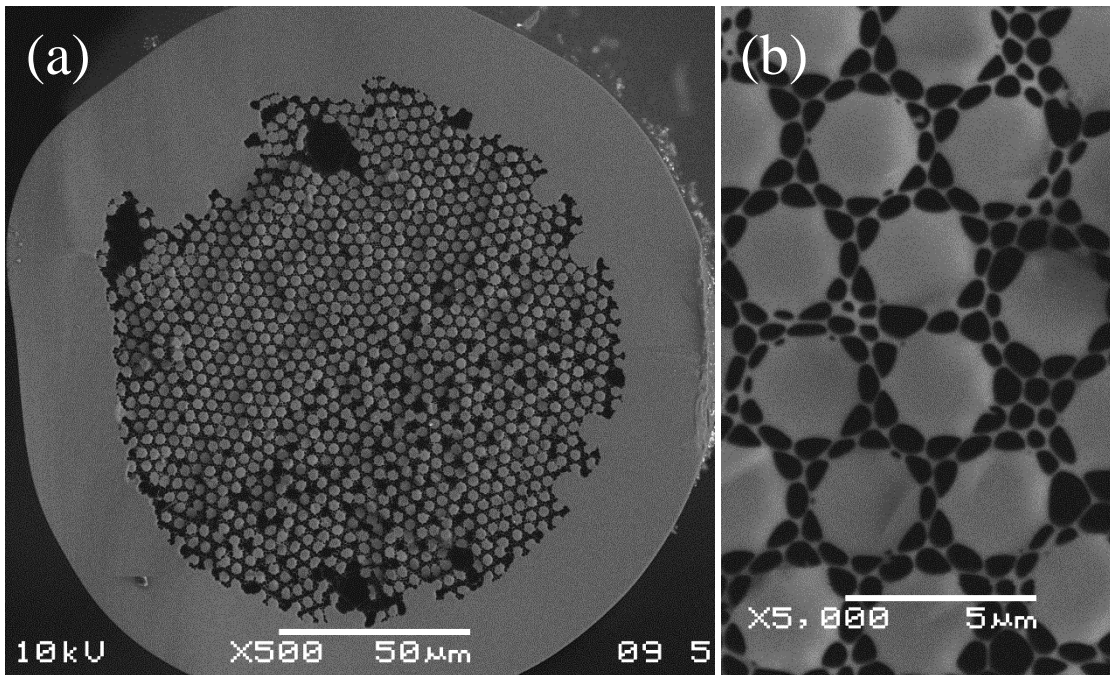


Figure 6.15: SEM images of a stub of 200 μm OD ACI1 fibre.

In both the secondary cane and final fibre stages I use the same temperature monitoring procedures as in the first stage; starting at high temperature and decreasing until the desired structure is observed, but it is far more easily achieved in these stages due to the structural strength afforded by the thickness of the outer jacket glass.

Figure 6.15 (a) shows one of the characteristic complications of this type of fibre – uneven cleaving. This is because the structure of the capillaries is so fine that imperfections can shift the course of a propagating cleave before it reaches the next core, causing it to be cleaved slightly higher or lower than the previous one.

6.4.2 Characterisation

Figure 6.16 compares images of element 1 of group 6 (7.81 μm) of a USAF test target taken using ACI1 and the FIGH-30-650S using 850 nm light. The field of view of ACI1 is very small, but despite this and the structural imperfections, its image is clearer than the one from the FIGH-30-650S, and the resolution higher than the previous air-clad fibre.

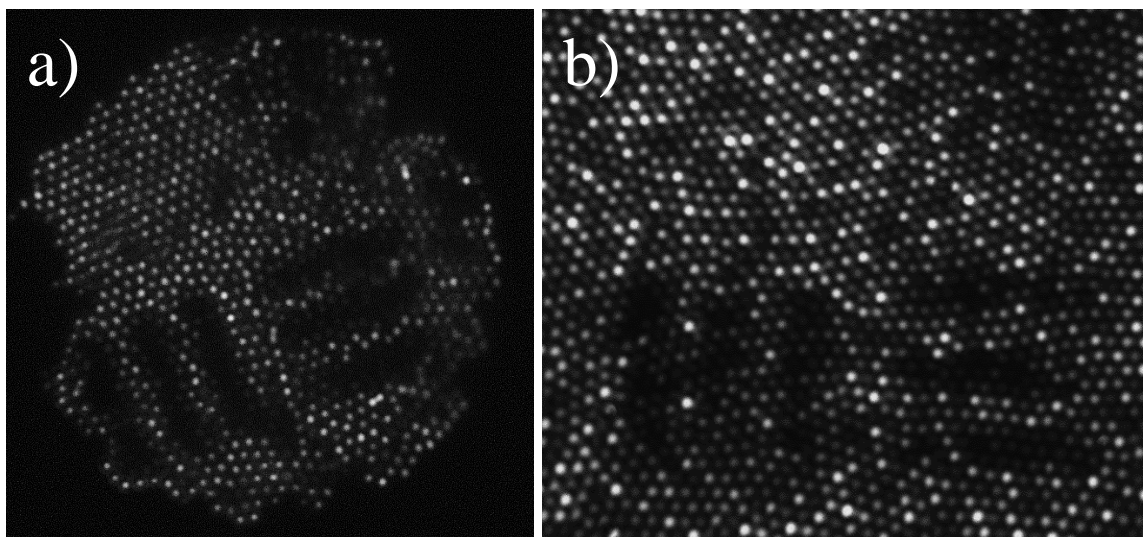


Figure 6.16: a) an image of element 1 of group 6 of a USAF resolution test target using 1 meter of ACI1. b) an image of the same element using Fujikura's FIGH-30-650S with the region corresponding to the left image circled. Both images were taken using 850 nm light.

6.5 ACI2

6.5.1 Fabrication

Having obtained a proof of concept that this type of fibre was possible, with ACI2 I aimed to scale up the number of cores using a primary stack with 42 solid cores (the design in figure 6.17) and a secondary stack of 217 of these, producing a 9114 core fibre.

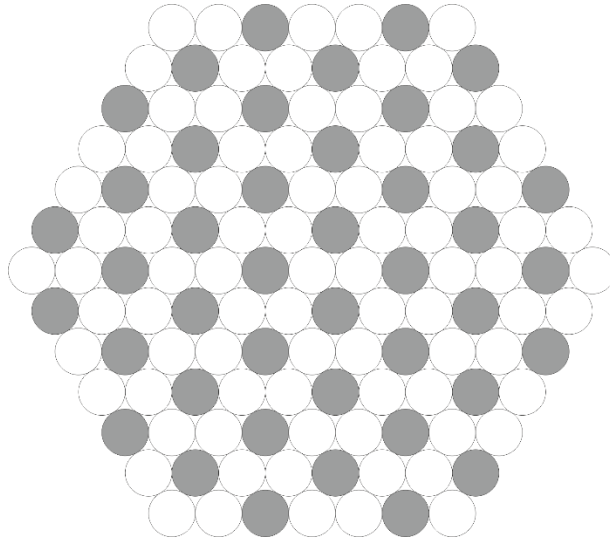


Figure 6.17: a schematic diagram of the primary stack that forms the sublattice of ACI2.

I hoped that by having solid canes within the outer boundary of this stack I could achieve higher core numbers more easily, and test if it is possible to precisely orient the canes in the second stage stack so that cores do not end up side-by-side.

The fine structure of the primary stack canes made it difficult to control their thickness accurately, so many had fluctuations too large to fit neatly in the second stack. In addition, partly because of the size variations, and partly because the cane stub I used to arrange the canes on the stacking jig had sharp corners, many capillaries cracked during the secondary stacking process. As the first few canes to fracture produced a fine glass dust the packers jammed and grinded against their neighbours when inserted, producing more glass fragments that exacerbated the problem.

Nevertheless, I drew this preform to canes and then the 200 μm fibre in figure 6.18, showing that despite the cracks in the capillaries, most of the internal capillaries in the sublattice remained open. It is possible that because they are so thin and close together at the final cane stage, heat from the furnace seals any cracks and holes against neighbouring capillaries, or that some do collapse, but the void is simply filled by the expanding, intact neighbour capillaries.

Efforts to stack the sublattice canes so that no edge cores are side-by-side failed partly due to the damaged capillaries and also because movements of the canes at the scale of the cores was very difficult to avoid. Although Anderson Localisation did help minimise the damage to the imaging quality, it was hampered by the merged cores at the borders of each sublattice stack.

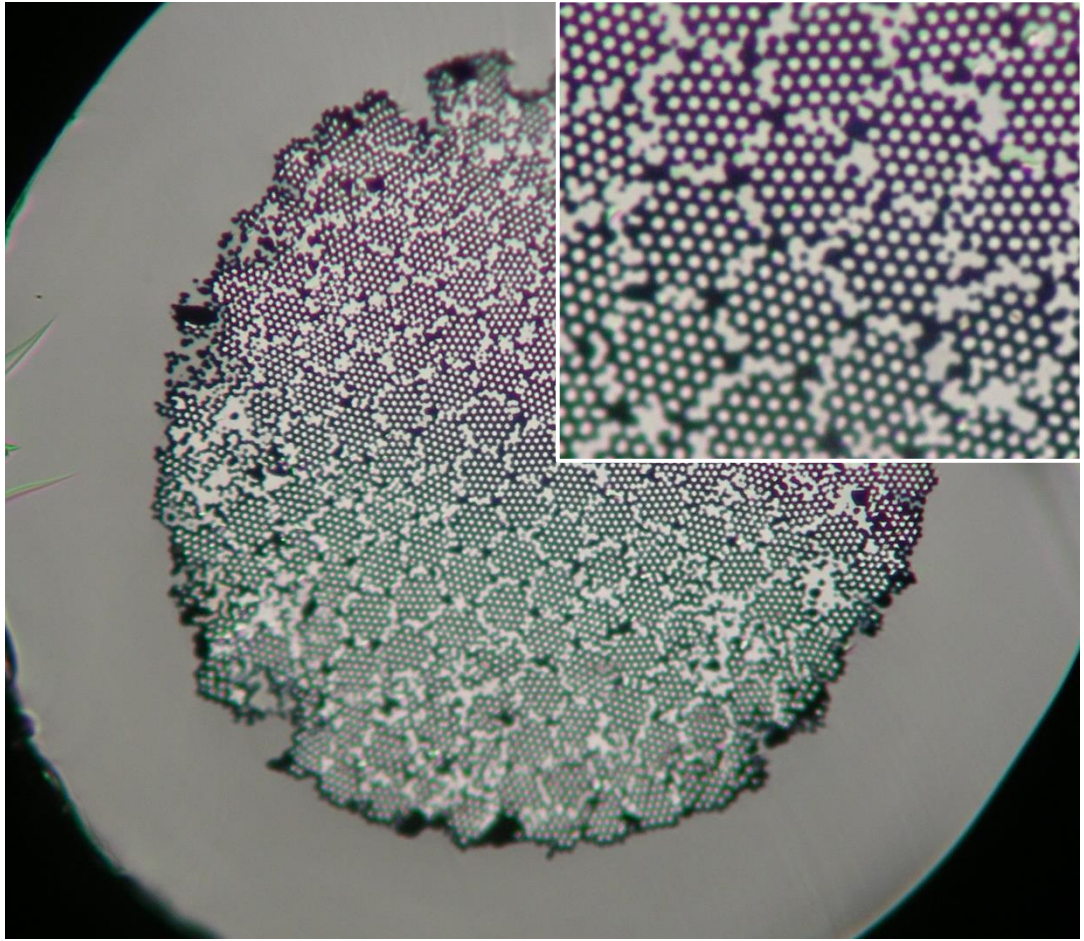


Figure 6.18: The 200 μm diameter ACI2 fibre under an optical microscope.

6.7 ACI4

Hoping to solve the issue of merged cores at the edges of the primary stacks, my third fibre design included a full layer of capillaries around the primary stack, so that there was a double layer between the edge cores of any given stack and its neighbours. Although the capillary layer worked as intended, I failed to properly stack the second stage. This resulted in a fibre that functioned reasonably well, but with very patchy quality. Although it did not meet the standard I had hoped for publication, I was confident that, with some refinement, this design could produce a fibre that would.

I began work on the fourth iteration of the air-clad imaging fibres using a similar design and fabrication process to the third, but with two improvements: The first was to reduce discontinuities in the structure by improving the techniques used in the secondary stacking stage – discussed in the following section. Second, I intended to further reduce coupling by using the 3 germanium-doped step-index preforms left over from the early Panoptes imaging fibre prototypes as the cores of ACI4, arranged as with my hexagonal fibres in chapter 4. The doped inner cores were far too small in the final fibre to guide light themselves. Instead, the modes were still guided by the air-silica index step,

and the germanium dopant served to introduce slight differences to the effective refractive indices of neighbouring cores, thereby giving them different propagation constants and reducing coupling. This version was successful enough to warrant both a paper and a patent application [105].

6.7.1 Fabrication

To build up the sublattice stack I drew the doped preforms and the 23.2/25 mm tubes to 1.85 mm OD, and assembled 57 core canes and 160 capillaries as shown in figure 6.19 (a). Note that, as mentioned in the previous section, the external layer consists only of capillaries so that the cores are guaranteed to be kept separate in subsequent stacks. I drew this stack down at 1900 °C to 1.2 mm thick canes as in figure 6.20 and made a stack of 217 of these. Next, I carefully pulled 3 canes out from each corner in 10 cm stages to allow 10 evenly spaced loops of PTFE tape secure the structure. Rounding the stack like this means the canes have far less room to move out of position once inserted into the 19/25 mm silica jacket tube. The PTFE was removed one band at a time as the stack slid inside. With one band of PTFE remaining on the end of the stack, I packed the small edge spaces with 0.9 mm silica canes to produce the preform shown diagrammatically in figure 6.19 (b).

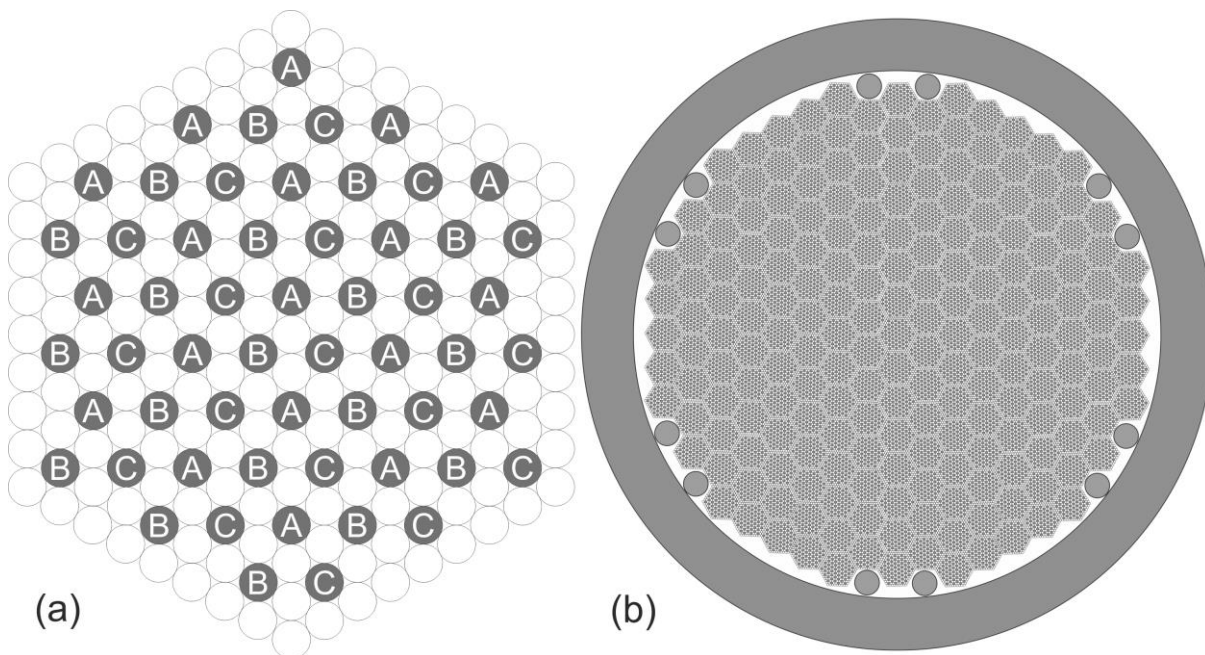


Figure 6.19: Schematic diagrams of the two main stages of fabrication. Shaded regions are silica glass and unshaded circles hollow capillaries. (a) depicts the first stacking stage with 57 cores, and the arrangement of the three different inner core sizes indicated by the letters A,B, and C. Note that the outer layer is comprised of capillaries only so that cores are separated in subsequent stacks. (b) shows an example final preform structure containing the canes produced from the first stack within an outer jacket tube and some solid silica packing canes at the edges to maintain the structure.

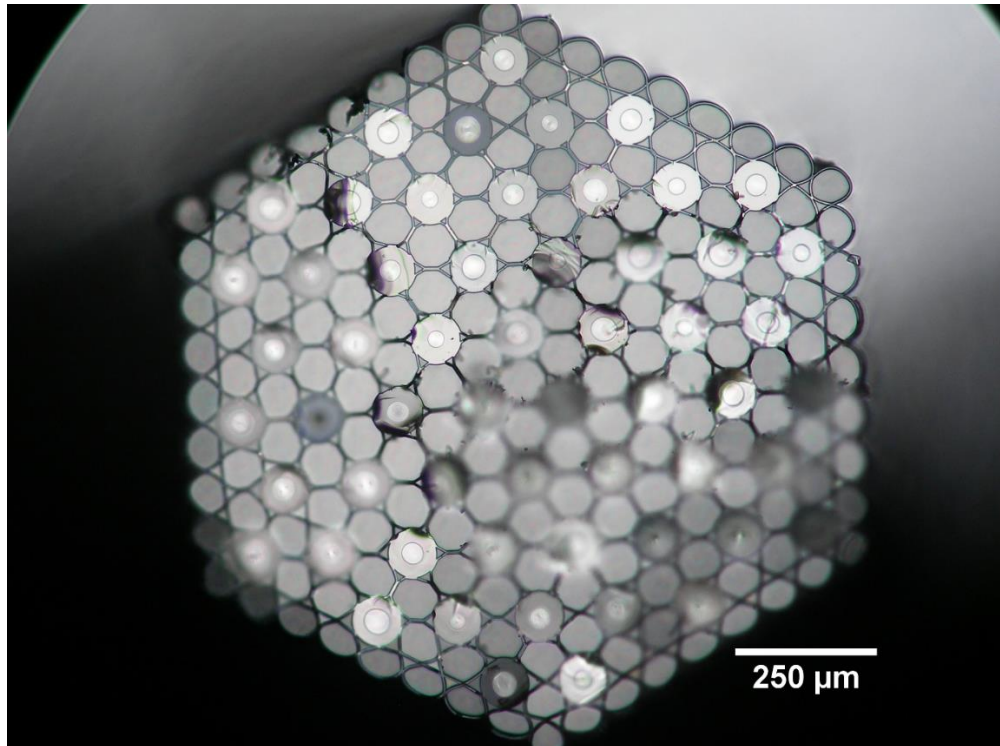


Figure 6.20: The cross section of a sublattice cane for ACI4, illuminated in transmission to better see the doped inner cores.

Drawing this to 4.3 mm OD canes at 1990 °C and then to 535 μm OD fibre at 1940 °C (6.47 N tension on the glass during the draw) produced the structure in figure 6.21. At some point (most likely when the stack was inserted into the jacket tube) a section of the structure shuffled one or two core widths out of place, producing a discontinuity in the lattice. Nevertheless, this was the most perfect stack achieved thus far.

This size of fibre was chosen as it has the same core spacing as Fujikura's FIGH-30-650S (3.2 μm separation and 2 μm core diameter), allowing the effects of differing resolutions to be removed from the list of variables during their comparison.

A second cane was also drawn to 353 μm to allow the possibility of high resolution, short wavelength imaging to be investigated. Despite the additional time for finding the correct tower parameters that is afforded by the steeper draw down ratio, the thinner air-clad fibres were very difficult to keep inflated as surface tension forces dominate at such small capillary sizes.

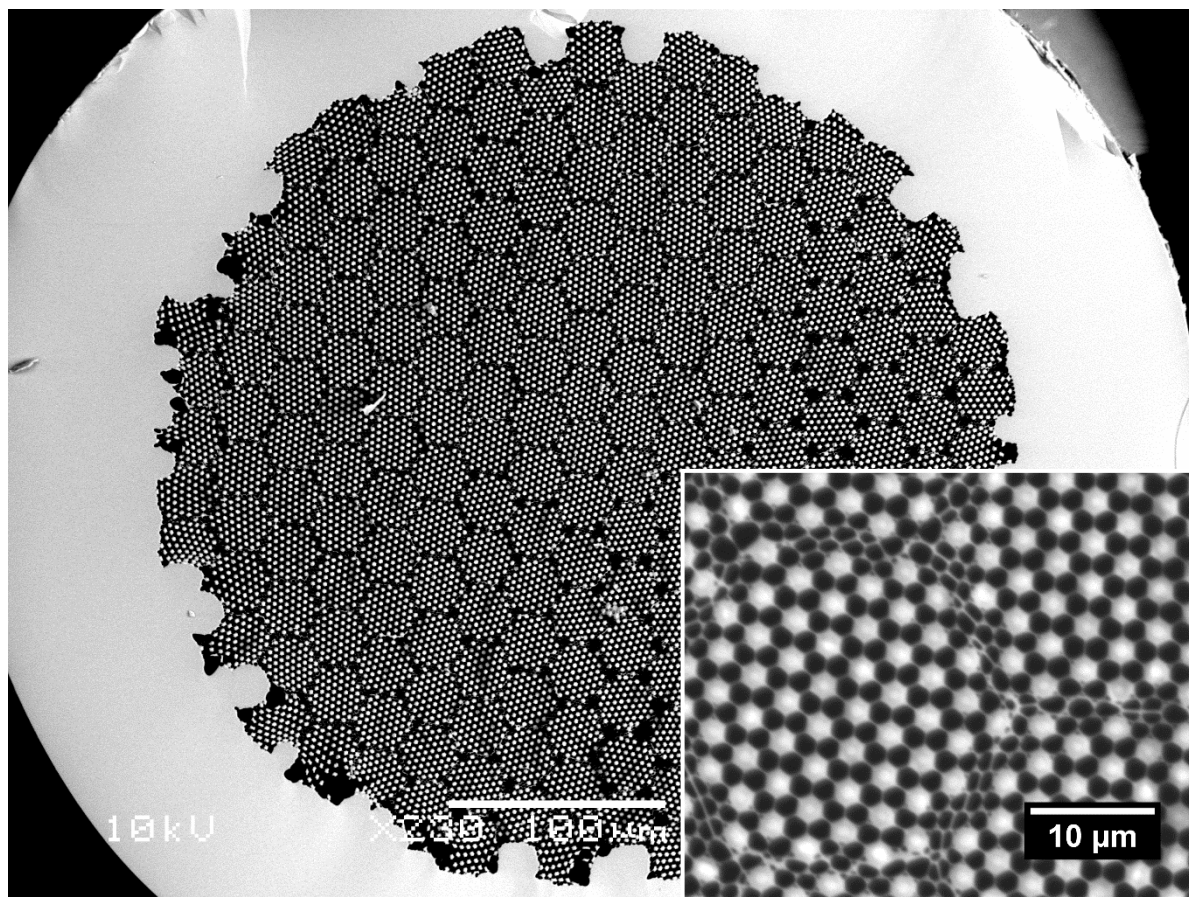


Figure 6.21: The 535 μm diameter ACI4 fibre. The dopant inside the cores can just be seen in the inset.

6.7.2 Characterisation

These were the first air-clad fibres with the potential to surpass the performance of all previous solid fibres in terms of functional wavelength range, number of cores, and resolution, so extensive qualitative and quantitative imaging characterisation was called for. As an entirely new type of fibre, the numerical aperture and dispersion of the cores were also unknown, warranting further investigation compared to our previous fibres. All of this is detailed and discussed in this section.

6.7.2.1 USAF test target imaging

Again, the process began with USAF test target images, and comparison with those using the FIGH-30-650S.

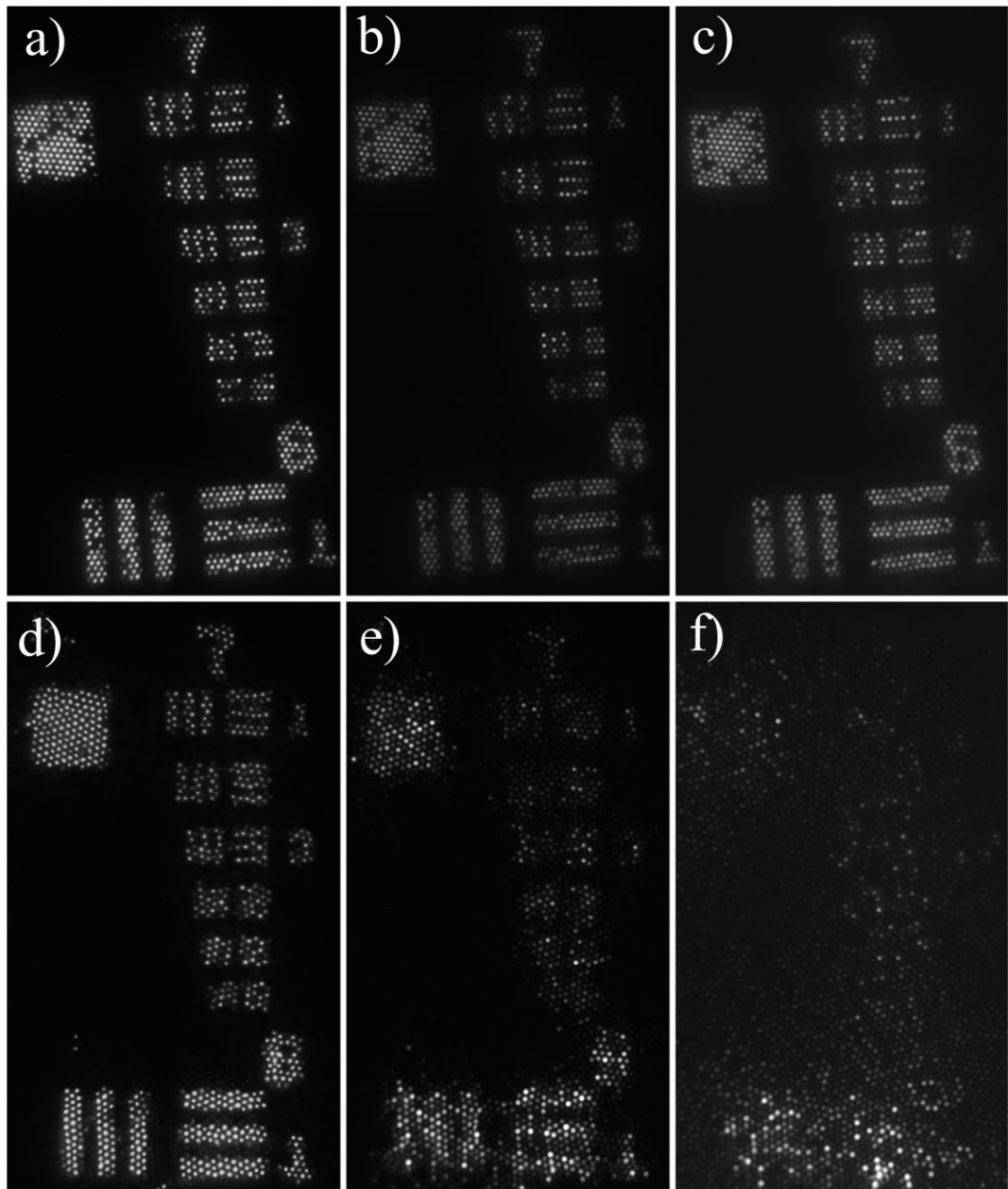


Figure 6.22: A series of group 7 USAF resolution test target images using the 535 μm diameter air-clad fibre (a-c) and the FIGH-30-650S (d-f). The light source was a supercontinuum that was band-pass filtered to 500 nm (a, d), 850 nm (b, e), and 1000 nm (c, f).

Figure 6.22 makes the potential of these air clad structures clear. The dramatic drop in performance of the FIGH-30-650S past 850 nm is apparent, but in stark contrast to the images produced by ACI4 which remain almost unchanged up to the limit of the silicon CCD's spectral range. At 1000 nm a drop in ACI4's performance is evident as element 3 of group 7 can no longer be distinguished, but this is a far more gradual increase in crosstalk with wavelength than is seen in any solid imaging fibre investigated during this project. Seeing that the fibre suffers little coupling

at the long wavelength limit of the silicon CCD prompted further study, so I used an InGaAs short wave infra-red (SWIR) camera to produce the image in figure 6.23.

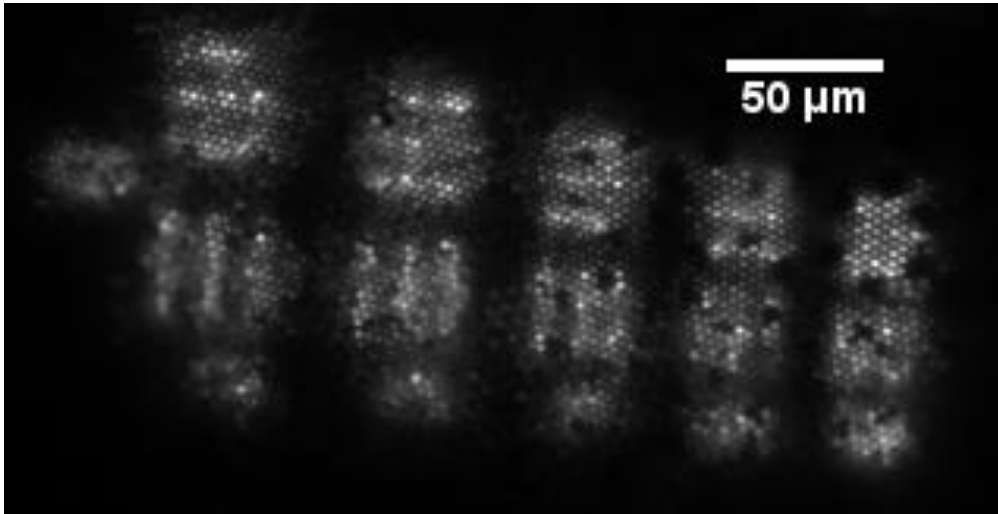


Figure 6.23: An image of group 6 taken using the 535 μm ACI4 at 1600 nm.

It is not until 1600 nm is reached that group 6 becomes difficult to resolve, past which the SWIR camera's spectral response is insufficient to continue the experiment. To investigate at what wavelength the performance of these fibres breaks down entirely I used the 353 μm fibre to scale the experiment down by a factor of $2/3$, to wavelengths where our detectors function. This also allowed me to test its high-resolution functionality.

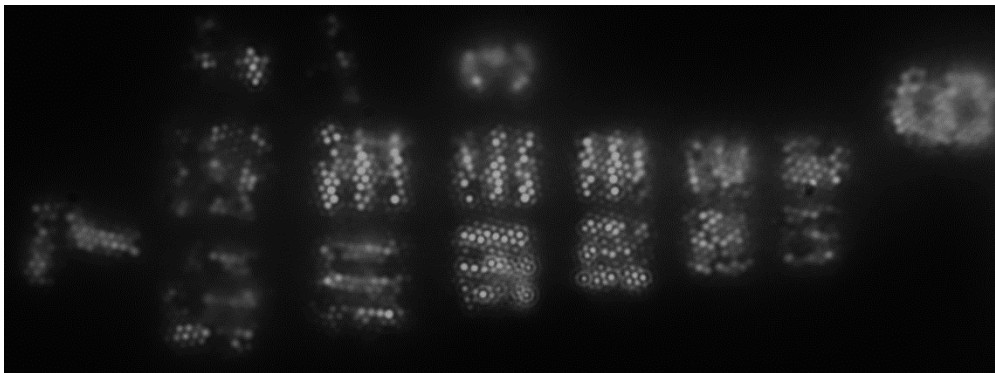


Figure 6.24: An image of group 7 of a USAF target taken using 700 nm light and the 353 μm version of ACI4.

As discussed in chapter 4, the V number (or normalised frequency) of a core gives a good indication of how well the mode is confined to the core. Equation 12 of chapter 2 indicates that V should scale linearly with the core diameters, leading to the conclusion that changing a fibre's scale should linearly shift its performance profile to a different wavelength. Because of this, I had expected that the 353 μm fibre would produce images at 700 nm of similar quality to those from the 535 μm

version using 1000 nm light. Comparing figure 6.24 and figure 6.22 shows that the 353 μm fibre performs far worse than expected, with significant crosstalk at only 700 nm. This is likely because the slight collapse of the cladding capillaries mentioned towards the end of section 6.7.1 decreases the core separation. Nonetheless, the USAF test target image in figure 6.25 makes a good case for the thinner version's high-resolution functionality at 500 nm.



Figure 6.25: An image of group 7 of a USAF test target taken using the high resolution 335 μm outer diameter air-clad fiber and a 500 nm bandpass filter. A scale bar and an identifier for element 6 have been added.

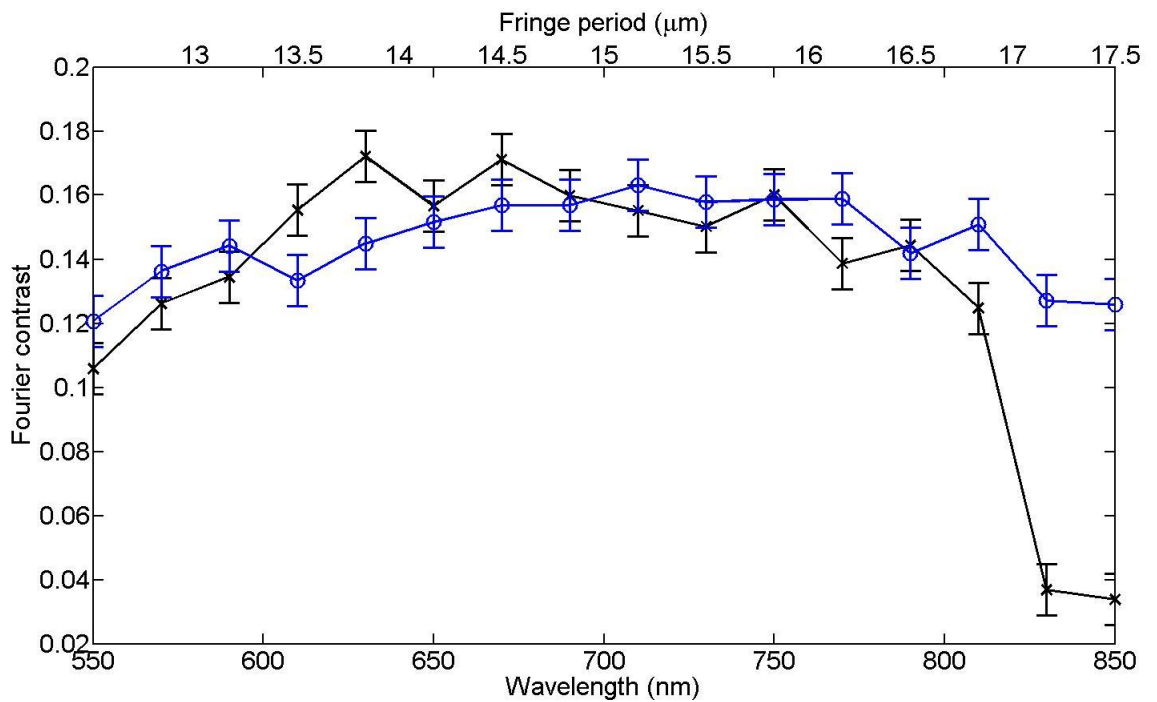


Figure 6.26: A plot of the Fourier contrast of fringe images through the 535 μm ACI4 fibre (blue circles) and the FIGH-30-650S for comparison (black crosses).

6.7.2.2 Quantitative characterisation

I used the interferometric characterisation technique discussed in chapter 5 to produce figure 6.26, showing that ACI4 has comparable contrast performance to FIGH-30-650S at wavelengths lower than 800 nm, and far better performance past 830 nm.

6.7.2.3 Numerical aperture

Using the knife-edge measurement technique discussed in chapter 2, I determined the wavelength dependence of the NA of ACI4's cores. This procedure was challenging due to the multi-mode nature of the cores, as well as the difficulty ensuring that only one had been coupled into. For this purpose, I used a camera and flip-mirror to image the output of the cores. Guaranteeing a flat end face was also very difficult, but necessary to ensure that the angles of emission are as expected for a flat fibre end face; equal to both sides of the fibre's axis. By taking the edge of the profile to be at 10% of maximum power, the NA was 0.41 ± 0.05 and 0.44 ± 0.05 at 500 and 1000 nm respectively. There are two competing effects at work here: On the one hand, the refractive index of silica is lower for longer wavelengths, so one might expect the NA to decrease with wavelength. On the other, longer wavelengths diffract through small apertures, such as the end of a fibre core, more. In this case, because the cores are little more than a couple of wavelengths wide at 1000 nm, the NA seems to increase with longer wavelength.

6.7.2.4 Dispersion

In an effort to quantify the difference between the three families of cores in the fibre and its significance to the low coupling observed, I used the dispersion measurement techniques described in chapter 2 to look for the differences in the propagation constants of each core family. I began by analysing the three core types by coupling the supercontinuum into one at a time. This yielded the data shown in figure 6.27.

The peaks seen are interference fringes indicating that the delay stage's position has matched the optical delay of the light in the experiment's fibre arm and the delay arm. The fact that evidence of each of the 3 interference peaks can be seen at roughly the same stage position in each trace shows that core crosstalk is occurring, but it is also reassuring evidence that we are observing the effects of the three differently doped core families. Interference peaks at greater stage positions indicate that the core's group delay is lower because the doped region is smaller. The peaks at 39.3 ± 0.1 and 39.7 ± 0.1 mm are therefore from the cores with bigger doped regions than the ones producing peaks at 40.5 mm. Closer inspection reveals that the peaks from the large and middle doped core size are more closely spaced than the middle and small ones. This is indicative of the relationship between the core diameters discussed back in chapter 4: It was necessary to have the middle core size slightly

closer to that of the large core as the small one confines its modes less well and so suffers from increased coupling.

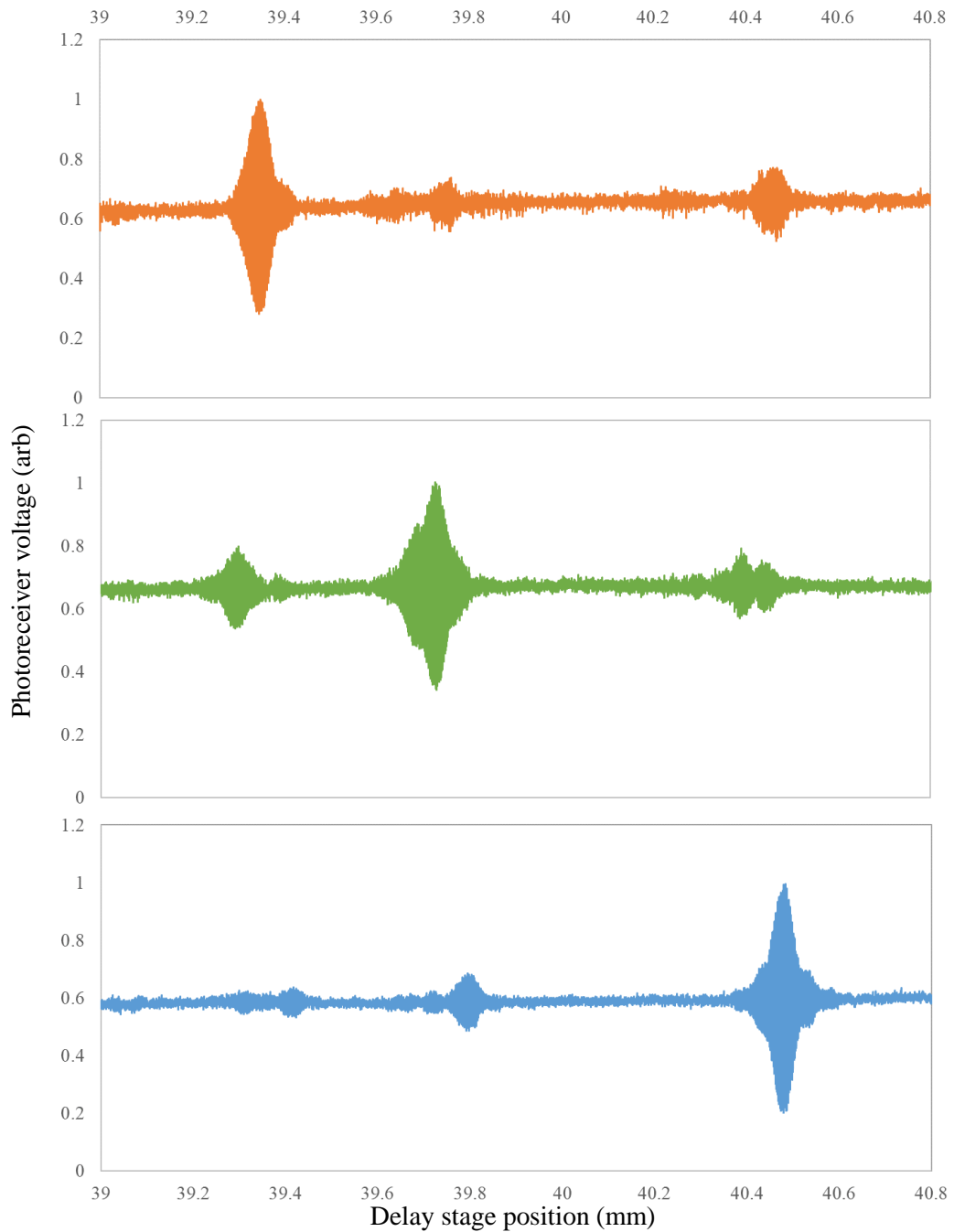


Figure 6.27: Normalised photoreceiver output voltage plotted against the delay stage position. Each trace represents a core from a different family being coupled into and analysed using a 900 nm bandpass filter. Larger stage positions indicate a smaller delay.

A different set of 3 cores were used to produce the group delay plots in figure 6.28. When changing wavelength, the beam coupling into the fibre would walk slightly due to the chromatic dispersion of the lenses. On 2 occasions this led to the wrong core being coupled into, producing the

outliers at 700 and 600 nm in the orange dataset. The anomalous result at 900 nm in the blue dataset is more difficult to explain, but could be a result of observing a cladding mode that can be guided in such a short and straight piece of fibre, or a supermode of a pair of cores where the separating capillary had collapsed.

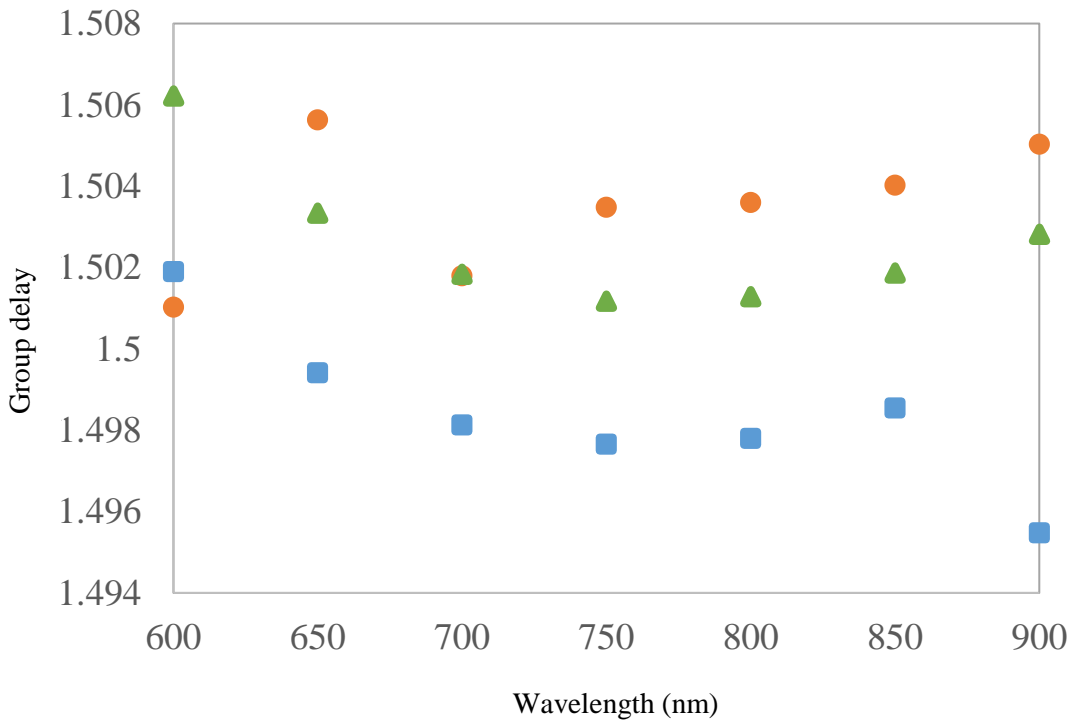


Figure 6.28: The group delays of 3 cores of a 5 cm length of 535 μm diameter ACI4 from each of the 3 different core families at a range of wavelengths.

In all three cases this data shows the expected, approximately quadratic, relationship between group delay and wavelength. The relative separation between each dataset is, again, indicative of the 3 different diameter doped regions.

6.7.2.5 Coupled family imaging

As seen in our early hexagonal solid core fibres, families of cores will light up when a single one is coupled into with high intensity light at wavelengths past its effective imaging range. As final confirmation of the effects that the doped cores in ACI4 have on its coupling characteristics, I imaged the result of coupling 1200 nm light into the 353 μm diameter fibre, producing figure 6.29.

Two things can be ascertained from this image; that the cores do indeed couple as families, and that the double layer capillary boundaries between the sublattice stacks are effective at confining crosstalk to a single sublattice unit.

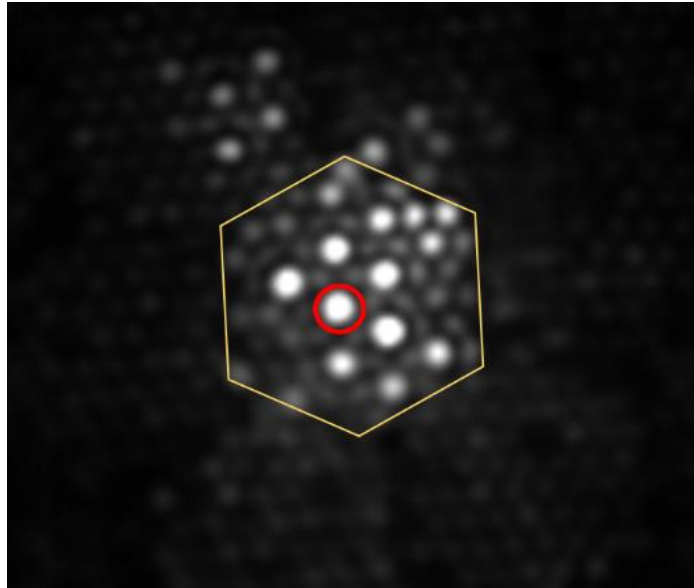


Figure 6.29: Near-field of the end face of a 1 m length of 353 μm OD ACI4 when coupling 1200 nm light into the core circled red. The yellow hexagon indicates the boundary of a sublattice stack.

Ultimately it was decided that this was the most distinctive proof that having three distinct core types has made a significant difference to the coupling characteristics, so, for the sake of brevity, only this evidence is included in the main paper [105].

6.8 Medical significance

Initial reactions might place all importance of these types of fibre on their implications for higher resolution endomicroscopy. What is potentially more interesting from a clinical perspective is the fibre's vast operational wavelength range, whilst maintaining the same resolution as commercial alternatives. This is because it presents the opportunity to multiplex signals from a far broader range of fluorescent probes, many of the newest of which operate in the near infra-red (NIR). This is a spectral region that is impossible to effectively image in with the current state of the art fibres that are used for bronchoscopy. Combining air-clad imaging fibre technology with clinically approved NIR fluorescent probes will provide clinicians with the ability to simultaneously observe the lung tissue using its green autofluorescence, and at least two distinct strains of bacteria, tagged with red and infrared fluorophores.

6.9 Post-processing

6.9.1 Necessity

In the context of the clinic, fibres with capillaries and unsealed end faces represent a health hazard as biological material can move inside the holes, leading to cross contamination between patients (discussed with respect to the hollow core sensing fibres in chapter 3). This is particularly problematic with air-clad imaging fibres as the thousands of micron scale capillaries soak up fluids like a sponge.

Air-clad fibres have the additional complication of being remarkably difficult to cleave flat, as discussed in section 6.4.1, which leads to poor imaging as it is difficult to bring all of the proximal end into focus at the same time. Using a ruby scribe to score the whole circumference of the fibre at the desired cleave position, wetting it with isopropyl alcohol, and applying tension, cleaves as flat as the one in figure 6.21 can be achieved. Although this is sufficient for the basic imaging experiments I have demonstrated, for a clinical product a perfectly flat end would be preferable.

Several potential methods of sealing the end face of the fibres were tested, details of which are in the next few subsections.

6.9.2 Tapering

We first looked to the taper rig as a means of sealing air-clad fibres. This was done using a particularly hot flame to collapse a short region, then a cleave was made as close to the end of the holes as possible to minimise the length over which the cores are close enough to couple together strongly. It was our hope that the small doped cores, although very weakly guiding, would perform well enough over such a short length scale to maintain coherence of an image to the point it could be guided by the air-silica index step. Although this process sealed the end face and allowed flat cleaves to be easily produced, the images obtained through the tapers suffered from unacceptable levels of coupling. If the transitions could be made shorter then the effects of coupling and scattering could potentially be avoided, but the minimum taper length is, in practice, limited by the flame size. Alternatively, a preform with a larger index step and core ratio could be used to form the cores in future fibres. All the air-clad fibre tapers described here were fabricated by Kerriane Harrington due to her extensive experience with the rig.

After finding that collapsing the fibre entirely ruined image quality, Kerriane began investigating the idea of partially collapsing the fibre to bring the cores closer together and increase resolution, while keeping the taper transition length short and with enough core separation to prevent excessive crosstalk. Images of the best taper she produced are in figure 6.30, as well as a USAF target image to show the increased resolution.

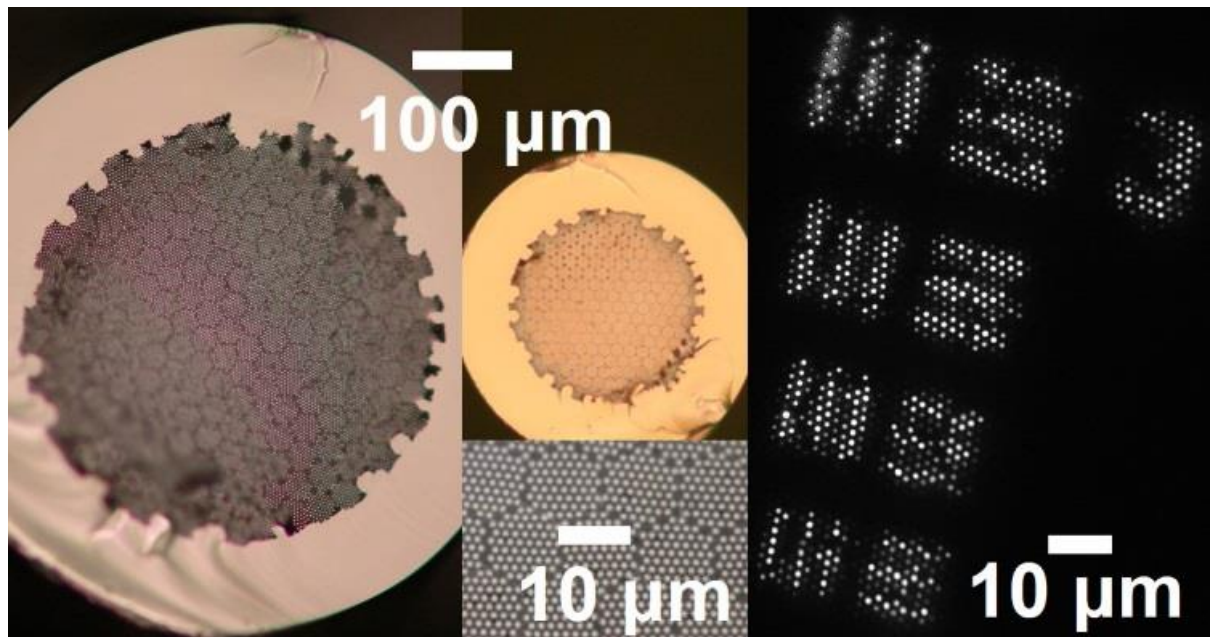


Figure 6.30: Micrographs for transmitted flood illuminated white light of the untapered (left) and tapered (middle) fiber. Elements 3 to 6 of USAF group 7 imaged at 500 nm are shown at the right - the line width in the smallest element is 2.19 μm . The scale bar gives the scale of the target, to compare resolution. However, the incidental magnifying effect of the taper made the image twice as big at the untapered proximal end of the fiber. Provided courtesy of Kerriane Harrington.

This taper was made using a small, 2-3 mm flame to maintain the air cladding as much as possible by reducing the fibre's cross section as a whole. Thanks to the untapered end, there is also some magnification of the sample, and because most of the length of the fibre is left unchanged it carries the signals with minimal coupling, allowing resolutions as high as 2.19 μm at 500 nm wavelength.

6.9.3 Adhesives and wax

A wide variety of materials could potentially be used to plug air-clad fibre capillaries. I chose to narrow my search for an appropriate material to only adhesives and waxes as they were easy to obtain and use. The optical and physical properties required for the application were four-fold:

- Viscosity low enough to easily enter the holes but high enough that it would not move up too quickly and cause excessive loss
- Hard enough to avoid being polished away too quickly compared to the glass, which causes shards to break off and become embedded or undercut surrounding glass
- Transparency to reduce loss
- Refractive index lower than silica (1.472 at 630 nm) to prevent cladding guidance

Beginning with Thor Labs' optical adhesive epoxy, the polishing quality was excellent as it was designed to fix fibres into ferrules, but the epoxy failed to wick more than 0.5 mm up the holes, leaving large patches free after it had been polished back.

I then investigated several waxes by melting them onto the fibre end. Sealing wax worked well, moving over a millimetre into the fibre, but a combination of high absorption and being too soft to achieve a good polish meant that this idea was also a failure.

Ultraviolet cured optical adhesives seem to be the best option. Recent tests using Norland Optical Adhesives glues, particularly NOA1020301, have shown promise. The liquid glue readily wicks up into the fibre, and is easily cured to polishable hardness using a hand-held UV lamp. The optical transparency is good as light can be seen to transmit through a polished fibre, but the index step was too small to allow good quality imaging. This could possibly be mitigated by preventing the glue from progressing more than a millimetre up the holes as such a short length should prevent excessive coupling.

6.10 Conclusion

In this chapter I have described my techniques for the design and fabrication of imaging fibres that guide light using the index step between thousands of solid silica cores and an air-filled cladding. I have shown that these air-clad fibres can continue to image up to at least 1600 nm. This is double the maximum functional wavelength of Fujikura's FIGH-30-650S; the current gold-standard imaging fibre for use in bronchoscopy systems. By drawing the fibre to a thinner diameter the long wavelength functionality was sacrificed for exceptional resolution, yielding clear images of features down to 2.2 μm . The high resolution and long wavelength functionality of my air-clad fibres constitute an enormous technological advantage compared to commercial state-of-the-art alternatives.

These fibres represent a new technology in its infancy, and I have discussed several of the difficulties faced, and potential solutions I have considered, in my early efforts to adapt them for use in a bronchoscope system.

Chapter 7

Conclusion

In this thesis I have described the design and fabrication of novel fibres for endoscopic imaging and sensing. Although the focus has been on improving diagnostic bronchoscope technology for the National Health Service, there is no reason why most, if not all, I have discussed could not be adapted for other purposes.

I first presented novel results in chapter 3, where I described several different designs of optical fibres, and fibre based devices, that improve the signal to noise challenges associated with performing spectroscopic sensing through a silica based fibre. Along with descriptions of their fabrication, I present results obtained through their use, and critique their relative merits. Overall, I show that although the solid sensing fibre solutions were relatively easy to fabricate and implement, hollow core fibre technology holds far more promise for ultra-low background Raman sensing, including the possibility of sensing the Raman signal intrinsic to mammalian tissues.

Chapter 4 contains an account of the iterative steps my group and I took towards developing a relatively inexpensive imaging fibre, with equal or better performance than the commercial state of the art alternative. The fabrication section details how this was ultimately achieved by stacking and drawing regular square arrays of cores, arranged such that no neighbouring cores were of the same size. This fibre is now being incorporated into a bronchoscope system by the Proteus team in Edinburgh in preparation for biocompatibility testing, and eventually, the clinic.

In chapter 5 I provide a full description of my technique for quantitatively characterising imaging fibres. The experimental apparatus is comprised of an interferometer that forms a fringe pattern on the test fibre's end, the transmitted images of which are analysed using two distinct techniques. In the final version of the experiment the light source was a supercontinuum beam, filtered using a monochromator to form a scanning wavelength source. The pitch of the fringes could also be varied simply by changing the angle between the interfering beams. I demonstrated the technique by analysing a selection of the fibres discussed in chapter 4, and showed that the results

provide greater insight into the fibres' performance than test target images alone are capable of. This technique has been published in Optics Express.

The greatest achievement of my PhD is detailed in chapter 6: An entirely new type of imaging fibre that guides light using the index step between silica cores and an air-filled cladding. I show that the resolution of this type of fibre can be equal to a commercial state of the art equivalent, but maintain this performance over more than double the commercial fibre's operational wavelength. Alternatively, by drawing the fibre smaller (or tapering the distal end) these fibres can image at a far higher resolution.

My work has advanced the field of medical optics and, in particular, the results I have achieved with my air-clad imaging fibre should have significant impact in the broader scientific community. These medical techniques are constantly evolving, with seemingly unrelated ideas frequently hybridised to make revolutionary new technologies. I look forward to seeing how the nascent ideas I have presented to the world will be changed and adapted by it.

Appendix A

List of acronyms

TIR	Total internal reflection
NA	Numerical aperture
PCF	Photonic crystal fibre
HCF	Hollow core fibre
NCF	Negative curvature fibre
ARROW	Anti-resonant reflecting optical waveguide
CFB	Coherent fibre bundle
ACI	Air-clad imaging (fibre)
PGI9	Panoptes graded-index 9
ID	Inner diameter
OD	Outer diameter
PTFE	Polytetrafluoroethylene
PMMA	Polymethylmethacrylate
USAF	United States Air Force
OSA	Optical spectrum analyser
SEM	Scanning electron microscope
EDX	Energy dispersive X-ray

SWIR	Short-wave infra-red
NIR	Near infra-red
MSE	Mean square error
MSSIM	Mean structural similarity index
MTF	Modulation transfer function
PCR	Polymerase chain reaction
IPA	Isopropyl alcohol
MBA	Mercaptobenzoic acid
PLL	Poly-l-lysine
SERS	Surface enhanced Raman spectroscopy
CARS	Coherent anti-stokes Raman spectroscopy
SPAD	Single photon avalanche diode
GVD	Group velocity dispersion
CPPM	Centre for photonics and photonic materials
MAS	Microscopy analysis suite
QMRI	Queen's medical research institute

Appendix B

Publications

This list is ordered based on my perceptions of their significance to my PhD.

B.1 Journal publications

H. A. C. Wood, K. Harrington, J. M. Stone, T. A. Birks, and J. C. Knight, “High resolution air-clad imaging fibers,” *Optics Letters* **43**(21), 5311-5314 (2018)

H. A. C. Wood, K. Harrington, J. M. Stone, T. A. Birks, and J. C. Knight, “Quantitative characterisation of endoscopic imaging fibres,” *Optics Express* **25**(3), 1985-1992 (2017)

J. M. Stone, H. A. C. Wood, K. Harrington, and T. A. Birks, “Low index contrast imaging fibres,” *Optics Letters* **42**(8), 1484-1487 (2017)

F. Mohamad, M.G. Tanner, D. Choudhury, T.R. Choudhary, H.A.C. Wood, K. Harrington, and M. Bradley, “Controlled core-to-core photo-polymerisation – fabrication of an optical fibre-based pH sensor,” *Analyst* **142**(19), 3569-3572 (2017)

B.2 Conference presentations

H. A. C. Wood, K. Harrington, J. M. Stone, T. A. Birks, and J. C. Knight, “Quantitative characterisation of endoscopic imaging fibres,” at the Institute of Physics’ Cleo, San Jose, 2016

H. A. C. Wood, K. Harrington, J. M. Stone, T. A. Birks, and J. C. Knight, “Quantitative characterisation of endoscopic imaging fibres,” at the Institute of Physics’ Photon, Leeds University, 2016

J. Stone, H. Wood, K. Harrington, H. Parker, M. G. Tanner, T. Birks and J. Knight “New designs for imaging fibres,” at the Institute of Physics’ Photon, Leeds University, 2016

M. G. Tanner, S. McAughtrie, T. R. Choudhary, D. Choudhury, F. Yu, H. Wood, K. Harrington, N. Krstajic, S. Chankeshwara, R. Henderson, C. Campbell, R. Thomson, K. Dhaliwal and M. Bradley “Multiplexed fibre optic sensing in the distal lung,” at the Institute of Physics’ Photon, Leeds University, 2016

H. Parker, A. Perperidis, K. Harrington, H. Wood, J. Stone, N. Krstajic, R. R. Thomson, K. Dhaliwal and M. G. Tanner, “Imaging and spectroscopic data of pathologies in the distal lung using coherent fibre bundles,” at the Institute of Physics’ Photon, Leeds University, 2016

K. Harrington, J. Stone, H. Wood, J. Knight, and T. Birks, “Reducing crosstalk in multicore fibres with parabolic index profiles,” at the Institute of Physics’ Photon, Leeds University, 2016

T. R. Choudhary, M. G. Tanner, A. Megia-Fernandez, K. Harrington, H. A. Wood, S. Chankeshwara, P. Zhu, D. Choudhury, F. Yu, R. R. Thomson, R. R. Duncan, K. Dhaliwal, and M. Bradley, “Toolkit for multiplexed sensing of physiological parameters in the distal lung with fluorescent probes on multicore fibres,” at SPIE’s Photonics West, San Francisco, 2017

H. Parker, A. Perperidis, K. Harrington, H. Wood, J. Stone, N. Krstajic, R.R. Thomson, K. Dhaliwal and M. Tanner, “Imaging using coherent fibre bundles,” at SUSSP2 Summer School, Photonic Systems for Sensing and Metrology, St Andrews, 2016

References

- [1] P. Bozzini, "Lichtleiter, eine Erfindung zur Anschauung innerer Teile und Krankheiten, nebst der Abbildung," *Journal of Practical Medicine and Surgery*, **24**, 107-124 (1806)
- [2] The Scottish Society of the History of Medicine Proceedings, <http://sshm.ac.uk/archive/> (accessed 18/04/2018)
- [3] <http://history.uroweb.org/history-of-urology/diagnosis/looking-into-the-body/bozzini-and-the-lichtleiter/> (from Gottfried Wiesner, Leipzig, International Nitze-Leiter Reserach Society for Endoscopy/Nitze-Leiter Collection) (accessed 18/04/2018)
- [4] J. Hecht, "City of Light: The Story of Fiber Optics," Oxford University Press, revised and expanded edition, (2004)
- [5] H. Hopkins, and N. S. Kapany, "A flexible fiberscope, using static scanning," *Nature*, **22**(173), 39-41 (1954)
- [6] J. Bhatt, A. Jones, S. Foley, Z. Shah, P. Malone, D. Fawcett, S. Kumar, "Harold Horace Hopkins: A Short Biography," Wiley, (2010)
- [7] J. G. Gow, and H. H. Hopkins, "Handbook of Urological Endoscopy," Churchill Livingstone, 1979
- [8] K. C. Kao, and G. A. Hockham, "Dielectric-fibre surface waveguides for optical frequencies," *Proceedings of the Institution of Electrical Engineers*, **113**(7), 1151-1158 (1966)
- [9] F. P. Kapron, D. B. Keck, and R. D. Maurer, "Radiation losses in glass optical waveguides," *App. Phys. Lett.* **17**(10), 423-425 (1970)
- [10] R. C. Newton, S. V. Kemp, P. L. Shah, D. Elson, A. Darzi, K. Shibuya, S. Mulgrew, G. Z. Yang, "Progress toward optical biopsy: bringing the microscope to the patient," *Lung*, **189**(2), 111-119 (2011)
- [11] <https://proteus.ac.uk/> (accessed 23/09/2018)
- [12] C. M. Lee, C. J. Engelbrecht, T. D. Soper, F. Helmchen, and E. J. Seibel, "Scanning fiber endoscopy with highly flexible 1-mm catheterscopes for wide-field, full-color imaging," *Journal of Biophotonics*, **3**(5-6), 385-405 (2011)
- [13] R. M. Schnabel, K. van der Velden, A. Osinski, G. Rohde, P. M. H. J. Roekaerts, and D. C. J. J. Bergmans, "Clinical course and complications following diagnostic bronchoalveolar lavage in critically ill mechanically ventilated patients," *BMC Pulmonary Medicine*, (2015)
- [14] <https://www.maunakeatech.com/en/cellvizio> (accessed 23/09/2018)
- [15] R. C. Newton, S. V. Kemp, G-Z. Yang, D. S. Elson, A. Darzi, P. L. Shah, "Imaging parenchymal lung diseases with confocal endomicroscopy," *Respiratory Medicine*, **106**(1), 127-137 (2012)
- [16] J. A. Buck, *Fundamentals of Optical Fibres*, 2nd edition, (Wiley, 2004)
- [17] A. W. Snyder and J. D. Love, "Optical waveguide theory," chapters 1 & 2, (Chapman & Hall, 1983)
- [18] E. Hecht, "Optics," (Addison-Wesley, 2002)

- [19] A. L. Love, "Hollow Core Optical Fibre Based Gas Discharge Laser Systems," PhD thesis, University of Bath (2017)
- [20] T. A. Birks, unpublished presentation on the modes of optical fibres.
- [21] A. W. Snyder and J. D. Love, "Optical waveguide theory," chapter 12, (Chapman & Hall, 1983)
- [22] G. F. Carrier, M. Krook and C. E. Pearson, "Functions of a Complex Variable: Theory and Technique," (SIAM, 2005)
- [23] A. W. Snyder and J. D. Love, "Optical waveguide theory," chapter 11, (Chapman & Hall, 1983)
- [24] A. W. Snyder and J. D. Love, "Optical waveguide theory," chapter 36, (Chapman & Hall, 1983)
- [25] T. A. Birks, "Postgraduate series lecture on silica glass," University of Bath, 2017
- [26] J. E. Shelby, "Introduction to Glass Science and Technology," 2nd edition, Royal Society of Chemistry, 2005
- [27] I. Gris-Sánchez, "Fabrication and Applications of low OH Photonic Crystal Fibres," PhD thesis, University of Bath (2012)
- [28] J. C. Knight, T. A. Birks, P. St.J. Russell, and D. M. Atkin, "All-silica single-mode fiber with photonic crystal cladding," *Opt. Lett.* **21**, 1547-1549 (1996);
- [29] W. J. Wadsworth, N. Joly, J. C. Knight, T. A. Birks, F. Biancalana, P. St. J. Russel, "Supercontinuum and four-wave mixing with Q-switched pulses in endlessly single-mode photonic crystal fibres," *Opt. Exp.*, **12**(2), 299-309 (2004)
- [30] J. M. Stone, "Photonic crystal fibres and their applications in the nonlinear regime," PhD thesis, University of Bath (2009)
- [31] F. Yu, "Hollow core negative curvature optical fibres," PhD thesis, University of Bath (2013)
- [32] M. A. Duguay, Y. Kokubun, and T. L. Koch, "Antiresonant reflecting optical waveguides in SiO₂-Si multilayer structures," *App. Phys. Lett.*, **49**(13), 13-15 (1986)
- [33] <https://www.drakauk.com/global-overview.html> (accessed 08/10/2018)
- [34] <https://www.prysmiangroup.com/en> (accessed 08/10/2018)
- [35] P. Geittner, D. Küppers, and H. Lydtin, "Low-loss optical fibers prepared by plasma-activated chemical vapour deposition (CVD)," *Appl. Phys. Lett.*, **28**(11), 645-646 (1976)
- [36] H. Lydtin, "PCVD: A technique suitable for large-scale fabrication of optical fibres," *Journal of Lightwave Technology*, **4**(8), 1034-1038 (1986)
- [37] I. Gris-Sánchez, D. Van Ras, and T. A. Birks, "The Airy fiber: an optical fiber that guides light diffracted by a circular aperture," *Optica* **3**, 270-276 (2016)
- [38] W. H. Reeves, "Photonic crystal fibre: the ultra-fattened dispersion regime," PhD thesis, University of Bath (2003)
- [39] J. N. Israelachvili, "Intermolecular and Surface Forces," chapter 15, Academic Press, New York, (1985)
- [40] Thor Labs product, "Guide to Connectorization and Polishing Optical Fibers," Product FN96A (2018)
- [41] S. Yerolatsitis, "Fibres for Astrophotonics and Other Applications, Confirmation Report," unpublished, University of Bath (2013)
- [42] F. Baldini, P. Bechi, S. Bracci, F. Cosi, and F. Pucciani, "In vivo optical-fibre pH sensor for gastr-oesophageal measurements," *Sensors and Actuators*, **29**, 164-168 (1995)

- [43] E. Heyduk, and T. Heyduk, "Fluorescent homogenous immunosensors for detecting pathogenic bacteria," *Anal. Biochem.*, **396**(2), 298-303 (2010)
- [44] J-M. Fritschy, and W. Härtig, "Immunofluorescence," *Encyclopedia of life sciences*, John Wiley & Sons (2001)
- [45] T. Aslam, A. Miele, S. V. Chankeshwara, A. Megia-Fernandez, C. Michels, A. R. Akram, N. McDonald, N. Hirani, C. Haslett, M. Bradley, and K. Dhaliwal, "Optical molecular imaging of lysyl oxidase activity – detection of active fibrogenesis in human lung tissue," *Chem. Sci.*, **4**, 4946-4953 (2015)
- [46] R. I. Dmitriev, and D. B. Papkovsky, "Intracellular probes for imaging oxygen concentration: how good are they?," *Methods and Applications in Fluorescence*, **3** (2015)
- [47] A. R. Akram, N. Avlonitis, A. Lilienkampf, A. M. Perez-Lopez, N. McDonald, S. V. Chankeshwara, E. Scholefield, C. Haslett, M. Bradley, and K. Dhaliwal, "A labelled-ubiquicidin antimicrobial peptide for immediate in situ optical detection of live bacteria in human alveolar lung tissue," *Chem. Sci.*, **6**, 6971-6979 (2015)
- [48] N. Krstajić, A. R. Akram, T. R. Choudhary, N. McDonald, M. G. Tanner, E. Pedretti, P. A. Dalgarno, E. Scholefield, J. M. Girkin, A. Moore, M. Bradley, K. Dhaliwal, "Two-color widefield fluorescence microendoscopy enables multiplexed molecular imaging in the alveolar space of human lung tissue," *Journal of Biomedical Optics*, **21**(4), 046009 (2016)
- [49] A. W. Ng, A. Bidani, and T. A. Heming, "Innate Host Defense of the Lung: Effects of Lung-lining Fluid pH," *Lung*, **182**(5), 297-317 (2004)
- [50] K. Ehrlich, A. Kufcsák, N. Krstajić, R. K. Henderson, R. R. Thompson, and M. G. Tanner, "Fibre optic time-resolved spectroscopy using CMOS-SPAD arrays," *Optical Fibers and Sensors for Medical Diagnostics and Treatment Applications XVII*, (Proceedings of SPIE; Vol. 10058)
- [51] F. Mohamad, M. G. Tanner, D. Choudhury, T. R. Choudhary, H. A. C. Wood, K. Harrington, and M. Bradley, "Controlled core-to-core photo-polymerisation – fabrication of an optical fibre-based pH sensor," *Analyst*, **142**(19), 3569-3572 (2017)
- [52] R. Quarrell, T. D. W. Claridge, G. W. Weaver, and G. Lowe, "Structure and properties of TentaGel resin beads: Implications for combinatorial library chemistry," *Molecular Diversity*, **1**(4), 223-232 (1996)
- [53] C. Lamberti, and G. Agostini, "Characterisation of Semiconductor Heterostructures and Nanostructures," chapter 8, "Raman spectroscopy," written by D. Wolverson, Elsevier Science and Technology (2011)
- [54] R. L. McCreery, "Raman Spectroscopy for Chemical Analysis," John Wiley & Sons, (2000)
- [55] M. Fleischmann, P. J. Hendra, and A. J. McQuillan, "Raman spectra of pyridine adsorbed at a silver electrode," *Chemical Physics Letters*, **24**(2), 163-166 (1974)
- [56] E. Smith, and G. Dent, "Modern Raman Spectroscopy: A Practical Approach," Wiley, (2005)
- [57] E. C. Le Ru, E. Blackie, M. Meyer, and P. G. Etchegoin, "Surface Enhanced Raman Scattering Enhancement Factors: A Comprehensive Study," *Journal of Physical Chemistry*, **111**(37), 13794-13803 (2007)
- [58] F. Wang, R. G. Widejko, Z. Yang, K. T. Nguyen, H. Chen, L. P. Fernando, K. A. Christensen, and J. N. Anker, "Surface-Enhanced Raman Scattering Detection of pH with Silica-Encapsulated 4-Mercaptobenzoic Acid-Functionalised Silver Nanoparticles," *Anal. Chem.*, **84**(18), 8013-8019 (2012)
- [59] B. Fortuni, T. Inose, S. Uezono, S. Toyouchi, K. Umamoto, S. Sekine, Y. Fujita, M. Ricci, G. Lu, A. Masuhara, J. A. Hutchinson, L. Latterini, and H. Uji-I, "*In situ* synthesis of Au-shelled Ag

- nanoparticles on PDMS for flexible, long-life, and broad spectrum-sensitive SERS substrates," *Chem. Commun.*, **53**, 11298-11301 (2017)
- [60] Q. Lin, and G. P. Agrawal, "Raman response function for silica fibers," *Opt. Lett.*, **31**(21), 3086-3088 (2006)
- [61] T. A. Birks, B. J. Mangan, A. Díez, J. L. Cruz, and D. F. Murphy, "'Photonic lantern' spectral filters in multi-core fibre," *Opt. Express* **20**, 13996-14008 (2012)
- [62] D. Choudhury, M. G. Tanner, S. McAughtrie, F. Yu, B. Mills, T. R. Choudhary, S. Seth, T. H. Craven, J. M. Stone, I. K. Mati, C. J. Campbell, M. Bradley, C. K. I. Williams, K. Dhaliwal, T. A. Birks, and R. R. Thomson, "Endoscopic sensing of alveolar pH," *Biomed. Opt. Exp.*, **8**(1), 243-259 (2017)
- [63] S. Yerolatsitis, F. Yu, S. McAughtrie, M.G. Tanner, H Fleming, J. M. Stone, C. J. Campbell, T. A. Birks, and J. C. Knight, "Ultra-low background Raman sensing using a negative-curvature fibre," Submitted to *Optica Letters*, (2018)
- [64] J. M. Stone, H. A. C. Wood, K. Harrington, and T. A. Birks, "Low index contrast imaging fibres," *Opt. Lett.* **42**(8), 1484-1487 (2017)
- [65] A. W. Snyder and J. D. Love, "Optical Waveguide Theory," chapters 18 & 29, (Chapman and Hall, 1983).
- [66] X. Chen, K. L. Reichenbach, and C. Xu, "Experimental and theoretical analysis of core-to-core coupling on fiber bundle imaging," *Opt. Express* **16**(26), 21598–21607 (2008).
- [67] A. W. Snyder, and P. McIntyre, "Crosstalk between light pipes," *Journ. Opt. Soc. Am.*, **66**(9), 877-882 (1976)
- [68] S. S. Abdullaev, and F. Kh. Abdullaev, "On propagation of light in fiber bundles with random parameters," *Radiophysics* **23**(6), 766-767 (1980)
- [69] P. W. Anderson, "Absence of Diffusion in Certain Random Lattices," *Phys. Rev.* **109**(5), 1492-1505 (1958)
- [70] <http://www.fujikura.co.uk/products/medical-industrial-optical-fibre/image-fibre/> (accessed 23/10/2018)
- [71] G. H. Sigel Jr., M. J. Marrone, "Photoluminescence in as-drawn and irradiated silica optical fibers: an assessment of the role of non-bridging oxygen defect centres," *Journal of Non-Crystalline Solids* **42**(2), 235-247 (1981)
- [72] B. Zhang, C. Zhai, S. Qi, W. Guo, Z. Yang, A. Yang, X. Gai, Y. Yu, R. Wang, D. Tang, G. Tao, B. Luther-Davies, "High-resolution chalcogenide fibre bundles for infrared imaging," *Opt. Lett.* **40**(19), 4384-4387 (2015)
- [73] http://www.schott.com/d/lightingimaging/e8fd66ab-67ab-4bfe-998d-3bc67a274038/1.0/1fb_datasheet_int_april_2015.pdf (accessed 23/04/2018)
- [74] A. J. Thompson, C. Paterson, M. A. A. Neil, C. Dunsby, and P. M. W. French, "Adaptive phase compensation for ultracompact laser scanning endomicroscopy," *Opt. Lett.*, **36**(9), 1707-1709 (2011)
- [75] J. C. Roper, S. Yerolatsitis, T. A. Birks, B. J. Mangan, C. Dunsby, P. M. W. French, and J. C. Knight, "Minimizing group index variations in a multicore endoscope fiber," *IEEE Photonics Technology Letters* **27**(22), 2359-2362 (2015)
- [76] Y. Kim, S. Warren, F. Favero, J. Stone, J. Clegg, M. Neil, C. Paterson, J. Knight, P. French, and C. Dunsby, "Semi-random multicore fibre design for adaptive multiphoton endoscopy," *Opt Express*, **26**(3), 3661-3673 (2018)

- [77] V. Tsvirkun, S. Sivankutty, G. Bouwmans, O. Katz, E. R. Andresen, and H. Rigneault, "Widefield lensless endoscopy with a multicore fiber," *Opt. Lett.*, **41**(20), 4771-4774 (2016)
- [78] K. Saitoh, M. Koshiha, K. Takenaga, and S. Matsuo, "Homogeneous and Heterogeneous Multi-core Fibers," IEEE Photonics Society Summer Topical Meeting Series, (2012)
- [79] H. A. C. Wood, K. Harrington, J. M. Stone, T. A. Birks, and J. C. Knight, "Quantitative characterisation of endoscopic imaging fibres," *Opt. Exp.*, **25**(3), 1985-1992 (2017)
- [80] S. Karbasi, R. J. Frazier, K. W. Koch, T. Hawkins, J. Ballato, and A. Mafi, "Image transport through a disordered optical fibre mediated by transverse Anderson localisation," *Nat. Comms.*, **5**(3362), (2014)
- [81] J. Zhao, J. E. A. Lopez, Z. Zhu, D. Zheng, S. Pang, R. A. Correa, and A. Schülzgen, "Image Teansport Through Meter-Long Randomly Disordered Silica-Air Optical Fiber," *Sci. Rep.*, **8**(3065), (2018)
- [82] X. Chen, K. L. Reichenbach, and C. Xu, "Experimental and theoretical analysis of core-to-core coupling on fiber bundle imaging," *Opt. Exp.*, **16**(26), 21598-21607 (2008)
- [83] J. Coltman, "Scintillation Limitations to Resolving Power in Imaging Devices," *Optical Society of America*, **44**(3), 234-237 (1954)
- [84] K. Rossman, "Measurement of the Modulation Transfer Function of Radiographic Systems Containing Fluorescent Screens," *Phys. Med. Biol.*, **9**(4), 551-557 (1964)
- [85] Khosro Madanipour and Mohammad T. Tavassoly, "Determination of modulation transfer function of a printer by measuring the autocorrelation of the transmission function of a printed Ronchi grating," *Appl. Opt.* **48**, 725-729 (2009)
- [86] J. Otón, C. O. S. Sorzano, R. Marabini, E. Pereiro, and J. M. Carazo, "Measurement of the modulation transfer function of an X-ray microscope based on multiple Fourier orders analysis of a Siemens star," **23**(8), 9567-9572 (2015)
- [87] J. W. Coltman, "The Specification of Imaging Properties by Response to a Sine Wave Input," *Journal of the Optical Society of America*, **44**(6), 468-471 (1954)
- [88] https://www.thorlabs.com/newgrouppage9.cfm?objectgroup_id=5840
- [89] H. A. C. Wood, K. Harrington, J. M. Stone, T. A. Birks, and J. C. Knight, "Quantitative characterisation of endoscopic imaging fibers," *Opt. Exp.*, **25**(3), 1985-1992 (2017)
- [90] T. Butz, "Fourier Transformation for Pedestrians," Springer, (2006)
- [91] J. M. Stone, "Photonic crystal fibres and their applications in the nonlinear regime," PhD thesis submitted at the University of Bath (2009)
- [92] <https://www.electrooptics.com/feature/super-lasers> (accessed 17/05/2018)
- [93] F. Yu, W. J. Wadsworth, J. C. Knight, "Low loss silica hollow core fibers for 3-4 μm spectral region," *Opt. Exp.* **20**(10), 11153-11158 (2012)
- [94] N. Arora, D. Martins, D. Ruggerio, E. Tousimis, A. J. Swistel, M. P. Osborne, and R. M. Simmons, "Effectiveness of a noninvasive digital infrared thermal imaging system in the detection of breast cancer," *Am. J. Surg.* **196**(4), 523-526 (2008).
- [95] T. M. Buzug, S. Schumann, L. Pfaffmann, U. Reinhold, and J. Ruhlmann, "Functional Infrared Imaging for Skin-Cancer Screening," in *Conference Proceedings of IEEE Engineering in Medicine and Biology Society*, (IEEE, 2006), pp. 2766-2769.
- [96] T. Kobayashi, T. Katagiri, and Y. Matsuura, "Multi-element hollow-core anti-resonant fiber for infrared thermal imaging," *Opt. Exp.* **24**(23), 26565-26574 (2016)

- [97] B. Zhang, C. Zhai, S. Qi, W. Guo, Z. Yang, A. Yang, X. Gai, Y. Yu, R. Wang, D. Tang, G. Tao, B. Luther-Davies, "High-resolution chalcogenide fibre bundles for infrared imaging," *Opt. Lett.* **40**(19), 4384-4387 (2015)
- [98] S. Qi, B. Zhang, C. Zhai, Y. Li, A. Yang, Y. Yu, D. Tang, Z. Yang, and B. Luther-Davies, "High-resolution chalcogenide fiber bundles for longwave infrared imaging," *Opt. Exp.* **25**(21), 26160-26165 (2017)
- [99] L. Michaille, C. R. Bennett, D. M. Taylor, and T. J. Shepherd, "Multicore Photonic Crystal Fiber Lasers for High Power/Energy Applications," *IEEE Journal of selected topics in quantum electronics*, **15**(2), 328-336 (2009)
- [100] T. Mansuryan, Ph. Rigaud, G. Bouwmans, V. Kermene, Y. Quiquempois, A. Desfarges-Berthelemot, P. Armand, J. Benoist, and A. Barthélémy, "Spatially dispersive scheme for transmission and synthesis of femtosecond pulses through a multicore fiber," *Optics express*, **20**(22), 24769-24777 (2012)
- [101] Arash Mafi, Salman Karbasi, Karl W. Koch, Thomas Hawkins, John Ballato, "Transverse Anderson Localization in Disorderd Glass Optical Fibres: A Review," *Materials* **7**(8), 5520-5527 (2014)
- [102] J. Zhao, J. E. A. Lopez, Z. Zhu, D. Zheng, S. Pang, R. A. Correa, and A. Schülzgen, "Image Transport Through Meter-Long Randomly Disordered Silica-Air Optical Fiber," *Nat. Sci. Repts.* **8**(3065), 1-7 (2018)
- [103] Martijn A. van Eijkelenborg, "Imaging with microstructured polymer fibre," *Opt. Express* **12**, 342-346 (2004)
- [104] M-L. V. Tse, Z. Liu, L-H. Cho, C. Lu, P-K. A. Wai, H-Y. Tam, "Superlattice Microstructured Optical Fiber," *Materials*, **7**, 4567-4573 (2014)
- [105] H. A. C. Wood, K. Harrington, T. A. Birks, J. C. Knight, and J. M. Stone, "High-resolution air-clad imaging fibers," *Opt. Lett.* **43**(21), 5311-5314 (2018)